



UNIVERSITÀ DEGLI STUDI DI TRENTO
UNIVERSITY OF TRENTO

General Relativistic Magnetohydrodynamic Simulations of Binary Neutron Star Mergers

Thesis submitted for the degree of
Doctor Philosophiæ

CANDIDATE:

Takumu Kawamura

SUPERVISOR:

Prof. Bruno Giacomazzo

February 2017

*Dedicated to my mother Rika
and my father Iwao.*

Table of Contents

Title Page	i
Table of Contents	iv
Citations to Previously Published Works	vii
1 Introduction	1
2 Astrophysical motivation	2
3 Formulations	7
3.1 ADM “3+1” formalism	7
3.2 BSSNOK formalism	9
3.3 Gauge conditions	10
3.4 “Valencia” formulation	11
3.4.1 Induction equations for electromagnetic field	11
3.4.2 Conservative form of GRMHD equations	12
3.5 Extracting GW signals	14
4 Numerical methods	15
4.1 Evolution method for spacetime curvature	15
4.2 HRSC method	15
4.3 Reconstruction of primitive values	16
4.4 Riemann solver	17
4.5 Modified Lorenz gauge	17
4.6 Atmosphere	17
4.7 Excision	17
5 General relativistic magnetohydrodynamic simulations of binary neutron star mergers with the APR4 equation of state	19
5.1 Models	19
5.2 Numerical setups	22
5.3 Results	23
5.3.1 General dynamics	23
5.3.2 Magnetic field evolution	23
5.3.3 GW signal	24

5.3.4	Constraints violation	26
6	Binary neutron star mergers and short gamma-ray bursts: Effects of magnetic field orientation, equation of state, and mass ratio	32
6.1	Models	32
6.2	Numerical setups	33
6.3	Evolution	34
6.3.1	Ideal-Fluid Equal-Mass Model	36
6.3.2	Comparison with Rezzolla et al. 2011	42
6.3.3	Effects of the Initial Magnetic Field Orientation	46
6.3.4	Ideal-Fluid Unequal-Mass Model	47
6.3.5	Equal-Mass H4 Model	51
6.3.6	Comparison with Kiuchi et al 2014	54
6.3.7	Unequal-Mass H4 model	57
6.3.8	Influence of Resolution	58
6.3.9	Constraints violation	62
6.4	Short Gamma-Ray Bursts and Other Electromagnetic Signals	64
6.5	Gravitational Waves	70
7	Conclusions	73
A	Visualizing the Field Structure	74
	Bibliography	75

Citations to Previously Published Works

Part of the contents of this Thesis has already appeared in the following papers:

Refereed Journals:

- *Binary neutron star mergers and short gamma-ray bursts: Effects of magnetic field orientation, equation of state, and mass ratio*
Kawamura T., Giacomazzo B., Kastaun W., Ciolfi R., Endrizzi A., Baiotti L., Perna R., 2016, *Physical Review D*, **94**, 064012.
- *General relativistic magnetohydrodynamic simulations of binary neutron star mergers with the APR4 equation of state*
Endrizzi A., Ciolfi R., Giacomazzo B., Kastaun W., **Kawamura T.**, 2016, *Classical and Quantum Gravity*, **33**, 164001.

Chapter 1

Introduction

In this thesis I present results of my fully general relativistic magnetohydrodynamic (GRMHD) simulations of binary neutron star (BNS) mergers, conducted by using the numerical code “Whisky”. The results were published in two papers [29, 47]. In the first one I worked on simulations of “high-mass” BNSs, in which a black hole is promptly formed after merger. The adopted equation of state (EOS) for neutron matter is APR4 and both magnetized and unmagnetized cases are investigated. In the second paper [47] we use two different EOSs (ideal fluid and H4), three different magnetic field orientations (both fields of the two neutron stars aligned with the total angular momentum, one aligned and one anti-aligned, and both anti-aligned) and mass ratios (equal and unequal mass). These simulations are aimed at investigating the effects of these parameters (EOSs, magnetic fields, mass ratios) on the dynamics of the merger and the possible formation of relativistic jets, which is thought to be one of the necessary conditions for the central engine of short gamma-ray bursts (SGRBs).

This thesis is organized as follows. In chapter 2 I describe why BNS systems are important and why we need to perform GRMHD simulations. In chapter 3 I describe the formalism for the GRMHD equations used in the “Whisky” code, and in chapter 4 I describe the numerical methods used to solve those equations. In chapter 5 I present the main results published in reference [29]. In chapter 6 I instead present the results of the simulations published in reference [47] and of which I was the first author. In chapter 7 I conclude and summarize the main results of this thesis.

Chapter 2

Astrophysical motivation

Neutron stars (NSs) are compact objects which are mainly supported by degenerate neutron pressure. Typical NSs observed as pulsars have masses of $\sim 1.4M_{\odot}$, radii of $\sim 10\text{-}14$ km, spin periods of ~ 0.5 second and magnetic field strength of $\sim 10^{12}$ G. NSs are believed to be related to many exotic astrophysical phenomena in the universe, such as, pulsars, supernovae, short gamma-ray bursts (SGRBs), and they are also sources of gravitational waves.

NSs are thought to be formed during supernovae. Ordinary stars more massive than $\sim 9\text{-}10M_{\odot}$ would finally produce iron cores at their centers at the end of their main sequence. When the central iron cores reach the Chandrasekhar mass, electron degeneracy pressure in the cores can no longer support structure of the cores, so the cores start to collapse gravitationally. The inner part of the iron cores collapse to form neutron stars, which would remain after the supernova explosion.

While measuring masses of isolated NSs is not a simple task, masses of NSs observed as pulsars in binary (or multiple) systems can be relatively easily estimated from trajectories of stars by Kepler's law considered with general relativistic effects. For example masses of NSs in binary neutron star systems have a Gaussian distribution centered on $1.35 \pm 0.04M_{\odot}$ ([53]). On the other hand, determining radii of NSs is a relatively tough work due to current insufficient resolution of telescopes. We cannot directly measure radii of NSs but one of the methods is spectroscopic analysis on thermonuclear phenomena occurring on surfaces of NSs, which can put some constraints on radii (and masses) of NSs. For example observation of Type 1 X-ray bursts from accreting NSs in three different X-ray binaries ([64]) indicates the radii of $8\text{km} \lesssim R_{NS} \lesssim 12\text{km}$, along with the masses of $1.3M_{\odot} \lesssim M_{NS} \lesssim 2M_{\odot}$.

Since we cannot study in a laboratory matter at densities as high as the ones reached in the NS cores, EOS and internal structure of NSs are not well known. One way to determine EOS is observing masses and radii of NSs because an EOS relates masses to radii. In particular measuring maximum mass of NSs would help excluding some EOSs from consideration because possible maximum mass differs depending on EOSs.

Though there are several formation channels for binary neutron star (BNS) systems, a standard scenario of forming a BNS is as follows (see Figure 2.1): there are two ordinary stars, whose masses are above $\sim 8M_{\odot}$ and below $\sim 25M_{\odot}$, between this range the stars

undergo supernovae and produce neutron stars; The heavier star (primary) evolves faster and reaches a supernova, then produces a NS; if the lighter star (secondary) is not kicked off from the binary, then a NS-ordinary star binary survives; as the secondary evolves, the hydrogen envelope of the secondary covers the NS and the Helium core of the secondary and it extracts the orbital momentum from the NS-He core binary (common envelope phase); the envelope is finally ejected from the binary for its high angular momentum, and a close binary consisting of a NS and a He core is left behind; the He core goes through a supernova and it produces a NS; if the NS produced from the primary is not kicked off, then a binary of two NSs is formed. In this scenario whether a NS moving through common envelope will collapse to form a BH by accretion of matter or not is critical. If a BH was formed, this scenario would finally produce a BH-NS binary.

Another scenario, which can avoid the BH formation during the common envelope phase, is that if the masses of initial two ordinary stars are nearly the same, the secondary leaves the main sequence soon after the primary does so and before the primary reaches a supernova. Then two He cores are left inside the common envelope and the problem of forming a BH during common envelope phase is avoided. After the envelope is ejected, two naked He cores are left, and if this binary He cores survives two supernovae explosions, a BNS is formed.

Such BNSs are rare because binaries have to survive two supernovae, but still there are some observations of BNSs. One of them is PSR 1913+16, which is a binary consisting of a pulsar and a neutron star. Regarding this binary, a decay in the orbital period is observed, which agrees to high precision with a theoretical decay predicted from general relativity [42]. Another BNS is J0737-3039 A+B, which is composed of two pulsars and whose orbital frequency is 2.45 hours.

Observing BNSs provides us many valuable information: merely an observation of a BNS indicates that in some cases formation of BHs in the evolution path of binary stars can be avoided, by restricted amount of accretion matter onto a NS (in the standard scenario) or preventing NSs from being covered by hydrogen envelope (in the another scenario); observation of orbital parameters of BNSs provides us with accurate measures of the masses of composing NSs. The maximum mass observed up to now is $\sim 2M_{\odot}$, which puts constraint on possible EOSs for nuclear matter. The decay of orbital period of PSR 1913+16, which agrees very well with the general relativistic prediction assuming GWs extract orbital angular momentum from the system, proved the existence of GWs indirectly.

Coalescence of two neutron stars in a binary is believed to be one of the possible central engines of Short Gamma-Ray Bursts (SGRBs). Gamma-Ray Bursts (GRBs) are nonrepeating flashes of bright gamma-ray, sometimes followed by x-ray/optical/radio afterglows. In particular, SGRBs indicate such flashes whose duration are below 2s, while the others (whose duration above 2s) are called Long Gamma-Ray Bursts. This classification of GRBs is based on the observed distribution of duration of GRBs, in which two peaks exist below and above 2s ([52]). These two peaks are naturally expected to indicate different central engines between Short and Long Gamma-Ray Bursts.

The idea that coalescences of two neutron stars are the sources of SGRBs is supported by the following evidences: SGRBs have cosmological origin, occur in various types of galaxies, and are not associated with supernovae, in addition to their energy scale ($\sim 10^{51}$

erg) and time scale (from 100ms to 2s). Although the mechanism of SGRBs is unclear, there are some models explaining SGRBs. A standard model is based on the idea that when two neutron stars merge, the merger remnant collapses to form a black hole and a massive disk around it. Then the accretion of the disk onto the black hole would finally produce a relativistic jet, which may be observed as a gamma-ray emission. Another possibility is, when two NSs merge, the merger remnant undergoes a hypermassive neutron star (HMNS) phase for some time followed by collapse to a black hole, or remains as a stable supramassive neutron star (SMNS). During these HMNS or SMNS phases, a disk may be produced around them and fall onto the central remnant, which may produce a relativistic jet. Meanwhile, electromagnetic spindown of the central remnant or neutrino heating may power an afterglow ([23],[59]). Yet another possible scenario is the "time-reversal" scenario ([21], [20]), in which a NS remnant produced from the merger survives for some time, and its rotational energy powers the X-ray afterglow, while the gamma-ray burst is powered by accretion of the surrounding disk onto the black hole produced after the long-lived NS remnant finally collapses.

All these scenarios include relativistic jets, which are believed to be necessary because gamma-ray emission is thought to be generated from a relativistic jet. Mainly two mechanisms explaining how such a jet is formed have been considered, one is neutrino-anti neutrino annihilation, and the other is magnetic field. In the former mechanism, neutrino-anti neutrino annihilation, the annihilation process transports thermal energy from the accretion disk to low density region along the rotation axis of the black hole, which may drive a relativistic jet. But in [45], it is shown that annihilation of neutrinos alone may be insufficient to power a jet in case of BNS mergers. In the latter mechanism, magnetic field [16], when poloidal magnetic field lines penetrate a spinning black hole, the rotational energy of the black hole can be extracted electromagnetically and power a jet, which is believed to be more promising mechanism.

Binary neutron stars (BNSs) are also important as sources of gravitational waves (GWs). GWs are space-time distortion propagating in space with the speed of light, whose existence has been theoretically predicted from general relativity. It was very recently that GW signals from binary black holes were actually detected ([3],[2]) by advanced LIGO, a ground-based interferometer for GWs located in the U.S.A. Other interferometers, such as advanced VIRGO in Italy and KAGRA in Japan are also proceeding to start their operations to detect more GW signals and extract more information from GWs.

While GWs from BNSs have not been detected yet, the expected detection rate by advanced LIGO and VIRGO is $\sim 0.4-400$ per year [1], so GWs from BNSs may be detected in the near future. If detected, we can extract many valuable information about the source. For example, masses of two composing NSs and GW waveform just before merger, can put constraint on possible EOSs of neutron matter. As described before, the observed maximum mass of NSs can exclude EOSs that do not support such large masses. While, GW just before merger depends on how NSs are tidally disrupted, which is affected by EOSs, so the part of GW signal just before merger is also a key to determine the EOS. The difference of EOSs also affects general dynamics of BNS mergers, that is, whether the merger remnant is a BH or a HMNS/SMNS under certain masses, and how long the remnant lives before collapsing to a BH (or remains as a stable NS) and the frequency of oscillating remnant

(f, g, p, w and r-modes) if it is a HMNS/SMNS. The dynamics of these systems strongly affect the GW signals, so comparing observed GW signals after merger with numerically calculated ones can help in determining the EOS.

As described before, the standard scenario for the central engine of SGRBs requires the coalescence of BNSs. A simultaneous observation of a SGRB and a GW signal from a BNS merger would validate such a scenario.

Numerical simulations of coalescence of BNSs may help addressing some questions, such as: what is the final phase of merger of two NSs?; what GWs are emitted from BNSs, and what information about the initial NSs can we get from the wave signals?; what fraction of the total mass of BNS is left in the disks, which may be formed around the central BHs or HMNSs after merger of two NSs?; what is the emission of neutrino and electromagnetic (EM) waves from BNSs?; what role do magnetic fields play in the evolution of BNS mergers, and GW, EM, neutrino emissions?; do mergers produce significant amount of elements via r-process nucleosynthesis?

To address these questions, some fully general relativistic magnetohydrodynamic (GRMHD) simulations of BNS mergers have been conducted. The first successful full GRMHD simulations are [7, 55, 35], in which effect of magnetic fields on dynamics of evolution and GW signals are investigated. Related to SGRBs, some simulations try to see if relativistic jets are launched from BNS mergers [76, 72, 49]. In [72], after a long simulation of BNS mergers, authors see a poloidal magnetic field configuration with a half-opening angle of 30° along the BH spin axis, though a jet itself is not launched. However, this poloidal field structure is one of the necessary conditions to launch a jet, so this simulation gives an indication that BNS mergers can launch relativistic jets. While in [49], authors do not see such structure under a different EOS. In [76], however, authors show launch of a mildly relativistic jet from BNS merger with initial magnetic field strength of $\sim 10^{15}$ G. Indeed this value is unrealistically high, but during HMNS phase after merger, magnetic field strength is amplified and can reach such large values, so this simulation also gives an indication that merger of BNS can launch a jet.

In addition to these full GRMHD simulations, some efforts have been made to do more realistic simulations. For example, a resistive magnetohydrodynamic simulation [26], or incorporation of thermodynamics and neutrino leakage [66]. Still further progress is needed to address these problems.

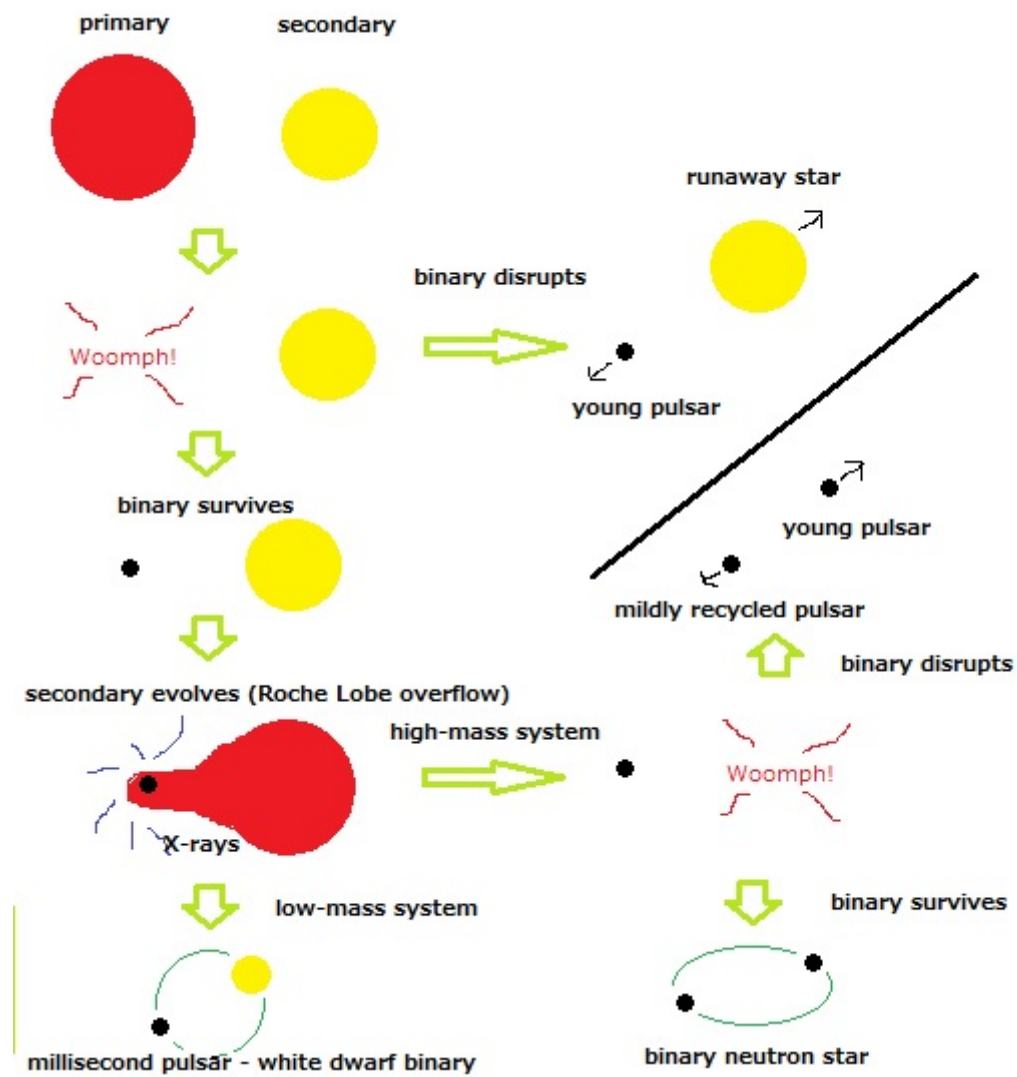


Figure 2.1 Cartoon visualizing the standard formation channel for BNSs. Image based on Figure 7 in [57].

Chapter 3

Formulations

In this chapter we describe the equations used in our fully general relativistic magnetohydrodynamic (GRMHD) simulations, such as the equations for evolution of gravitational field, matter dynamics and magnetic field evolution. In addition to these, we describe the formalism to extract GW signals. In this thesis I use a spacelike signature $(-, +, +, +)$ and geometric units ($c = G = M_{\odot} = 1$) unless specified otherwise.

The Einstein equations, which describes the relationship between matter and geometry of spacetime, are

$$G_{\mu\nu} = 8\pi T_{\mu\nu}, \quad (3.1)$$

$$G_{\mu\nu} \equiv R_{\mu\nu} - \frac{1}{2}g_{\mu\nu}R, \quad (3.2)$$

where $T_{\mu\nu}$ is the stress-energy tensor, $G_{\mu\nu}$ is the Einstein tensor, $R_{\mu\nu}$ is the Ricci tensor, R is the Ricci scalar, and $g_{\mu\nu}$ is the metric. All these variables are considered and defined in 4-dimensional spacetime.

To solve the Einstein equations, coupled with equations for matter and electromagnetic field dynamics, the BSSNOK formalism, based on the ADM formalism, is adopted for spacetime.

3.1 ADM “3+1” formalism

The 3+1 formalism is an approach to solving the Einstein equations based on the slicing of the 4-dimensional spacetime by 3-dimensional spacelike hypersurfaces. This formalism was originally introduced by Georges Darmois [25], André Lichnerowicz [54] and Yvonne Choquet-Bruhat [19]. Following these works, the Arnowitt Deser Misner (ADM) formalism [9], the Hamiltonian formulations of general relativity, was founded. In the ADM formalism, 4-dimensional spacetime is foliated by multiple 3-dimensional spacelike hypersurfaces, which are parameterized by time parameter t . Then the future-pointing normal vector to each hypersurface can be defined as $\mathbf{n} \equiv -\alpha\nabla t$, where α is a value chosen to normalize the vector \mathbf{n} . Here coordinate is introduced as $\{\mathbf{e}_{(\mu)}\} = \{\mathbf{e}_{(0)}, \mathbf{e}_{(i)}\}$, where $\mathbf{e}_{(0)}$, the time coordinate basis, is defined so that $\mathbf{e}_{(0)} \cdot \nabla t = 1$. The other three bases $\mathbf{e}_{(i)}$ are

spacelike and tangent to hypersurfaces ($\mathbf{n} \cdot \mathbf{e}_{(i)} = 0$). Then \mathbf{n} can be expressed using this coordinate as follows,

$$\mathbf{n} = \frac{\mathbf{e}_{(0)}}{\alpha} - \frac{\beta}{\alpha}, \quad (3.3)$$

here $\beta = \beta^i \mathbf{e}_{(i)}$ is so called *shift* vector, since it describes how spatial part of the coordinate changes when moving from a hyperspace to neighborhood one, while α is called *lapse*, since it corresponds to time advance from a hypersurface to another one. Under this coordinate, the line element of spacetime is written as

$$ds^2 = -(\alpha^2 - \beta^i \beta_i) dt^2 + 2\beta_i dx^i dt + \gamma_{ij} dx^i dx^j. \quad (3.4)$$

Here γ_{ij} is the 3-metric in the hypersurfaces, which is the projection of 4-metric $g_{\mu\nu}$ onto the hypersurfaces (defined as $\gamma_{\mu\nu} \equiv g_{\mu\nu} + n_\mu n_\nu$). Another important variable for ADM formalism is the extrinsic curvature, defined as

$$K_{ij} \equiv -\gamma_i^k \gamma_j^l \nabla_{(k} n_{l)}, \quad (3.5)$$

where ∇_i denotes covariant derivative regarding the 3-metric γ_{ij} . The extrinsic curvature describes how the spacial hypersurface is embedded in 4-dimensional spacetime. Now the trace of the extrinsic curvature, $K \equiv \gamma^{ij} K_{ij}$, is called mean curvature, which describes how much the volume on spacial hypersurface changes when moving along the direction of n_l from one hypersurface to another one. Based on this “3+1” foliation of spacetime and defined variables, the Einstein equations can be split into evolution equations and constraint equations (the Hamiltonian constraint equation and the momentum constraint equations).

The evolution equations are:

$$D_t \gamma_{ij} = -2\alpha K_{ij}, \quad (3.6)$$

$$D_t K_{ij} = -\nabla_i \nabla_j \alpha + \alpha [R_{ij} + K K_{ij} - 2K_{im} K_j^m - 8\pi (S_{ij} - \frac{1}{2} \gamma_{ij} S) - 4\pi \rho \gamma_{ij}], \quad (3.7)$$

where $D_t \equiv \partial_t - \mathcal{L}_\beta$ and \mathcal{L}_β denotes the Lie derivative along the vector β , R_{ij} is the Ricci tensor of the spacial metric γ_{ij} , $S_{ij} \equiv \gamma_{i\mu} \gamma_{j\nu} T^{\mu\nu}$ is the projection of stress-energy tensor in 4-dimensional spacetime onto the spacial hypersurface, $S \equiv \gamma^{ij} S_{ij}$, and $\rho \equiv n_\mu n_\nu T^{\mu\nu}$ is the total energy density measured by a normal observer.

The Hamiltonian constraint equation is given by

$$R + K^2 - K_{ij} K^{ij} - 16\pi \rho = 0, \quad (3.8)$$

where R denotes the Ricci Scalar of the spacial metric.

And finally the momentum constraint equations are

$$\nabla_j K^{ij} - \gamma^{ij} \nabla_j K - 8\pi S^i = 0, \quad (3.9)$$

where $S^i \equiv -\gamma^{i\mu}n^\nu T_{\mu\nu}$ is the momentum density measured by a normal observer. The Hamiltonian and momentum constraint equations represent the constraint which should be satisfied on each spacial hypersurface, and the evolution equations determine the spacial metric on a hypersurface from that on previous hypersurface if *gauge* conditions (imposed on the values of α and β) are given. The set of equations (3.6)-(3.9) is the original ADM formalism.

3.2 BSSNOK formalism

The original ADM formalism is now known not to be stable for long-term simulations, and a more robust formalism, based on the conformal traceless reformulation of the ADM equations, is the BSSNOK formalism ([14, 77, 62]).

In the BSSNOK formalism, the 3-metric γ_{ij} and the trace-free part of the extrinsic curvature ($A_{ij} \equiv K_{ij} - \frac{1}{3}\gamma_{ij}K$) are decomposed using a conformal factor as follows.

$$\tilde{\gamma}_{ij} \equiv e^{-4\phi}\gamma_{ij}, \quad (3.10)$$

$$\tilde{A}_{ij} \equiv e^{-4\phi}A_{ij}, \quad (3.11)$$

where the conformal factor is defined as

$$e^{4\phi} = \gamma^{1/3} \equiv \det(\gamma_{ij})^{1/3}. \quad (3.12)$$

Now the evolution equations for the conformally decomposed 3-metric $\tilde{\gamma}_{ij}$ and the conformal factor ϕ are written as

$$D_t\tilde{\gamma}_{ij} = -2\alpha\tilde{A}_{ij}, \quad (3.13)$$

$$D_t\phi = -\frac{1}{6}\alpha K. \quad (3.14)$$

The evolution equation for mean Curvature K is also derived as

$$D_tK = -\gamma^{ij}\nabla_i\nabla_j\alpha + \alpha(\tilde{A}_{ij}\tilde{A}^{ij} + \frac{1}{3}K^2 + \frac{1}{2}(\rho + S)). \quad (3.15)$$

Regarding the form of the evolution equation for the conformally decomposed trace-free extrinsic curvature \tilde{A}_{ij} , there are different possible choices. A commonly used form is

$$D_t\tilde{A}_{ij} = e^{-4\phi}(-\nabla_i\nabla_j\alpha + \alpha(R_{ij} - S_{ij}))^{TF} + \alpha(K\tilde{A}_{ij} - 2\tilde{A}_{il}\tilde{A}_j^l), \quad (3.16)$$

where $(N_{ij})^{TF}$ refers to the trace-free part of a 3-dimensional 2-rank tensor N_{ij} , so $(N_{ij})^{TF} \equiv N_{ij} - \gamma_{ij}N_k^k/3$. The Ricci tensor in the equation (3.16) is decomposed as

$$R_{ij} = \tilde{R}_{ij} + R_{ij}^\phi, \quad (3.17)$$

where the part including the conformal factor ϕ is

$$R_{ij}^\phi = -2\tilde{\nabla}_i \tilde{\nabla}_j \phi - 2\tilde{\gamma}_{ij} \tilde{\nabla}^l \tilde{\nabla}_l \phi + 4\tilde{\nabla}_i \phi \tilde{\nabla}_j \phi - 4\tilde{\gamma}_{ij} \tilde{\nabla}^l \phi \tilde{\nabla}_l \phi, \quad (3.18)$$

while the other part is

$$\tilde{R}_{ij} = -\frac{1}{2}\tilde{\gamma}^{lm}\partial_l\partial_m\tilde{\gamma}_{ij} + \tilde{\gamma}_{k(i}\partial_j)\tilde{\Gamma}^k + \tilde{\Gamma}^k\tilde{\Gamma}_{(ij)k} + \tilde{\gamma}^{lm}(2\tilde{\Gamma}_{l(i}\tilde{\Gamma}_{j)km} + \tilde{\Gamma}_{im}^k\tilde{\Gamma}_{klj}), \quad (3.19)$$

where $\Gamma_{\mu\rho}^\sigma$ is the Christoffel symbols, and here $\tilde{\Gamma}^i \equiv \tilde{\gamma}^{jk}\tilde{\Gamma}_{jk}^i = -\partial_j\tilde{\gamma}^{ij}$ is treated as new variables for the set of BSSNOK equations. The evolution equation for $\tilde{\Gamma}^i$ [5] is

$$\begin{aligned} \partial_t\tilde{\Gamma}^i &= -2\tilde{A}^{ij}\partial_j\alpha + 2\alpha(\tilde{\Gamma}_{jk}^i\tilde{A}^{kj} - \frac{2}{3}\tilde{\gamma}^{ij}\partial_j K - \tilde{\gamma}^{ij}S_j + 6\tilde{A}^{ij}\partial_j\phi) \\ &\quad - \partial_j(\beta^l\partial_l\tilde{\gamma}^{ij} - 2\tilde{\gamma}^{m(j}\partial_m\beta^{i)}) + \frac{2}{3}\tilde{\gamma}^{ij}\partial_l\beta^l. \end{aligned} \quad (3.20)$$

Here the set of equations of (3.13),(3.14),(3.15),(3.16),(3.20) is the BSSNOK formalism for the variables of $\{\phi, K, \tilde{\gamma}_{ij}, \tilde{A}_{ij}, \tilde{\Gamma}^i\}$.

3.3 Gauge conditions

The gauge condition we adopt for our simulations is “1+log” slicing condition [17] for the lapse, imposed by the following hyperbolic K-driver slicing condition

$$(\partial_t - \beta^i\partial_i)\alpha = -f(\alpha)\alpha^2(K - K_0), \quad (3.21)$$

with $f(\alpha) = 2/\alpha$ and $K_0 \equiv K(t = 0)$. This choice of gauge condition allows for robust numerical simulations also in the presence of black holes. While, for the shift we use the hyperbolic Gamma-driver condition [6]

$$\partial_t^2\beta^i = F\partial_t\tilde{\Gamma}^i - \eta\partial_t\beta^i, \quad (3.22)$$

where F and η are chosen empirically in order to avoid strong oscillations in the shift [12]. Typical values are $F = 0.75$ and $\eta = 3$. This gauge condition acts so as to reduce the oscillation of $\tilde{\Gamma}^i$ and β .

3.4 “Valencia” formulation

In our numerical code we use the so called “Valencia” formulation [8] to deal with the matter and magnetic field dynamics. Here we briefly review the formulation.

At first we assume an Eulerian observer, who is moving with a four-velocity \mathbf{n} perpendicular to a spacial hypersurface. Then 3-velocity of the fluid seen from this observer is

$$v^i = \frac{h^i_\mu u^\mu}{-u^\mu n_\mu} = \frac{u^i}{W} + \frac{\beta^i}{\alpha}, \quad (3.23)$$

where $h_{\mu\nu} \equiv g_{\mu\nu} + n_\mu n_\nu$ is the projector onto the hypersurface orthogonal to \mathbf{n} (identical to the spacial metric $\gamma_{\mu\nu}$), \mathbf{u} is the 4-velocity of the fluid, and $-u^\mu n_\mu = \alpha u^0 = W$ is the Lorentz factor.

3.4.1 Induction equations for electromagnetic field

Maxwell equations can be expressed in 4-dimensional spacetime by the Faraday tensor $F^{\mu\nu}$ as follows

$$\nabla_\nu {}^*F^{\mu\nu} = 0, \quad (3.24)$$

$$\nabla_\nu F^{\mu\nu} = 4\pi J^\mu, \quad (3.25)$$

where ∇_ν is the covariant derivative with respect to 4-metric $g_{\mu\nu}$, J^μ is the charge current 4-vector, and ${}^*F^{\mu\nu}$ is the dual of the Faraday tensor defined as

$${}^*F^{\mu\nu} = \frac{1}{2} \eta^{\mu\nu\lambda\delta} F_{\lambda\delta}, \quad (3.26)$$

here $\eta^{\mu\nu\lambda\delta}$ is the Levi-Civita pseudo tensor. At this point we can introduce the magnetic induction field B^α and the electric field E^α seen from an observer moving with the 4-velocity \mathbf{U} ,

$$E^\alpha \equiv F^{\alpha\beta} U_\beta, \quad (3.27)$$

$$B^\alpha \equiv {}^*F^{\alpha\beta} U_\beta. \quad (3.28)$$

Now we assume ideal MHD condition, in which the fluid is a perfect conductor so the electric conductivity of the fluid is infinite. Under this condition, $F^{\mu\nu} u_\nu = 0$ needs to be fulfilled, because the charge current (generally expressed as $J^\mu = qu^\mu + \sigma F^{\mu\nu} u_\nu$, where q is the proper charge density and σ is the electric conductivity of the fluid) would be infinite under the ideal MHD condition ($\sigma \rightarrow \infty$) if the condition $F^{\mu\nu} u_\nu = 0$ was violated.

Now we can rewrite the Faraday tensor in terms of the magnetic field b^μ measured by the comoving observer with the fluid as follows

$$F^{\nu\sigma} = \eta^{\alpha\mu\nu\sigma} b_\alpha u_\mu. \quad (3.29)$$

And by taking the dual of this expression,

$$*F^{\mu\nu} = b^\mu u^\nu - b^\nu u^\mu \quad (3.30)$$

can be derived. Now Maxwell equations (3.24),(3.25) are written as

$$\nabla_\nu *F^{\mu\nu} = \frac{1}{\sqrt{-g}} \partial_\nu (\sqrt{-g} (b^\mu u^\nu - b^\nu u^\mu)) = 0, \quad (3.31)$$

where $g \equiv \det(g_{\mu\nu})$. To further rewrite Maxwell equations in terms of quantities measured by an Eulerian observer, it is necessary to convert b^μ , measured in the comoving frame, to B^μ , measured in the Eulerian frame. We introduce the projection operator $P_{\mu\nu} \equiv g_{\mu\nu} + u_\mu u_\nu$ regarding the 4-velocity of the fluid \mathbf{u} . Using this operator we can relate b^μ to B^μ as follows

$$b^0 = \frac{WB^i v_i}{\alpha}, \quad (3.32)$$

$$b^i = \frac{B^i + \alpha b^0 u^i}{W}, \quad (3.33)$$

$$b^2 = b^\mu b_\mu = \frac{B^2 + \alpha^2 (b^0)^2}{W^2}, \quad (3.34)$$

where $B^2 \equiv B^i B_i$. Now it is possible to rewrite Maxwell equations. The divergence-free condition of magnetic field is

$$\partial_i \tilde{B}^i = 0, \quad (3.35)$$

where $\tilde{B}^i \equiv \sqrt{\gamma} B^i$, and the induction equations of magnetic field are

$$\partial_t(\tilde{B}^i) = \partial_j (\tilde{v}^i \tilde{B}^j - \tilde{v}^j \tilde{B}^i), \quad (3.36)$$

where $\tilde{v}^i \equiv \alpha v^i - \beta^i$.

3.4.2 Conservative form of GRMHD equations

For evolving set of quantities related to matter and magnetic field dynamics, including rest-mass density ρ , specific internal energy ϵ , pressure p , 3-velocity of the fluid v^i , and magnetic field, we need to rewrite related equations in conservative form, which is suited for High-Resolution Shock-Capturing methods used in many simulations including ours.

The equations of motion of the fluid consist of the following two parts.

The conservation of baryon number of the fluid

$$\nabla_\nu(\rho u^\nu) = 0. \quad (3.37)$$

The conservation of energy-momentum of the fluid

$$\nabla_\nu T^{\mu\nu} = 0. \quad (3.38)$$

Now we assume that the fluid is a perfect fluid. Then the energy-momentum tensor for the fluid is

$$T^{\mu\nu} = T_{\text{fluid}}^{\mu\nu} + T_{\text{em}}^{\mu\nu}, \quad (3.39)$$

$$T_{\text{fluid}}^{\mu\nu} = \rho h u^\mu u^\nu + p g^{\mu\nu}, \quad (3.40)$$

$$T_{\text{em}}^{\mu\nu} = \frac{1}{4\pi} (F^{\mu\lambda} F_\lambda^\nu - \frac{1}{4} g^{\mu\nu} F^{\lambda\delta} F_{\lambda\delta}) = (u^\mu u^\nu + \frac{1}{2} g^{\mu\nu}) b^2 - b^\mu b^\nu, \quad (3.41)$$

here $h \equiv 1 + \epsilon + p/\rho$ is the specific relativistic enthalpy. $T_{\text{fluid}}^{\mu\nu}$ denotes the stress-energy tensor for non-magnetized perfect fluid, and $T_{\text{em}}^{\mu\nu}$ denotes the stress-energy tensor related to electromagnetic field. Then the stress-energy tensor for magnetized perfect fluid is sum of the two, as shown.

The energy-momentum for the fluid is then written as

$$T^{\mu\nu} = (\rho h + b^2) u^\mu u^\nu + (p + \frac{b^2}{2}) g^{\mu\nu} - b^\mu b^\nu. \quad (3.42)$$

Now we can rewrite equations for matter dynamics (3.37), (3.38) and magnetic field (3.36) in a conservative form

$$\frac{1}{\sqrt{-g}} [\partial_t(\sqrt{\gamma} \mathbf{F}^0) + \partial_i(\sqrt{-g} \mathbf{F}^i)] = \mathbf{S}, \quad (3.43)$$

where \mathbf{F}^0 is the vector of conserved variables seen from an Eulerian observer

$$\mathbf{F}^0 = \begin{pmatrix} D \\ S_j \\ \tau \\ B^k \end{pmatrix}, \quad (3.44)$$

\mathbf{F}^i are the fluxes

$$\mathbf{F}^i = \begin{pmatrix} D\tilde{v}^i/\alpha \\ S_j \tilde{v}^i/\alpha + (p + b^2/2)\delta_j^i - b_j B^i/W \\ \tau \tilde{v}^i/\alpha + (p + b^2/2)v^i - \alpha b^0 B^i/W \\ B^k \tilde{v}^i/\alpha - B^i \tilde{v}^k/\alpha \end{pmatrix}, \quad (3.45)$$

and \mathbf{S} is the source terms

$$\mathbf{S} = \begin{pmatrix} 0 \\ T^{\mu\nu}(\partial_\mu g_{\nu j} - \Gamma_{\nu\mu}^\delta g_{\delta j}) \\ \alpha(T^{\mu 0} \partial_\mu \ln \alpha - T^{\mu\nu} \Gamma_{\nu\mu}^0) \\ 0^k \end{pmatrix}, \quad (3.46)$$

where

$$D \equiv \rho W, \quad (3.47)$$

$$S_j \equiv (\rho h + b^2) W^2 v_j - \alpha b^0 b_j, \quad (3.48)$$

$$\tau \equiv (\rho h + b^2) W^2 - (p + \frac{b^2}{2}) - \alpha^2 (b^0)^2 - D, \quad (3.49)$$

$$0^k = (0, 0, 0)^T. \quad (3.50)$$

This is the ‘‘Valencia’’ formulation we use to evolve matter and magnetic field. To actually solve this set of equations, we need additionally an equation of state of the fluid matter, which relates the pressure to the rest-mass density and the specific internal energy $p = p(\rho, \epsilon)$.

3.5 Extracting GW signals

While there are several ways of extracting the waveforms of gravitational waves, we choose the gauge-invariant Moncrief formalism [60, 61]. In this method metric is decomposed into the Schwarzschild metric and a perturbation metric. By calculating the gauge-invariant Moncrief functions (for even-parity $\Psi_{lm}^{(e)}$ and for odd-parity $Q_{lm}^{(o)}$) at a spherical surface far from the objects emitting GWs, one can extract the content of GWs (the perturbation of the metric from the Schwarzschild metric),

$$Q_{lm}^+ = \lambda \Psi_{lm}^{(e)}, \quad (3.51)$$

$$Q_{lm}^\times = \lambda Q_{lm}^{(o)}, \quad (3.52)$$

where $\lambda \equiv \sqrt{2(l+2)!/(l-2)!}$. From these quantities we can calculate gravitational wave amplitudes for + and \times polarizations as follows:

$$h_+ - ih_\times = \frac{1}{2r} \sum_{l,m} \left(Q_{lm}^+ - i \int_{-\infty}^t Q_{lm}^\times(t') dt' \right) {}_{-2}Y^{lm}, \quad (3.53)$$

where ${}_{-2}Y^{lm}$ is the $s = -2$ spin-weighted spherical harmonic.

Chapter 4

Numerical methods

In this chapter we present the numerical methods for solving the equations described in the previous chapter. We make use of the full GRMHD code Whisky [37, 36, 33], which is based on the public code Einstein Toolkit [56], to conduct our numerical simulations. The initial data are computed using the spectral-method code LORENE (<http://www.lorene.obspm.fr>).

4.1 Evolution method for spacetime curvature

The spacetime is evolved using the BSSNOK formalism via the McLachlan code [18, 70] in the Einstein Toolkit. This code solves the set of equations shown in the section of BSSNOK formalism (3.13), (3.14), (3.15), (3.16), (3.20) for the variables of $\{\phi, K, \tilde{\gamma}_{ij}, \tilde{A}_{ij}, \tilde{\Gamma}^i\}$. The code uses finite difference schemes and adds a Kreiss-Oliger dissipation term to remove high-frequency noise.

4.2 HRSC method

High-Resolution Shock-Capturing (HRSC) methods [32] can solve the conservative form of GRMHD equations (3.43) properly in the presence of shocks. At first, we set coordinates that are parameterized by a time coordinate t , and spacial coordinates x, y, z in the spacetime. Now we focus on a single computational cell at (t, x, y, z) , which is bounded spatially by surfaces at $x^i - \Delta x^i/2$ and $x^i + \Delta x^i/2$. Then the integral form of equation (3.43) is

$$\int \partial_t(\sqrt{\gamma}\mathbf{F}^0)d\Omega = - \int \partial_i(\sqrt{-g}\mathbf{F}^i)d\Omega + \int \sqrt{-g}\mathbf{S}d\Omega, \quad (4.1)$$

where $d\Omega \equiv dt dx dy dz$. This integral form can be rewritten as

$$\begin{aligned}
(\Delta V \bar{\mathbf{F}}^0)|_{t+\Delta t} - (\Delta V \bar{\mathbf{F}}^0)|_t &= - \int_{x+\Delta x/2} (\sqrt{-g} \mathbf{F}^x) dt dy dz + \int_{x-\Delta x/2} (\sqrt{-g} \mathbf{F}^x) dt dy dz \\
&\quad - \int_{y+\Delta y/2} (\sqrt{-g} \mathbf{F}^y) dt dx dz + \int_{y-\Delta y/2} (\sqrt{-g} \mathbf{F}^y) dt dx dz \\
&\quad - \int_{z+\Delta z/2} (\sqrt{-g} \mathbf{F}^z) dt dx dy + \int_{z-\Delta z/2} (\sqrt{-g} \mathbf{F}^z) dt dx dy \\
&\quad + \int \sqrt{-g} \mathbf{S} d\Omega,
\end{aligned} \tag{4.2}$$

where $\bar{\mathbf{F}}^0$ is defined as

$$\bar{\mathbf{F}}^0 \equiv \frac{1}{\Delta V} \int_{\Delta V} \sqrt{\gamma} \mathbf{F}^0 dx dy dz, \tag{4.3}$$

where

$$\Delta V \equiv \int_{x-\Delta x/2}^{x+\Delta x/2} \int_{y-\Delta y/2}^{y+\Delta y/2} \int_{z-\Delta z/2}^{z+\Delta z/2} \sqrt{\gamma} dx dy dz. \tag{4.4}$$

Here we introduce the numerical fluxes $\hat{\mathbf{F}}^i$, which are defined at the boundaries of computational cells, and defined as the time average of the fluxes,

$$\hat{\mathbf{F}}^i \equiv \frac{1}{\Delta t} \int_t^{t+\Delta t} \sqrt{-g} \mathbf{F}^i dt. \tag{4.5}$$

Now we obtain the following equation by dividing the equation (4.2) by ΔV if we ignore the source term for the time being,

$$\frac{(\bar{\mathbf{F}}^0)|_{t+\Delta t} - (\bar{\mathbf{F}}^0)|_t}{\Delta t} = \sum_{i=1,3} \frac{(\hat{\mathbf{F}}^i)|_{x^i-\Delta x^i/2} - (\hat{\mathbf{F}}^i)|_{x^i+\Delta x^i/2}}{\Delta x^i}. \tag{4.6}$$

In practice we treat the values of \mathbf{F}^0 at each numerical cell as the average values $\bar{\mathbf{F}}^0$, and we take into account the source term \mathbf{S} in the numerical evolution, then we calculate the conserved equation numerically as follows,

$$\frac{d\mathbf{F}^0}{dt} = \frac{d\bar{\mathbf{F}}^0}{dt} = \sum_{i=1,3} \frac{(\hat{\mathbf{F}}^i)|_{x^i-\Delta x^i/2} - (\hat{\mathbf{F}}^i)|_{x^i+\Delta x^i/2}}{\Delta x^i} + \mathbf{S}. \tag{4.7}$$

4.3 Reconstruction of primitive values

To compute the numerical fluxes in the equation (4.7), one needs to reconstruct primitive variables (ρ, v^i, ϵ) at the interfaces between the numerical cells in each step of

evolution. For the interpolation of numerical values we adopt the Piecewise Parabolic Method [22] for its balance of accuracy and computational efficiency. Since our scheme evolves the conserved variables while the fluxes need the primitive variables to be computed, at the end of each time step we need to compute the primitive variables from the conservative ones by solving the set of equations (3.47)-(3.49). This requires to solve for a system of five equations in five unknowns. By using the "2D" method described in [37] we reduce the problem to the solution of two equations in two unknown via a Newton-Raphson scheme.

4.4 Riemann solver

Since the numerical fluxes are defined on the boundaries between the numerical cells, the fluxes are determined by solving a Riemann problem with the parameters obtained by reconstruction of primitive variables in the numerical cells. Since solving the Riemann problem analytically is difficult due to the complexity of the equations, we use the approximate Riemann solver HLLC [40] to solve the problem numerically.

4.5 Modified Lorenz gauge

In order to keep the magnetic field to be divergence-free during the evolution, we evolve the vector potential of the field instead of the magnetic field itself. Under the ideal MHD condition the evolution equations for the vector potential \mathbf{A} can be written as [36]

$$\partial_t \mathbf{A} = -\mathbf{E}, \quad (4.8)$$

where \mathbf{E} denotes the electric field at the center of each numerical cell, which is calculated by interpolating fluxes at the interfaces of the cells. Then the magnetic field is calculated at the center of each cell by taking the curl of the vector potential.

We choose "Modified Lorenz gauge" [30, 31] for evolving the vector potential in order to suppress the spurious amplification of magnetic fields at the boundaries between different refinement levels of numerical grids.

4.6 Atmosphere

The conservative equation (3.43) has a singularity if the rest-mass density is zero (i.e., if we are in a vacuum region). To avoid this problem, we replace vacuum regions with an artificial "atmosphere" for all the grid points outside the stars, where very low, but non-zero constant rest-mass density is initially set. The value of rest-mass density is chosen as small as possible in order to suppress the effect of this artificial density onto the physical dynamics.

4.7 Excision

We excise the region inside the apparent horizon after the formation of a black hole by setting the hydrodynamic variables to the values in the atmosphere, so that the

calculation of the primitive variables from the conservative ones does not fail due to very high magnetic field amplification that may occur inside a black hole. The region of apparent horizon is determined by the apparent horizon finder of Thornburg [84].

Chapter 5

General relativistic magnetohydrodynamic simulations of binary neutron star mergers with the APR4 equation of state

In this chapter I present the results of simulations published in one of our papers [29], in particular the part associated with the “high-mass” models whose simulations were done by me. The other simulations, “low-mass” and “unequal-mass” simulations were done by another PhD student of our group (Andrea Endrizzi). The figures presented in this chapter, as well as part of the text, were published in [29].

5.1 Models

We employ a piecewise polytropic approximation of the APR4 EOS [4] as the EOS for neutron matter. The parameters for the polytropic segments are taken from [69]. In addition, we take into account thermal effects by adding thermal component to the EOS,

$$P(\rho, \epsilon) = P_{cold}(\rho) + (\Gamma_{th} - 1)(\epsilon - \epsilon_{cold}(\rho))\rho \quad (5.1)$$

where $\Gamma_{th} = 1.8$. Further, we noticed that the piecewise polytropic approximation [69] of the APR4 EOS is only causal up to a density of $1.45 \times 10^{15} g/cm^3$, above which the sound speed becomes superluminal. The critical density is larger than the central density of all the NSs used for our initial data. During the evolution however, the density can exceed this value, either during a short period when the stars are merging or while undergoing collapse to a BH. We therefore add two more high-density pieces, one with $\Gamma = 3$ and starting at density $1.4 \times 10^{15} g/cm^3$, and one with $\Gamma = 2$ for densities above $1.61 \times 10^{15} g/cm^3$. The resulting hybrid EOS is fully causal (regardless of temperature), although it is probably not particularly realistic in the high density part.

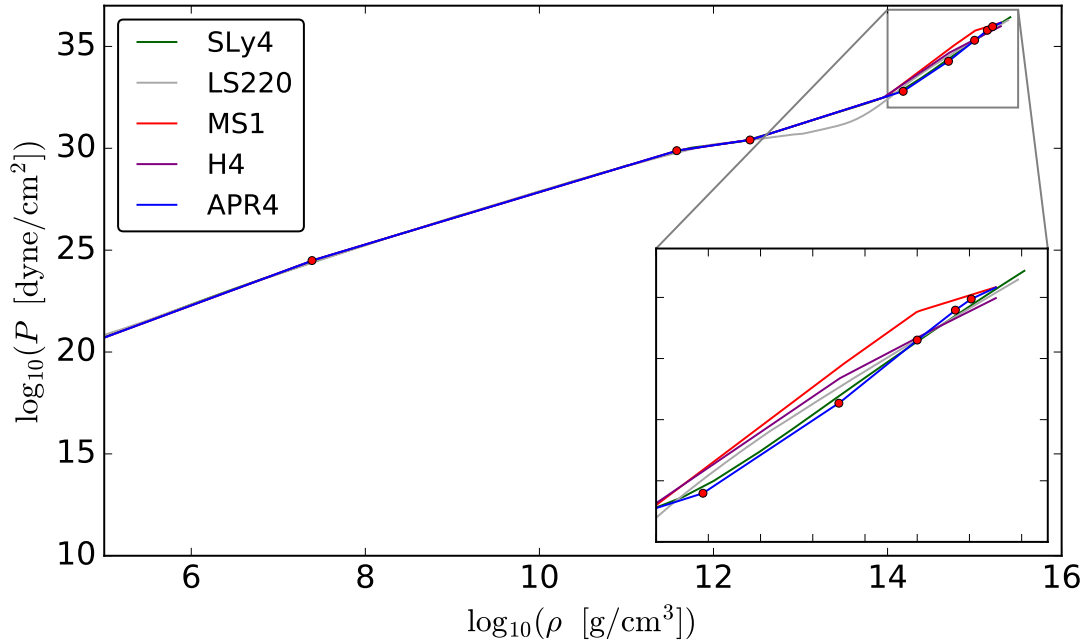


Figure 5.1 Pressure versus rest mass density relation for the piecewise polytropic approximation of the APR4 EOS used in this work. For comparison, we also show some other EOSs.

Figure 5.1 shows pressure versus rest mass density for the cold part in comparison to other well known EOSs. They differ only at high densities, since the EOS for the density range of the NS crust is better constrained by current understanding of nuclear physics. We should note that the same low density EOS is used together with the added thermal part for the evolution of ejected matter. Since such matter is shock-heated, we expect the thermal part to dominate in this regime. We computed sequences of TOV stars as well as uniformly rotating stars with maximal rotation using the piecewise polytropic APR4 EOS. Figure 5.2 shows the baryonic mass versus the central density for these sequences. We find that the supramassive mass range lies between $2.61\text{--}3.07M_{\odot}$.

We evolve three different initial models, which are summarized in Table 5.1. The first (“high mass”, HM) is an equal mass model with total mass in the hypermassive range (cf. Figure 5.2), which can either form a metastable HMNS or directly collapse to a BH. The second equal mass model is in the supramassive mass range and expected to form a long-lived remnant (“low mass”, LM). Our third model is an unequal mass binary with mass ratio 0.905 (“unequal mass”, UM). Although its total mass is in the upper supramassive regime, the resulting remnant can be somewhat lighter since unequal mass models typically form more massive disks during merger.

Each of the three models is evolved with and without an initial magnetic field. Since the LORENE code cannot yet compute magnetized BNS models, we manually add a

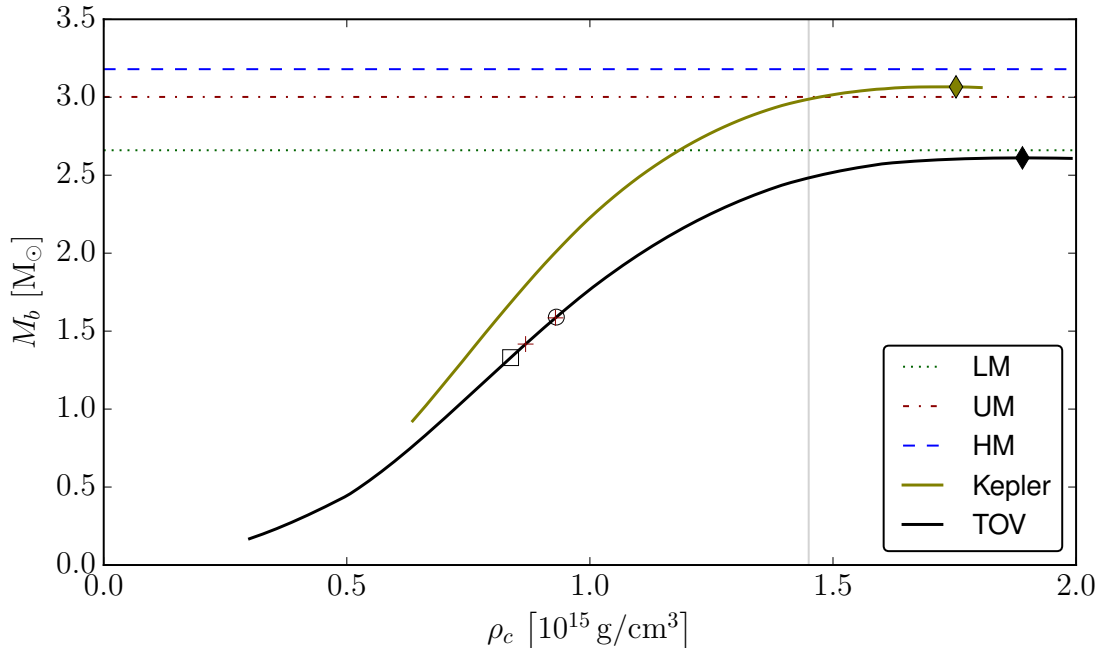


Figure 5.2 Total baryonic mass as function of the central rest mass density, for nonrotating NSs and for uniformly rotating NSs at the mass-shedding limit, employing the EOS used for all our initial data. The horizontal lines correspond to the total baryonic masses of the three models we evolved. The individual stars of the low-, unequal-, and high-mass binaries are marked by square, plus, and circle markers, respectively. The diamond symbols denote maximum mass models. The vertical line marks the density where the original APR4 approximation given in [69] becomes non-causal and had to be modified.

poloidal magnetic field using a simple analytic prescription for the vector potential:

$$A_\phi \equiv \varpi^2 A_b \max(p - p_{\text{cut}}, 0)^{n_s}, \quad (5.2)$$

where ϖ is the coordinate distance to the NS axis (orthogonal to the orbital plane). The field is confined to the NSs, using a cutoff pressure $p_{\text{cut}} = 0.04$ of the maximum (central) pressure. The exponent $n_s = 2$ determines the degree of differentiability of the potential [36]. The strength of the field, determined by A_b , is chosen such that the maximum field strength is $1.0 \times 10^{13} G$. For the unequal mass model, this is done separately for each star. The corresponding magnetic energy (see Table 5.1) is below 10^{-11} of the NS binding energy. Hence we can neglect the impact on the hydrostatic equilibrium, and also the violation of the general relativistic constraints. We stress however that finding a stable magnetic field configuration for NSs is still an unsolved problem. The prescribed magnetic field topology will decay into an unordered field during the inspiral.

Though we confine the magnetic field to the NS interior, as the ideal MHD approximation is valid only inside the NSs, we do not think this assumption affects the numerical

Table 5.1 Initial data parameters. M_b is the total baryonic mass of the systems and d denotes initial proper separation, both parameters are given to Lorene to produce initial data. f_0 is the initial orbital frequency calculated by Lorene. For all the models we calculated TOV sequence of single star, whose mass corresponds to M_g , the gravitational mass of each star at infinite separation, and whose circumference radius R_c is used for calculating the compactness of each star M_g/R_c (dimensionless). $q = M_g^1/M_g^2$ denotes the mass ratio. The total magnetic energy in the system is calculated as $E_{\text{mag}} \equiv \int_V n_\mu n_\nu T_{\text{em}}^{\mu\nu} W \sqrt{\gamma} d^3x / W$ (See [27]). According to this calculation, E_B is the initial magnetic energy of the magnetized models, which are otherwise identical to the non-magnetic ones.

Model	HM	LM	UM
q	1	1	0.905
M_b [M_\odot]	3.18	2.66	3.01
M_g [M_\odot]	1.43	1.22	1.29, 1.42
M_g/R_c	0.186	0.159	0.168, 0.186
f_0 [Hz]	288	270	282
d [km]	60.0	57.5	59.0
E_B [10^{42} erg]	1.58	1.52	1.55

results qualitatively compared with the results obtained if we instead assume dipolar magnetic fields. Ruiz et al [76] presents results in which both the models with dipolar-like magnetic fields and confined fields launch jets via NS-NS mergers. The launch of jets seems to be due to the very high initial magnetic field strength ($\sim 10^{15}$ G), and seems not to be related to the initial configuration of magnetic fields.

5.2 Numerical setups

Though basic setups for numerical evolutions are already presented in the previous chapter, in particular for the APR4 simulations, the density of atmosphere is $\rho_a \approx 6.2 \times 10^6 \text{g/cm}^3$. Regarding the adaptation of meshes for the space, adaptive mesh refinement is implemented via the Carpet driver which is part of the Einstein toolkit. In all the simulations we employed 6 refinement levels, with a resolution of $0.15M_\odot \approx 222m$ for the finest level. During inspiral, the two finest levels follow the NSs, which are completely contained in the larger fixed grids (see Figures 5.3 and 5.4). Shortly before merger, when two NSs approach within a given distance $\sim 1332m$, the moving grids are replaced by larger fixed grids. The smallest covers a radius of $\sim 30km$, sufficient to contain the post-merger remnant. The outer boundary is located at $\sim 794km$. In order to save computational resources, we apply reflection symmetry with respect to the equatorial plane.

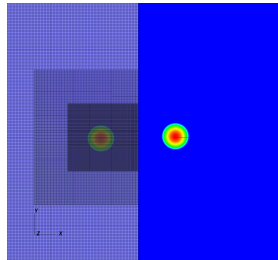


Figure 5.3 Plot of the rest-mass density and grid setup on the equatorial plane at the beginning of the simulation. The right-hand side of the mesh is clipped for clear visualization.

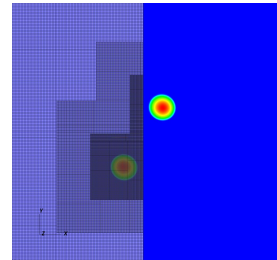


Figure 5.4 Like Figure 5.3, but during the inspiral phase. One can see that the two finest grids are following the stars while the other outer grids are kept fixed.

5.3 Results

5.3.1 General dynamics

In the “high-mass” models binary neutron stars complete 5 orbits before merger in either of magnetized or non-magnetized cases, while “unequal-mass” and “low-mass” models complete 6 and 8 orbits, respectively, regardless of the existence of magnetic fields. The influence of magnetic fields on general dynamics seems very small. In Figure 5.5 we show the dynamics of matter for the “high-mass” case. After merger, the remnant promptly collapses to form a black hole, and mass of the surrounding disk and the amount of ejected matter are negligibly small. While, the “unequal-mass” and “low-mass” models undergoes SMNS phases which are stable at least for the time lapse of our simulation, and surrounding disks and some ejected matter exist. In Figure 5.6 we show the plot of dimensionless BH spin for the “high-mass” model. The discontinuity between first ~ 1 ms after finding the apparent horizon and the other part is due to the failure of finding the apparent horizon during the first ~ 1 ms except for its first detection (black vertical line). See the detailed information for the outcome of simulations in Table 5.2.

5.3.2 Magnetic field evolution

The evolution of total magnetic energy for magnetized high-, low- and unequal-mass models are shown in Figure 5.7. As one can see, there is a moderate amplification already during the inspiral. There are several possible effects that might contribute to the evolution of the field. First, the chosen field configuration is known to be unstable and might re-arrange itself (we indeed observed that the magnetic field configuration changes slightly during inspiral), which is however unfavourable to amplify the field. A second possible cause could be fluid flows induced by tidal forces or GR effects, which is however purely speculative. A more likely cause is the imperfection of the initial data. The error due to the quasi-circular approximation might lead to some vortex-like, churning movements on top of more visible effects such as residual eccentricity and stellar oscillations. Numerical errors during the evolution can be ruled out as cause of the amplification, since we observe

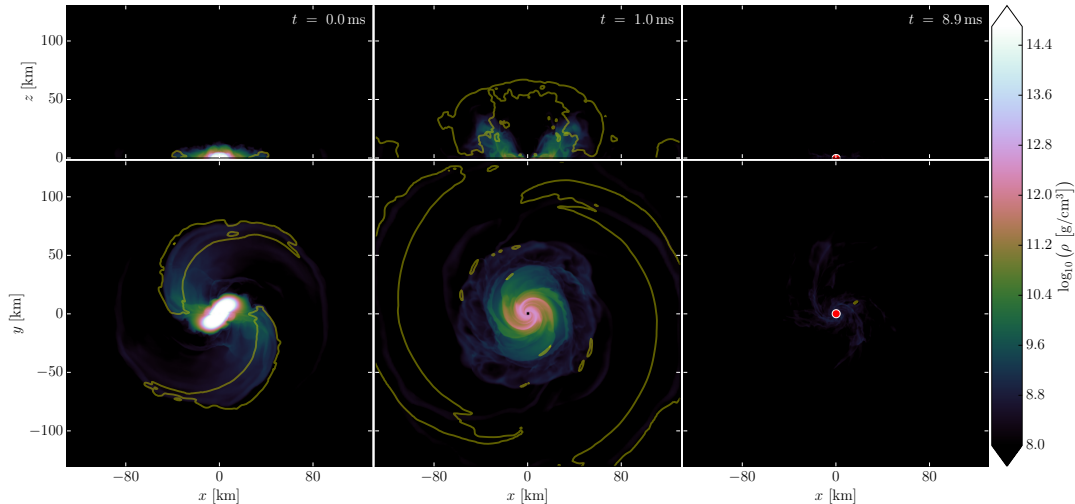


Figure 5.5 Snapshots of the evolution at 0, 1, and 8.9 ms after the merger, for model HM_B0. The top row show cuts in the xz -plane, the bottom row cuts in the orbital xy -plane. The color corresponds to the logarithmic rest mass density. The contour lines mark the boundaries of regions where matter is unbound (according to the geodesic criterion, $u_0 < -1$). The apparent horizon and its interior are drawn in white and red, respectively.

slightly more amplification during inspiral with better resolution, not less. In summary, we cannot tell if the amplification during inspiral is a generic feature or an artifact of our setup. In any case, we are not overly concerned about the changes during the inspiral since the actual field structure of BNS is completely unknown anyway and our setup is intended only as generic example of a magnetized merger. Moreover, we are confident that those changes do not influence the qualitative results in the post-merger phase which will be discussed in the following.

Regarding the high-mass case, it seems that the Kelvin-Helmholtz instability acts in the very late inspiral so as to amplify the magnetic field energy, since the remnant promptly collapses to a black hole, the matter and associated magnetic energy are swallowed at merger. The increase in magnetic energy occurring a few ms after merger seems to be due to the amplification of the magnetic field in low density matter falling back onto the black hole. While, in low- and unequal-mass cases, the magnetic field energy is amplified via the Kelvin-Helmholtz instability during merger, and also later time during the evolution of SMNS, and reaches a saturation.

5.3.3 GW signal

We extract the GW signal for all runs at a fixed radius of 738 km, and we perform no extrapolation to infinity, since the precision is likely limited by the accuracy of the hydrodynamic evolution. The $l = m = 2$ component of GWs, which is the largest one,

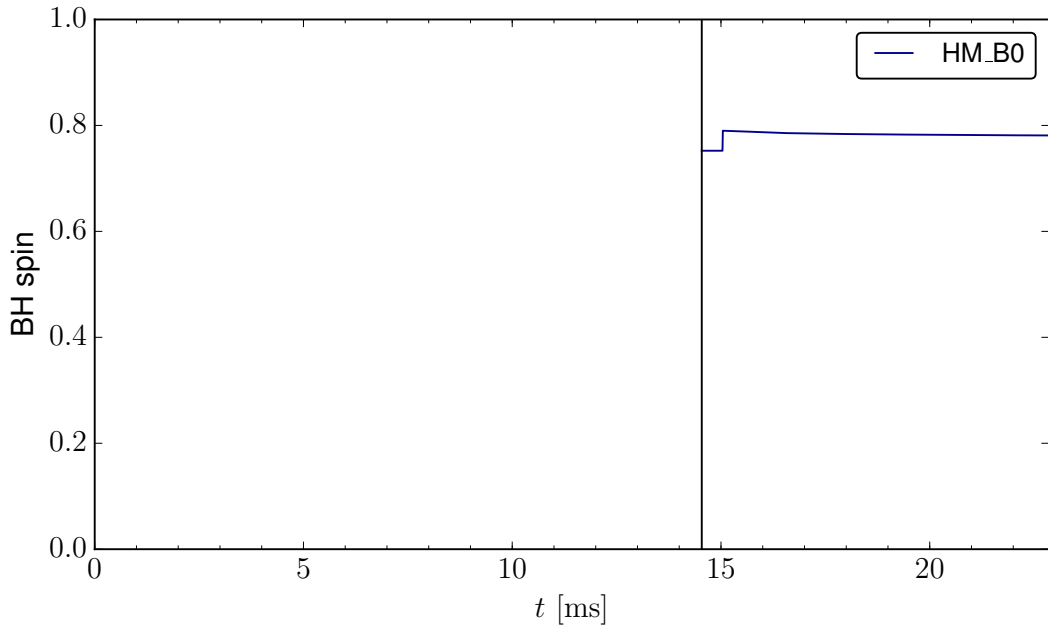


Figure 5.6 The time evolution of dimensionless BH spin $J_{\text{BH}}/M_{\text{BH}}^2$ for the model HM_B0. The vertical black line denotes the time of black hole formation.

are shown in Figure 5.8, for non-magnetized high-, low- and unequal-mass cases. For the high-mass case, since the remnant promptly collapses to a black hole after merger, the GW signal mainly consists of inspiral signal and black hole ringdown. While, for low- and unequal-mass cases, the GW signals consists of inspiral part and SMNS oscillation. The sudden drop in amplitude happening at ~ 3 ms in the unequal-mass model may be related to vortex rearrangements in the fluid after merger [46]. The following decay in the amplitude is instead probably due to the remnant becoming more axisymmetric and a similar effect is also observed in other simulations (e.g., [41]).

We now discuss the power spectra of the GW signal, given by $h_{\text{eff}}(f) = \sqrt{\tilde{h}_+^2(f) + \tilde{h}_\times^2(f)}$, where \tilde{h}_+ , \tilde{h}_\times are the Fourier transforms of coefficients $h_{22}^+(t)$, $h_{22}^\times(t)$. The spectra for all models are shown in Figure 5.9, in comparison to the sensitivity curves of GW detectors. At a distance of 100 Mpc, the inspiral phase of all our models will be visible with both advanced LIGO and Virgo, while the post-merger part of the spectrum for the low- and unequal-mass models will be barely visible. Note that our signal does not include the long term evolution of the remnant. Although the amplitude at the end of our simulation is quite low, a longer integration time might enhance its detectability (e.g. [24, 39]). This depends on the damping at late times and the stability of the frequency. The high-frequency side-peak of the unequal mass models will be barely visible with the Einstein telescope, while the one produced by the low-mass models is too faint. The frequency of the largest post-merger peak of the spectra is given in Table 5.2 for each model, together with the instantaneous frequency at merger time.

Table 5.2 Outcome of the mergers. M_e is our best estimate for the total ejected mass, computed by integrating the flux of rest-mass density across spherical surfaces at certain distances from the origin of the grids (The distance is chosen so that the amount of ejected matter becomes maximum within our initial guessed radii. See more detail in [29]). The average escape velocity is defined as $v_{\text{esc}} \equiv \sqrt{1 - W_\infty^{-2}}$, where $W_\infty \equiv -(\int u_0 \rho_u dV)/(\int \rho_u dV)$ is an average escape Lorentz factor (ρ_u is the density of ejected matter and dV is the proper volume element). See more detail about the average escape velocity in [29]. f_{pk} is the GW instantaneous frequency at merger time. If a BH is formed, M_{BH} and J_{BH} are its mass and angular momentum calculated by QuasiLocalMeasures (See [56]), extracted at the end of the simulations. For the models without BH, F_c and F_m denote the remnant's central and maximum rotation rates, computed 15 ms after the merger (See [29] about HMNS rotation profiles). Though there is neither a clear distinction between disk and fall-back component, nor between remnant and disk, we estimated disk mass M_d between $20 < r < 60$ km and fall-back mass M_f at $r > 60$ km, computed 15 ms after the merger. Finally, f_{pm} is the frequency of the largest peak in the post merger spectrum. Note that the missing of v_{esc} , M_d and M_f in the UMBO is simply because its simulation was done before the introduction of these measures.

Model	HMBO	HMB13	LMBO	LMB13	UMBO	UMB13
$M_{\text{BH}} [M_\odot]$	2.79	2.79	—	—	—	—
$J_{\text{BH}}/M_{\text{BH}}^2$	0.78	0.78	—	—	—	—
F_c [kHz]	—	—	0.52	0.49	0.67	0.66
F_m [kHz]	—	—	1.50	1.54	1.63	1.60
f_{pk} [kHz]	2.18	2.18	2.02	2.02	2.08	2.07
f_{pm} [kHz]	—	—	3.17	3.14	3.30	3.26
$M_e [M_\odot]$	$< 10^{-3}$	$< 10^{-3}$	0.002	0.003	0.010	0.010
$v_{\text{esc}} [c]$	—	—	0.13	0.12	—	0.12
$M_d [M_\odot]$	—	—	0.130	0.091	—	0.119
$M_f [M_\odot]$	0.001	0.001	0.085	0.085	—	0.112

5.3.4 Constraints violation

To check the numerical accuracy of the simulations, we show the time evolutions of the Hamiltonian and momentum constraints for the magnetized high-, low- and unequal-mass models in Figures 5.10, 5.11 and 5.12, respectively. Though we do not show the cases of unmagnetized models, the constraint violations are almost the same as in the magnetized cases, so the effect of magnetic fields on the Hamiltonian and momentum constraints is almost negligible.

In all the three models, the values of the Hamiltonian and momentum constraints are almost the same during inspiral ($\sim 10^{-2}$ and $\sim 10^{-4}$, respectively). After merger, in the high-mass model a black hole is promptly formed and both the constraints settle down to $\sim 10^{-3}$, while in the low- and unequal-mass models the Hamiltonian constraint continues to increase to $\sim 10^{-1}$ until the end of our simulations, and the momentum constraints settle down to $\sim 10^{-3}$ slowly with oscillation since the HMNSs survive for these cases. Note that the flat lines of constraints continuing for ~ 1 ms after the black hole formation in the

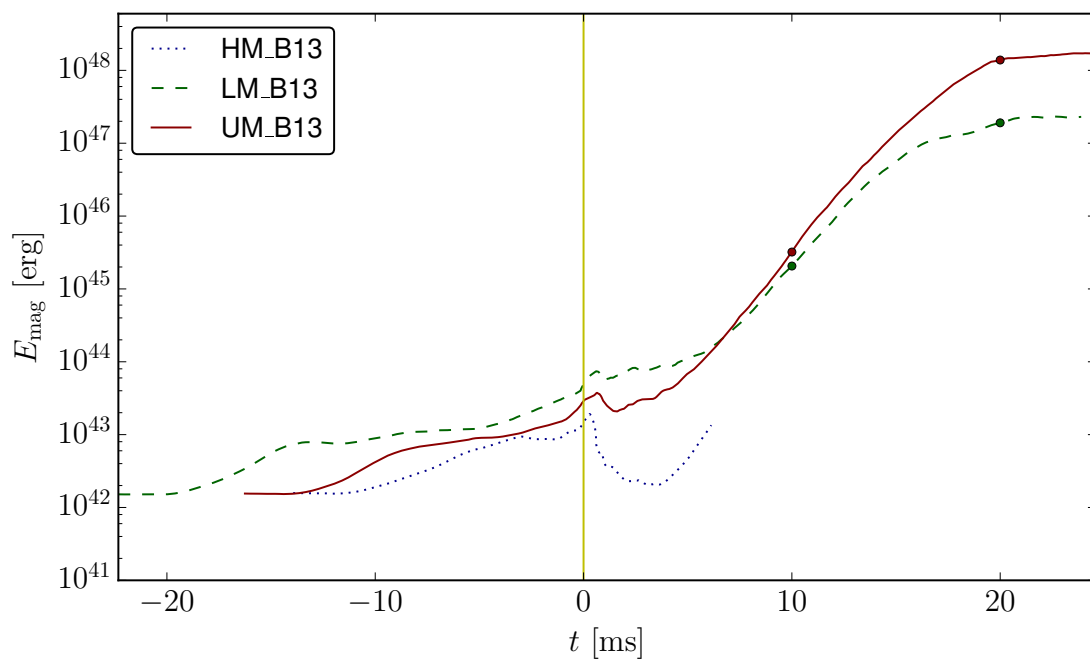


Figure 5.7 Evolution of the total magnetic energy for the three magnetized models: high-mass (blue dotted), low-mass (green dashed), and unequal-mass (solid red). The vertical line marks the time of merger $t = 0$.

high-mass model are due to the failure of finding the apparent horizon during this period except for its first detection (the vertical black line).

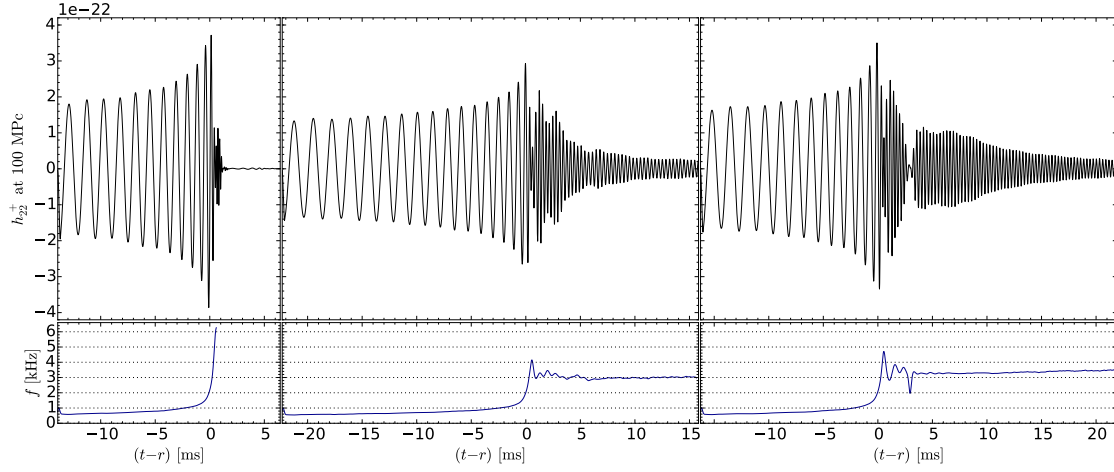


Figure 5.8 Gravitational wave signal for models HM_B0, LM_B0, and UM_B0 (from left to right). The top panels show the strain at nominal distance of 100 Mpc. The lower panels show the instantaneous frequency.

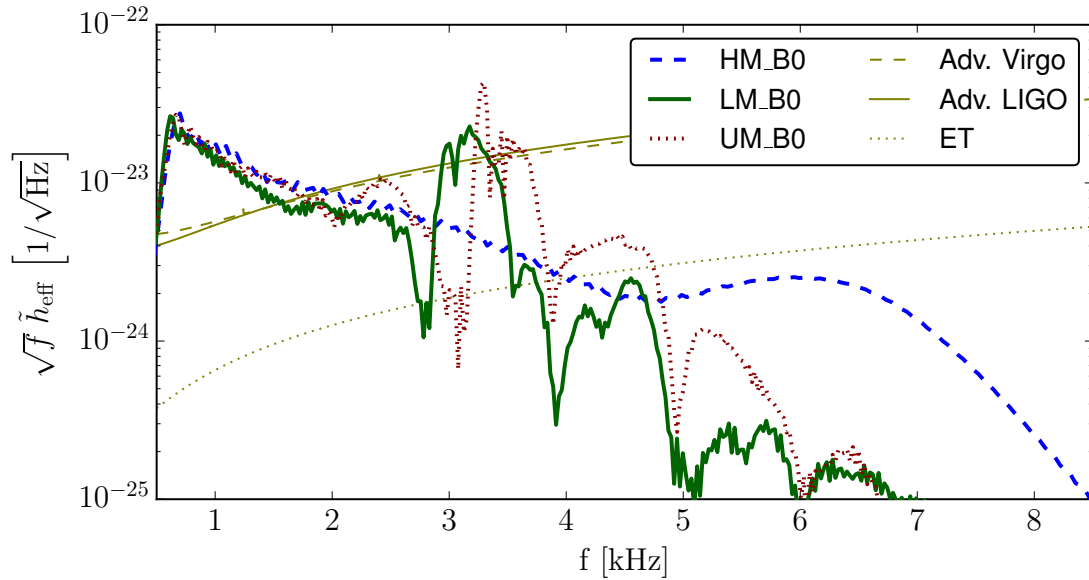


Figure 5.9 Gravitational wave spectra (thick lines) for the three models in comparison to the sensitivity curves of GW detectors (thin lines). The strain is given at distance of 100 Mpc.

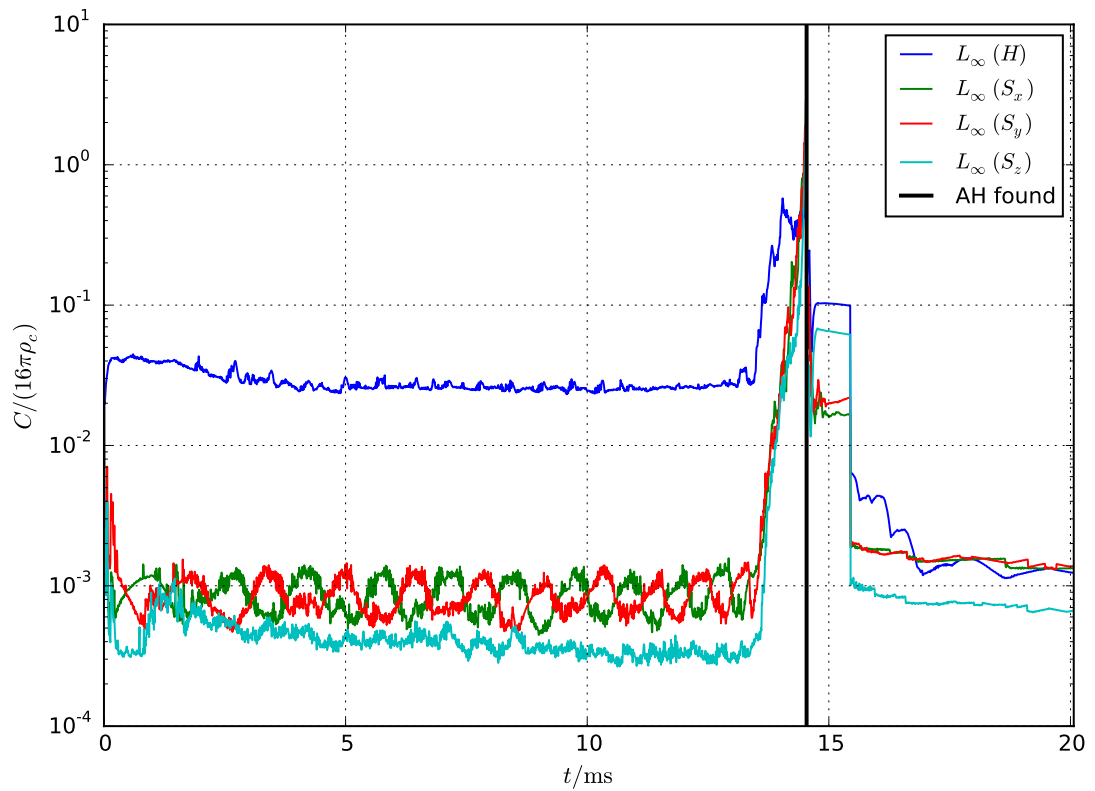


Figure 5.10 Evolution of the maximum values for the Hamiltonian constraint (blue line) and the momentum constraints (green, red, cyan lines correspond to x, y, z directions, respectively), for the magnetized high-mass model. The vertical black line marks the time of a black hole formation.

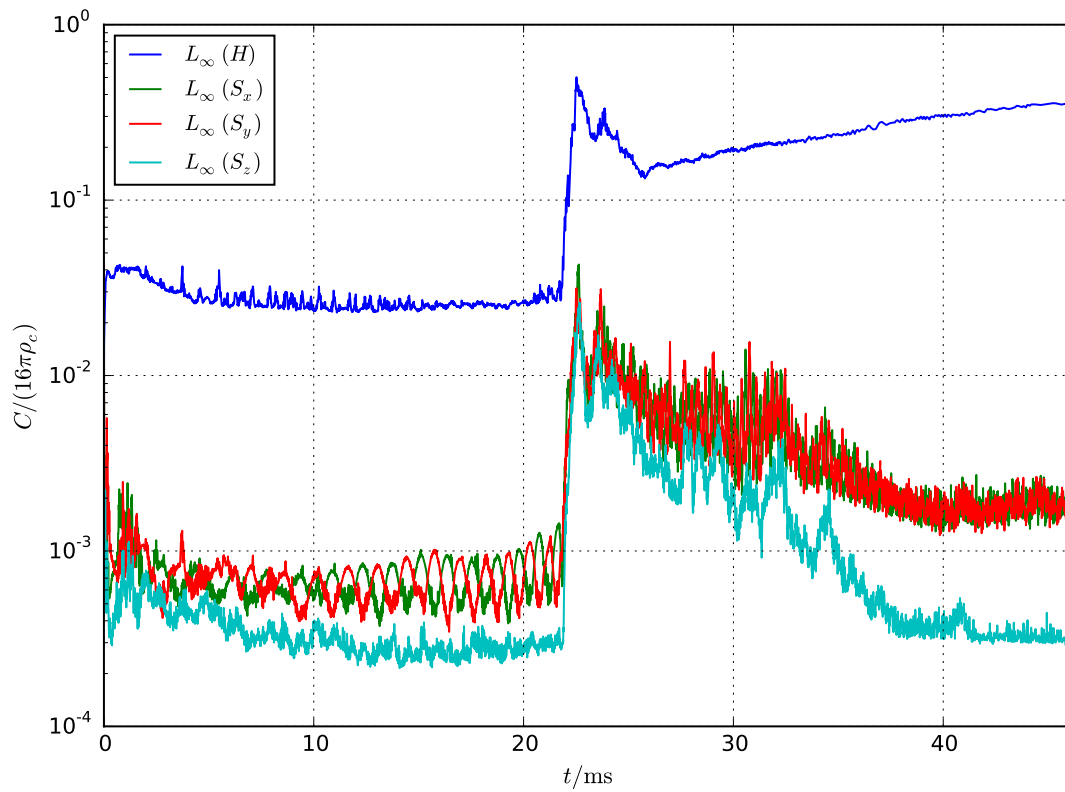


Figure 5.11 Evolution of the maximum values for the Hamiltonian constraint and the momentum constraints for the magnetized low-mass model. The relationship between line colors and physical quantities is the same as Figure 5.10.

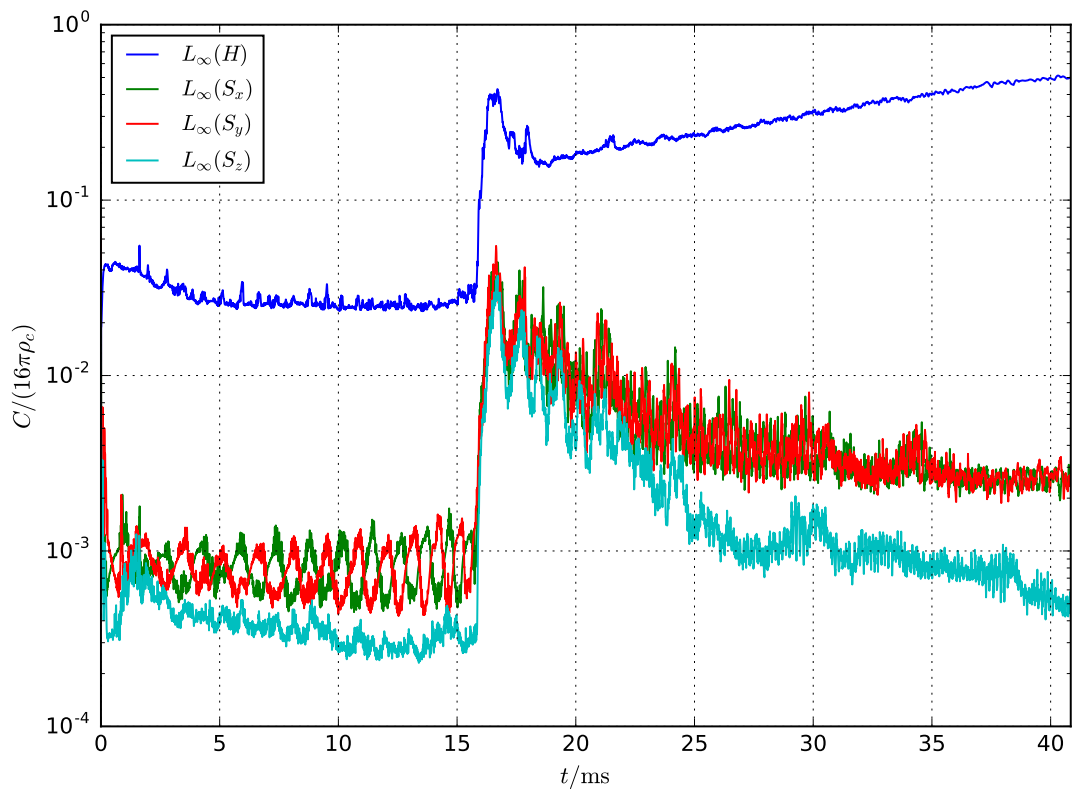


Figure 5.12 Evolution of the maximum values for the Hamiltonian constraint and the momentum constraints for the magnetized unequal-mass model. The relationship between line colors and physical quantities is the same as Figure 5.10.

Chapter 6

Binary neutron star mergers and short gamma-ray bursts: Effects of magnetic field orientation, equation of state, and mass ratio

In this chapter I present the results published in Kawamura et al 2016 [47]. The figures and part of the text presented in this chapter are taken from the published paper.

6.1 Models

We evolve magnetized, quasicircular and irrotational BNS models. The main properties of the initial data used for our simulations are listed in Table 6.1. These data are produced using the spectral-method code LORENE (<http://www.lorene.obspm.fr>), except for the setup of the magnetic field (see below). We employ the ideal-fluid EOS (denoted IF in the table) and the H4 EOS (denoted H4 [38]), along with poloidal initial magnetic fields that are confined inside the stars. The ideal-fluid EOS uses a polytropic index $\Gamma = 2$ and a polytropic constant $K = 100$ as in previous simulations [36, 72]. The H4 EOS is instead implemented as a piecewise polytropic EOS as described in Ref. [69]. In order to also take thermal effects into account in this case, we add a thermal part via an ideal-fluid EOS with a polytropic index $\Gamma = 1.8$ as done in Refs. [49, 48]. The total masses have been chosen so that the ideal-fluid and H4 equal-mass models are the same as the ones evolved in Ref. [72] and Refs. [49, 48], respectively. All our models inspiral for $\sim 3 - 6$ orbits before merger. Time of merger is defined as the time of maximum amplitude in the GW signal.

For the ideal-fluid equal-mass simulations, we use three different magnetic field orientations: both NS magnetic fields aligned to the orbital rotation axis (UU), aligned and antialigned (UD), and both antialigned (DD). For the ideal-fluid unequal-mass simulation, and also for the H4 equal- and unequal-mass simulations, we use the UU magnetic field configuration. In summary, there are six models according to EOSs, mass ratio, and magnetic field configurations: IF_q10_UU, IF_q10_UD, IF_q10_DD, IF_q08_UU, H4_q10_UU, and H4_q08_UU.

Table 6.1 Initial data parameters: mass ratio ($q = M_g^1/M_g^2$), total baryonic mass of the system (M_b^{tot}), baryonic and gravitational masses of each star at infinite separation (M_b and M_g), compactness (M_g/R_c , dimensionless), initial orbital frequency and proper separation (f_0 and d), initial magnetic energy (E_B), initial maximum value of magnetic field strength (B_{max}), and A_b , the value in geometric units used in equation 6.1 in order to fix B_{max} . See Table 5.1 for detailed description for each parameter.

Model	IF equal	IF unequal	H4 equal	H4 unequal
q	1	0.816	1	0.816
M_b^{tot} [M_\odot]	3.25	3.25	3.04	3.04
M_b [M_\odot]	1.63	1.44, 1.81	1.52	1.35, 1.69
M_g [M_\odot]	1.51	1.36, 1.67	1.40	1.26, 1.54
M_g/R_c	0.140	0.120, 0.164	0.148	0.132, 0.164
f_0 [Hz]	295	234	263	263
d [km]	59.3	68.0	61.0	61.0
E_B [10^{40} erg]	8.19	8.03	9.51	9.32
B_{max} [10^{12} G]	1.99	1.99	1.99	1.99
A_b	2.20	0.76, 5.36	1.97	1.21, 3.13

All the initial data computed with LORENE are publicly available online as supplemental material to my paper¹, except for model IF_q10 (ideal-fluid equal-mass) which is already available on the LORENE web page as model G2_I14vs14_D4R33_45km.

The magnetic fields are added a posteriori on top of the initial data produced with LORENE using the following vector potential:

$$A_\phi \equiv \varpi^2 A_b \max(p - p_{\text{cut}}, 0)^{n_s}, \quad (6.1)$$

where ϖ is the coordinate distance from the NS spin axis, $p_{\text{cut}} = 0.04 \max(p)$ is a cutoff that determines where the magnetic field goes to zero inside the NS, $\max(p)$ is the initial maximum pressure in each star, and $n_s = 2$ is the degree of differentiability of the magnetic field strength [36]. The values for A_b for each model are listed in table 6.1. For the unequal-mass models different values for A_b were used for each star in order to guarantee that they had the same initial magnetic field strength. Antialigned fields are instead obtained by multiplying A_b by -1 .

Also in this case we assume the magnetic field to be confined inside the NSs as we did in the previous chapter.

6.2 Numerical setups

In all the simulations we set the atmosphere density to $\rho_a \approx 6.2 \times 10^4 \text{g/cm}^3$. This atmosphere value is two orders of magnitude lower than that of the simulations in chapter 5. In the simulations in this chapter we want to investigate the relationship between BNS

¹<http://journals.aps.org/prd/abstract/10.1103/PhysRevD.94.064012>

Table 6.2 System properties for the different EOS and mass ratios considered in this work (Also see Table 5.2 for the description of each property): BH mass (M_{BH}), spin ($a_{\text{BH}} \equiv J_{\text{BH}}/M_{\text{BH}}^2$), and disk mass (M_{disk}) at the end of our simulations (27 – 30 ms after collapse), accretion rate computed by integrating the flux of rest-mass density across the apparent horizon (\dot{M}), accretion timescale ($\tau_{\text{acc}} \equiv M_{\text{disk}}/\dot{M}$), time of BH formation since merger (t_{BH}), instantaneous GW frequency at merger (f_{merger}) and characteristic GW frequency in the HMNS phase (f_{HMNS}). The accretion rate is taken as time average from 5 ms after collapse to the end of the simulation. The time of merger $t = 0$ corresponds to the maximum GW strain. f_{HMNS} is estimated from the characteristic peak in the post-merger spectrum (see Section 6.5).

Model	IF equal	IF unequal	H4 equal	H4 unequal
$M_{\text{BH}} [M_{\odot}]$	2.92	2.78	2.67	2.50
a_{BH}	0.81	0.77	0.71	0.63
$M_{\text{disk}} [M_{\odot}]$	0.04	0.21	0.04	0.23
$\dot{M} [M_{\odot}/\text{s}]$	0.8	2.6	1.1	1.8
$\tau_{\text{acc}} [\text{s}]$	0.05	0.08	0.03	0.13
$t_{\text{BH}} [\text{ms}]$	8.7	1.3	11.6	24.7
$f_{\text{merger}} [\text{kHz}]$	1.36	0.96	1.43	1.62
$f_{\text{HMNS}} [\text{kHz}]$	–	–	2.47	2.69

mergers and short gamma-ray bursts by studying the possible production of relativistic jets. Since the funnel that is typically formed along the BH spin-axis has a very low density, we set the atmosphere as low as possible in order to reduce possible contamination due to the interaction between the low-density funnel and the artificial atmosphere. We also used the adaptive mesh refinement driver Carpet with a total of six refinement levels. The finest grids cover each of the NSs during the inspiral and, after merger, they are merged into a larger one that covers the resulting hypermassive NS (HMNS). We adopted a resolution on the finest grids of ≈ 222 m in the runs using an ideal-fluid EOS and of ≈ 186 m in the runs using the H4 EOS. This choice has been made so that the NSs are covered by approximately the same number of points in both cases. The external boundary is located at a distance of ≈ 1400 km in the ideal-fluid case and ≈ 1200 km in the H4 case. All the simulations employed reflection symmetry across the equatorial plane to reduce computational costs.

6.3 Evolution

In this section we provide an extensive discussion of the results of our simulations, including the general dynamics, the magnetic field evolution, the dependence on the EOS and the mass ratio, a comparison with previous work, and a resolution study. The connection to SGRBs and GW emission are discussed in Secs. 6.4 and 6.5. Important quantities characterizing the system are summarized in Table 6.2 for the different cases considered in this work.

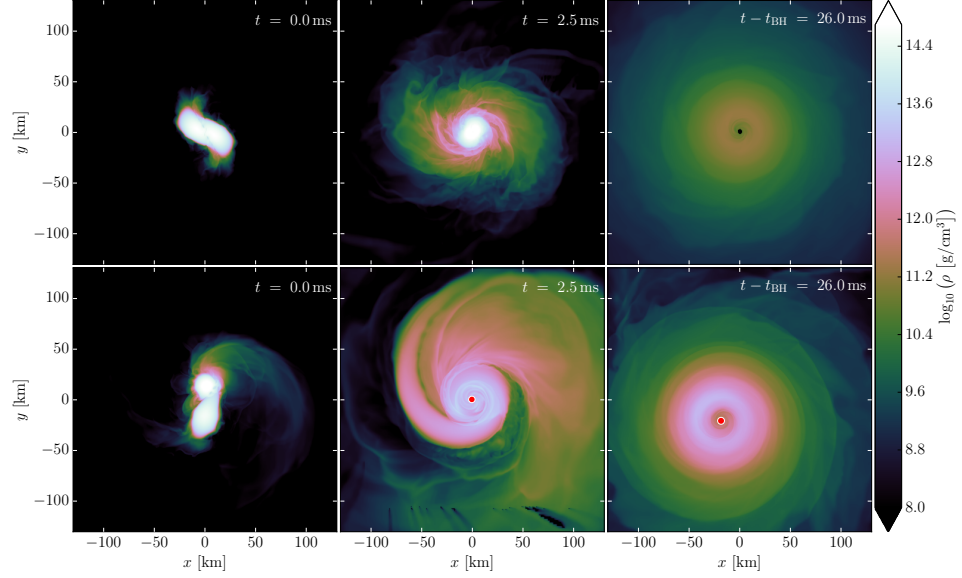


Figure 6.1 Rest-mass density evolution on the equatorial plane for models IF_q10 (top) and IF_q08 (bottom). The horizon is marked with a red circle, with the exception of the top right panel which shows the excised region (black) instead.

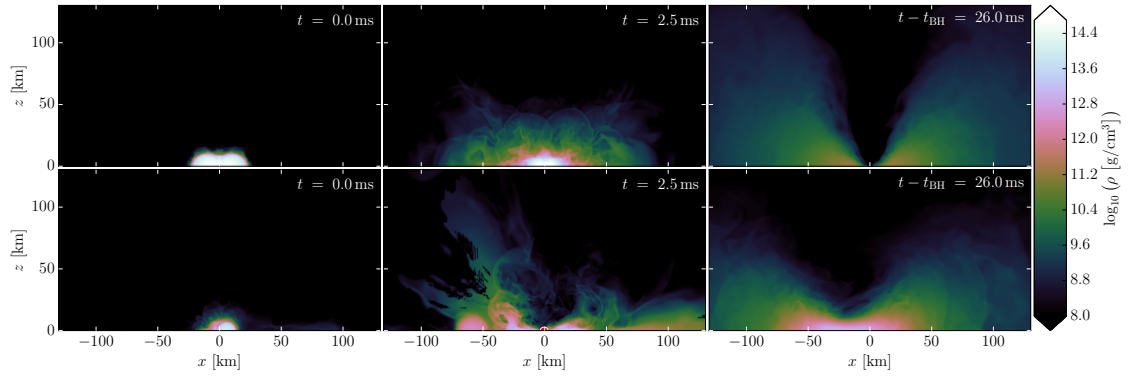


Figure 6.2 Rest-mass density evolution on the meridional plane for models IF_q10 (top) and IF_q08 (bottom). Note the lower right panel constitutes an off-center cut because of the BH drift.

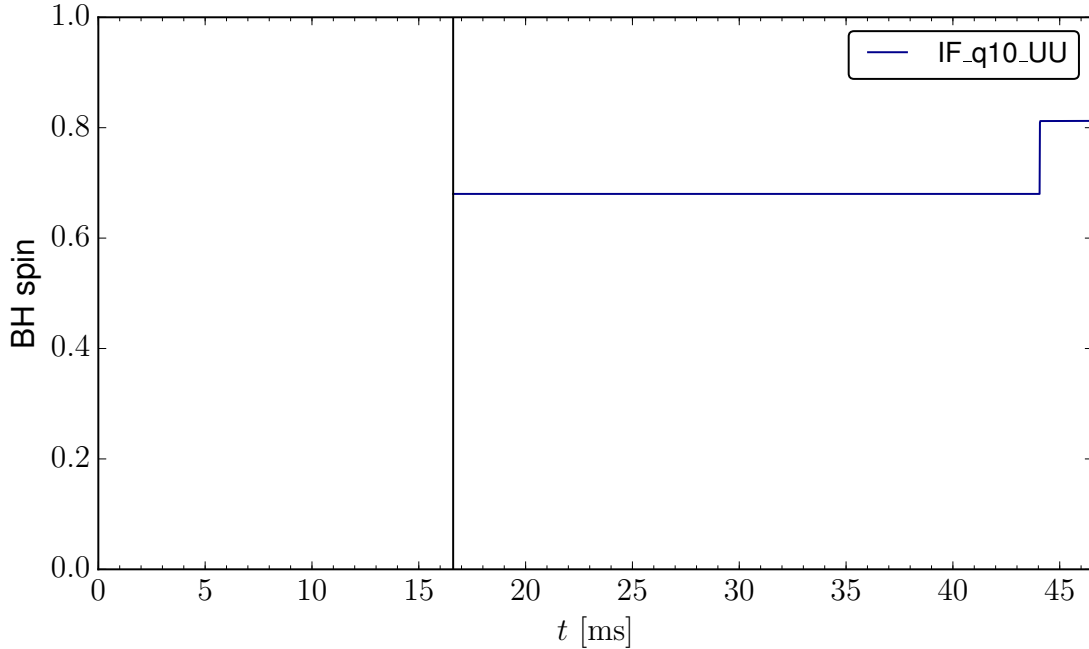


Figure 6.3 The time evolution of dimensionless BH spin a_{BH} for the IF_q10_UU model. The vertical black line denotes the time of black hole formation.

6.3.1 Ideal-Fluid Equal-Mass Model

We first consider the equal-mass case with ideal-fluid EOS and initial magnetic fields aligned with the orbital axis, IF_q10_UU. The following discussion refers to the standard resolution simulation, while different resolutions for this case are considered in Sec. 6.3.8.

The rest-mass density evolutions on the equatorial and meridional planes are shown in the top rows of Figures 6.1 and 6.2, respectively. As its total rest mass is well within the hypermassive regime for a single object, the merger is followed by a HMNS phase lasting ~ 8.5 ms and the eventual collapse to a BH. Most of the rest mass in the system is rapidly swallowed by the BH during its formation, leaving behind only a light disk. At the end of the simulation (~ 26 ms after BH formation) the disk mass is only $\sim 0.04 M_{\odot}$ and the accretion time scale is less than 100 ms (see Table 6.2). In Figure 6.3 we show the time evolution of BH spin. The discontinuity is due to the failure of finding apparent horizon during the first low value part. The final BH spin is relatively high $a_{\text{BH}} \sim 0.8$ (the highest value obtained in this study).

The evolutions of the magnetic field energy and strength are shown in Figures 6.4, 6.5, 6.6, and 6.7. A sudden increase of magnetic energy is observed in the first 2 ms after merger. This is to be attributed to the shear that is generated when the two stars first touch and that is associated with strong magnetic field amplification via the Kelvin-Helmholtz instability (although our resolution does not allow us to fully resolve it; see Section 6.3.8). In the following evolution, the magnetic field is further amplified

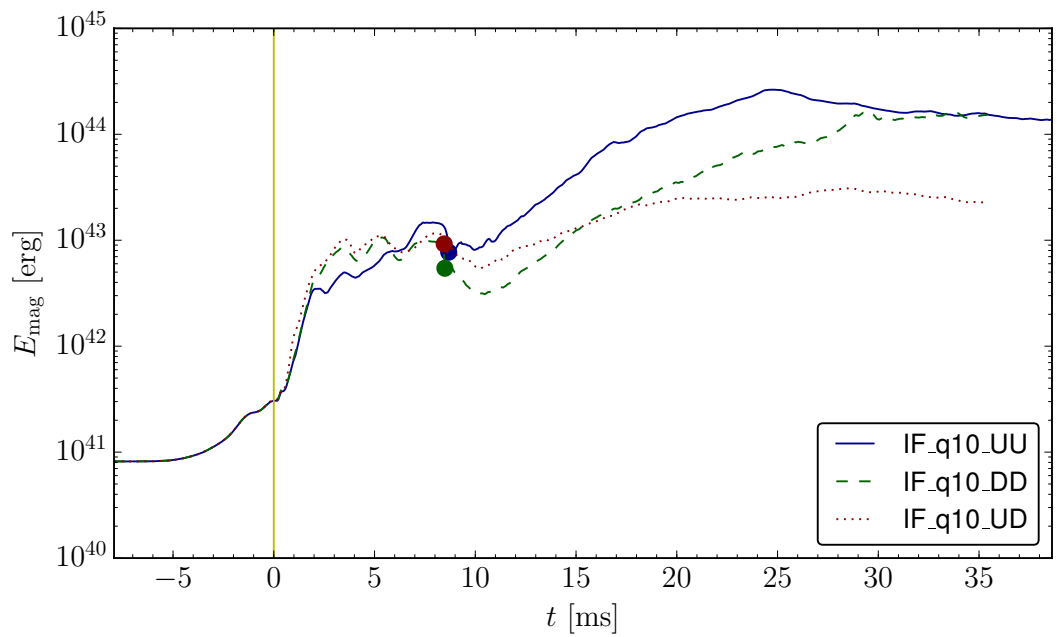


Figure 6.4 Comparison of total magnetic energy between the models IF_q10_UU, IF_q10_DD, IF_q10_UD. The yellow vertical line marks the merger time and the circles show the time of BH formation for each model.

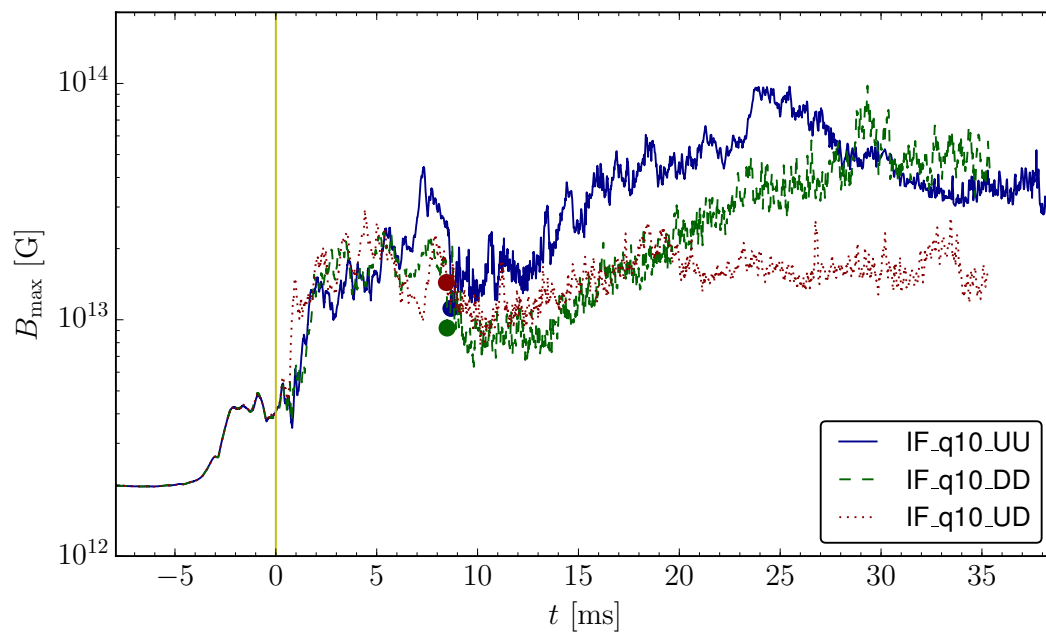


Figure 6.5 Comparison of the maximum values of magnetic field strength between the models IF_q10_UU, IF_q10_DD, IF_q10_UD. The yellow vertical line marks the merger time and the circles show the time of BH formation for each model.

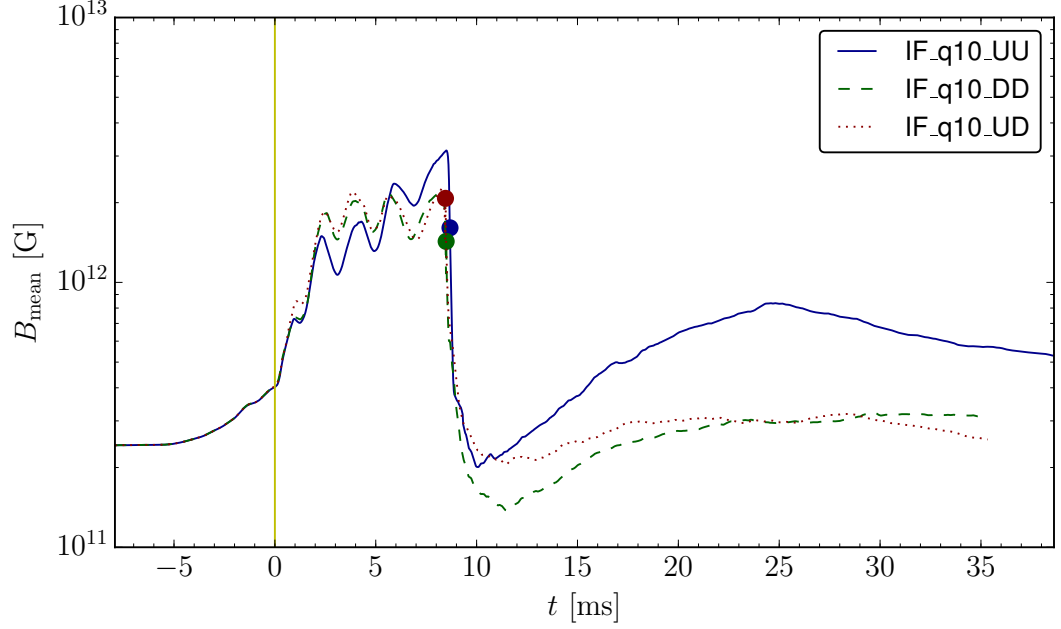


Figure 6.6 Comparison of the mean values of magnetic field strength B_{mean} between the models IF_q10_UU, IF_q10_DD, IF_q10_UD. This value is defined as $B_{\text{mean}} \equiv \int \rho B dV / \int \rho dV$, where B is the magnetic field amplitude and dV is the proper volume. The yellow vertical line marks the merger time and the circles show the time of BH formation for each model.

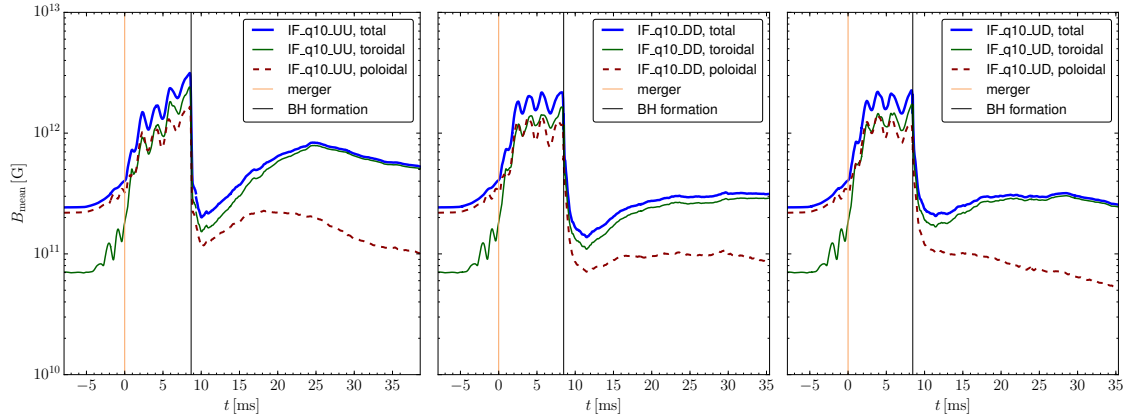


Figure 6.7 Comparison of the mean values of magnetic field strength between the models IF_q10_UU, IF_q10_DD, IF_q10_UD, including mean values of toroidal and poloidal field components. The yellow vertical lines mark the merger time and the black vertical lines mark the time of BH formation.

(at a lower rate) in the HMNS phase and in the remnant disk after BH formation. The magnetic energy and the maximum field strength do not show a sudden decrease at BH formation, indicating that most of the field is outside the high-density bulk of the HMNS that is immediately swallowed by the nascent BH. Conversely, such a drop is observed when considering a density-weighted average of the magnetic field strength (Figures 6.6 and 6.7). Around 15 ms after BH formation the gain in magnetic energy becomes lower than the loss associated with the accretion of magnetized material in the disk. Overall, the maximum magnetic field strength achieved is a factor of ~ 50 higher than the initial value. More details on the magnetic field amplification mechanisms and the dependence on resolution are discussed in Section 6.3.8.

As shown in Figure 6.7, magnetic field amplification is mostly in favor of the toroidal component. In terms of average magnetic field strength, the toroidal component becomes comparable to the poloidal one in the first ms after merger and in the HMNS phase the two keep growing together. Then, after BH formation the poloidal field remains much smaller than the toroidal one, which is more efficiently amplified in the disk.

We now discuss in more detail the geometrical structure of the magnetic field. To qualitatively assess the global structure of the field, we use three-dimensional (3D) plots of selected field lines. Visualizing field lines is a complex task and can be very misleading. We developed a prescription for the automated selection of field lines that gives good results without any manual (i.e. potentially biased) intervention. The procedure is described in detail in the Appendix A. For a quantitative description of the field, we rely instead on histograms of magnetic energy in suitable bins based on spatial position.

An overview of the evolution of the field structure is given in Fig. 6.8. During early inspiral, the field is given by the initial data prescription, Eq. (5.2). We recall that the magnetic field strength drops to zero towards the surface and there is no field outside the stars. During the last orbits of inspiral (not shown in the figure), the field already becomes more irregular. The complex fluid flows during merger finally destroy all regularity, as can be seen in the second snapshot (~ 2 ms after merger). In the remaining evolution, the field structure becomes more regular again. As expected, magnetic winding produces a toroidal field of increasing strength near the equatorial plane. More interestingly, we also observe a cone-like region of increasing strength along the edge of the accretion torus. The alignment is highlighted in the figure by displaying two isodensity surfaces in addition to the field. Initially, the field along the cone is more or less tangential, but still relatively irregular. At a later stage, around 30 ms after merger, the lines along the cone acquire a clear “twister” structure. This could be attributed to the stretching of field lines by the fluid flow along the edge of the torus.

By using an interactive version of Fig. 6.8 to look at magnified parts from different angles, we found that the strong field lines typically turn around sharply at some point and very closely follow their previous path in reverse. This is indeed the expected outcome of stretching an initially irregular field continuously along a quasistationary shearing fluid flow. We stress that Fig. 6.8 visualizes the orientation of the field, but not the sign, which alternates on small length scales. The cone contains field lines going both upwards and downwards (along the cone), and the toroidal field near the equatorial plane contains field lines wound both clockwise and counterclockwise. The field near the BH axis is only mildly

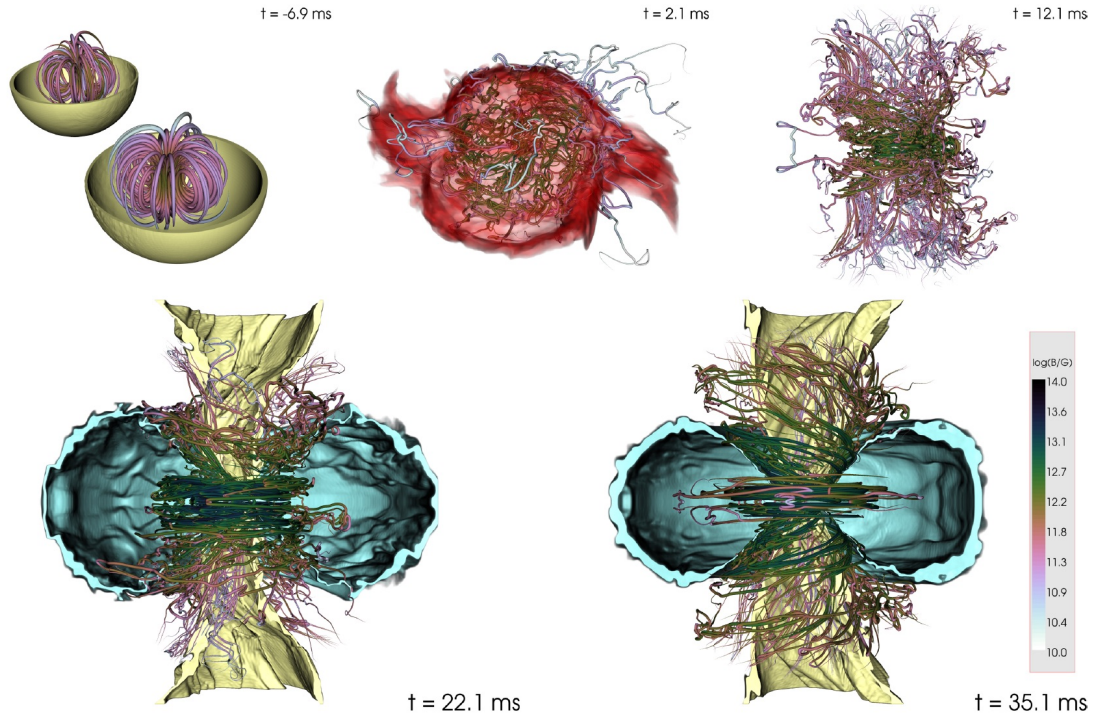


Figure 6.8 Evolution of the magnetic field structure for model IF_q10_UU. Top left: inspiral phase, showing the magnetic field, as well as the lower half of the NS surfaces. Top center: magnetic field 2 ms after merger together with the isodensity surface for $5 \times 10^{12} g/cm^3$, drawn as a semitransparent red surface. Top right: magnetic field structure 12 ms after merger. Bottom left: magnetic field 22 ms after merger, together with two isosurfaces of density 10^8 (yellow) and $10^{10} g/cm^3$ (cyan), cut off for $y < 0$. Bottom right: same at 35 ms after merger. The color of the field lines gives a rough indication of the field strength (see colorbar), but for quantitative results compare figures 6.9, 6.11, and 6.17.

collimated. From animations showing a cut through the meridional plane, we found that it is also strongly fluctuating. This seems to be related to lumps of low-density matter falling towards the BH along the axis.

To quantify the magnitude and topology of the magnetic field, we sum the magnetic field energy contained in bins regularly spaced in $\cos(\theta)$, where θ is the angle to the BH axis. Thus, a homogeneous field would result in a flat distribution. This measure allows us to distinguish the amount of energy in the disk, along the conical structure separating the disk and funnel, and near the axis. As a measure for the strength of the field, we computed for each bin the field strength B_{90} , defined by the requirement that 90% of the magnetic field energy is contributed by regions with field strength below B_{90} . We use this measure because using the maximum field strength is too sensitive to potential outliers, while using the average field strength would depend on the volume under consideration. Using B_{90} is a good compromise.

The energy distribution and the field strength B_{90} for model IF_q10_UU at three

different times are shown in Fig. 6.9. The total magnetic energy near the equatorial plane increases by around an order of magnitude between 12–22 ms after merger, most likely because of magnetic winding in the torus. The energy 35 ms after merger is slightly lower, however. The reason is uncertain, but it might be a change of the torus structure and/or loss by accretion. Since there is no ejecta for this model, ejecta carrying the magnetic energy is unlikely to be the reason. The energy along the conical structure separating the disk and funnel is steadily growing (side peaks). The final distribution has a pronounced local maximum, corresponding to an opening half-angle around 50° . Notably, the regions near the BH axis ($\theta < 20^\circ$) do not contribute significantly to the total field energy.

The field strength B_{90} near the equator increases from $\approx 6 \times 10^{12}G$ at 12 ms after merger up to $\approx 2 \times 10^{13}G$ at 22 ms after merger, and afterwards it stagnates. B_{90} is of the same order of magnitude at all angles from the equator up to the conical structure, and then it drops rapidly in the funnel. In particular, near the axis the field is very weak (less than $3 \times 10^{11}G$ at 12 ms after merger) and further drops by a factor of ≈ 2 at the end of the simulation.

6.3.2 Comparison with Rezzolla et al. 2011

As mentioned before, the specific choice of EOSs used in this work has been made in order to favor comparisons with previous work. In particular, our equal-mass model employing the simplistic ideal-fluid EOS is the same as the one studied in [72], the first work to claim the formation of a funnel-like structure in the magnetic field after BH formation, a region of low-density matter where a jet eventually producing a GRB may be launched.

In order to make a meaningful comparison between the present work and Ref. [72], we first describe the differences in the numerical methodology of the simulations. However, we did not investigate the influence of different parameters one by one because it would have been too expensive. Below we report what we believe are the relevant changes.

First of all, in both works the vector potential is the evolved variable for the magnetic field, in order to guarantee the divergence-free character of the magnetic field. However, differently from Ref. [72], we use the modified Lorenz gauge [30, 31]. This avoids spurious amplifications of the magnetic field at the boundary between refinement levels, as was observed in the simulations of Ref. [72].

The resolution of the simulation in Ref. [72] is the same as our standard resolution, as is the number of refinement levels. In the current work, we evolved the same model also with higher and lower resolutions, as discussed in Sec. 6.3.8. The location of the outer boundary and the size of the refinement levels are different from Ref. [72]. The finest refinement level after merger in this work only extends to $30km$, compared to $44km$ used in Ref. [72]. The outer boundary on the other hand was expanded to $1403km$, almost 4 times the extent used in Ref. [72]. We believe that this was an important improvement on the previous work. The simulation described in Ref. [72] had to be terminated when large spurious waves in the magnetic field coming from the outer boundary had contaminated the solution even near the central object, while we encountered no such problems.

Another difference concerns the symmetries. In both works, a reflection symmetry with respect to the orbital plane was used, but in contrast to Ref. [72], we do not enforce π symmetry around the z axis, thus allowing for non- π -symmetric modes to develop. However,

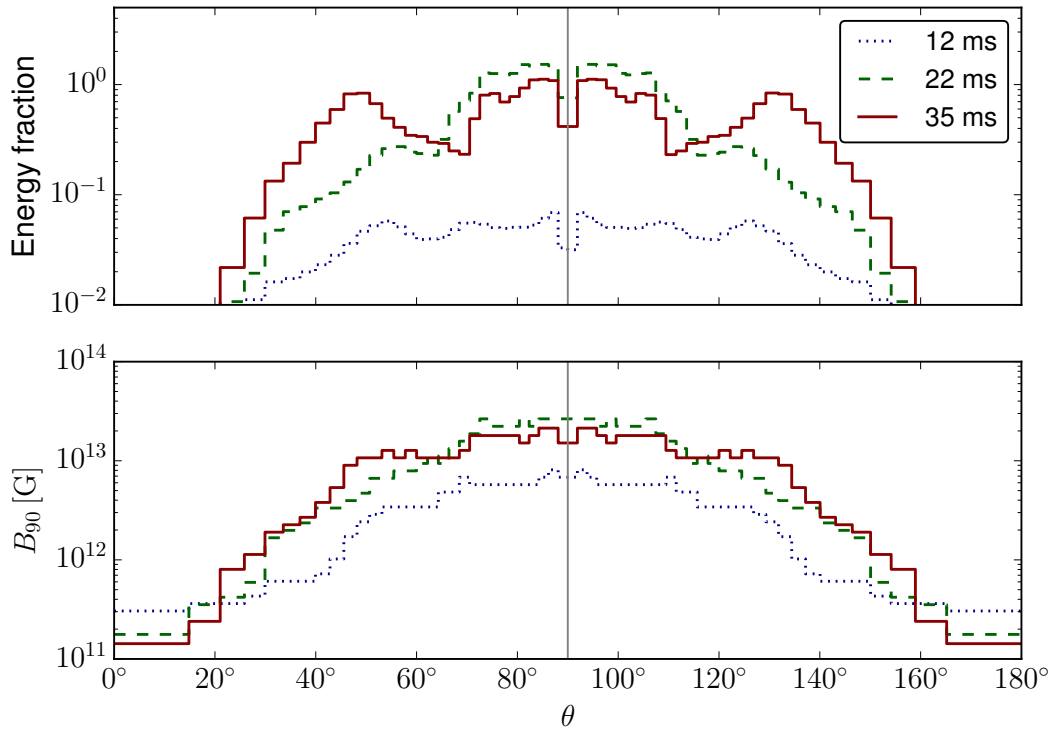


Figure 6.9 Distribution of the magnetic field with respect to the θ -coordinate, for model IF_q10_UU at various times after merger. Top: histogram of magnetic energy employing bins regularly spaced in $\cos(\theta)$, where $\theta = 0$ is the z-axis and $\theta = 90^\circ$ the equator. The plot is normalized to the total magnetic energy 35 ms after merger. Bottom: field strength B_{90} defined as the value for which 90% of the magnetic energy (inside a given $\cos(\theta)$ bin) is contained in regions with field strength below B_{90} .

in the case of equal-mass binaries the system becomes roughly axisymmetric soon after the merger and therefore we do not think that the different symmetries imposed led to significant differences in the results.

Another improvement is the lower density of the artificial atmosphere in our work, $\sim 6.2 \times 10^4 g/cm^3$, which is 3 orders of magnitude smaller than the one used in Ref. [72]. This could be relevant for the computation of the accretion rate, estimated in Ref. [72] from the time derivative of the total amount of matter outside the apparent horizon, and which might contain a significant error due to the effect of the artificial atmosphere. We measure the accretion rate from the integrated matter flux through the apparent horizon instead.

We now compare the outcome of Ref. [72] to our standard resolution run of the same model. The most important improvement is our detailed analysis of the magnetic field near the BH spin axis. In Ref. [72], a magnetic field of $8 \times 10^{14} G$ near the axis² was reported. In this work, we found a much weaker field near the axis. In fact, we computed the full magnetic field energy spectrum as a function of the angle to the spin axis, and found that 90% of the field energy near the axis (cf. Fig. 6.9) is contributed by field strengths below $2 \times 10^{11} G$, and that the spectrum does not extend beyond $10^{12} G$.

Further, we find only a weakly collimated and fluctuating field in this region. We could not reproduce the strong collimation suggested by the field line visualization of Fig. 3 in Ref. [72], which shows field lines originating on the apparent horizon and tracing the shape of the funnel, proceeding outwards nearly as straight lines. One could argue that this is merely a difference in visualization methods, given that the seeds of this plot were selected ad hoc, while we adopted a more systematic approach for the selection of field lines. However, we do not fully rely on such visualizations and also used two-dimensional (2D) cuts in the meridional plane, both as snapshots and animations, to cross-check our results. What we find instead is a twister-like configuration of the magnetic field, with an opening half-angle around 50° and a field strength around $10^{13} G$.

Comparing the evolution of the maximum field strength, i.e., Fig. 6.5 with the right panel of Fig. 2 in Ref. [72], we find a slightly stronger amplification between merger and collapse. The main difference however is the post-collapse amplification. The maximum field strength in Ref. [72] keeps growing up to $10^{15} G$, while for our simulation it settles around $10^{14} G$. Also, our simulation is a bit longer and exhibits a decrease of the maximum field strength starting $24ms$ after merger. These differences may be due to the different numerical setups of the two simulations, in particular the location of the outer boundary, but we cannot provide certain conclusions.

We stress that the maximum is not a very reliable measure for the growth of the magnetic field, since it is sensitive to outliers, either physical or caused by numerical errors. Inspecting measures not relying on a single point is more meaningful. In particular, the measure B_{90} is a more robust replacement for the maximum. Furthermore, using the density-weighted mean allowed us to quantify the field of the HMNS (see Fig. 6.6). More specifically, the use of histograms of magnetic energy with respect to the θ coordinate allowed us to quantify the spatial distribution of the post-collapse field in more detail (see

²However, L.B. and B.G. (who are also co-authors of Ref. [72]) found this to be an erroneous statement. The number quoted in [72] referred to the *global* maximum of the poloidal field component (see also figure 2 of [72]).

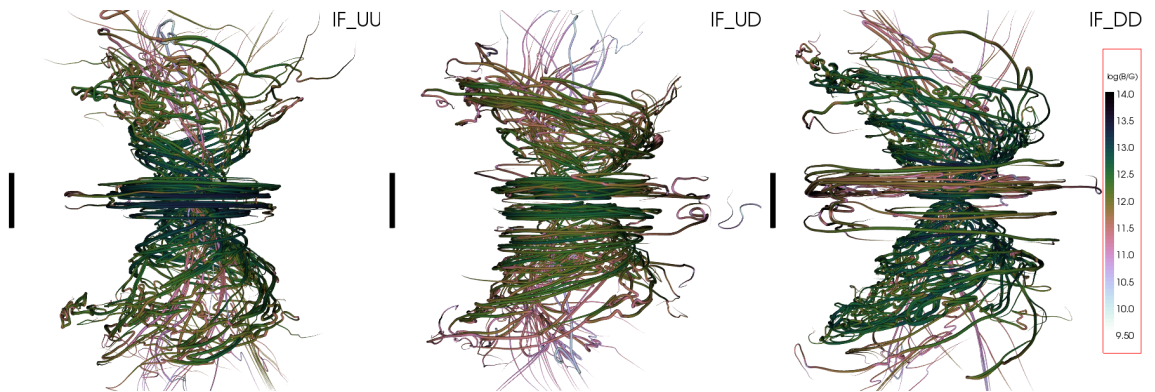


Figure 6.10 Magnetic field structure 35ms after the merger, comparing models IF_q10_UU, IF_q10_UD, and IF_q10_DD. The black bars provide a length scale of 20km. The coloring of the fieldlines indicates the magnetic field strength ($\log_{10}(B [G])$, same colorscale for all models) along the lines. However, for quantitative results see Fig. 6.11.

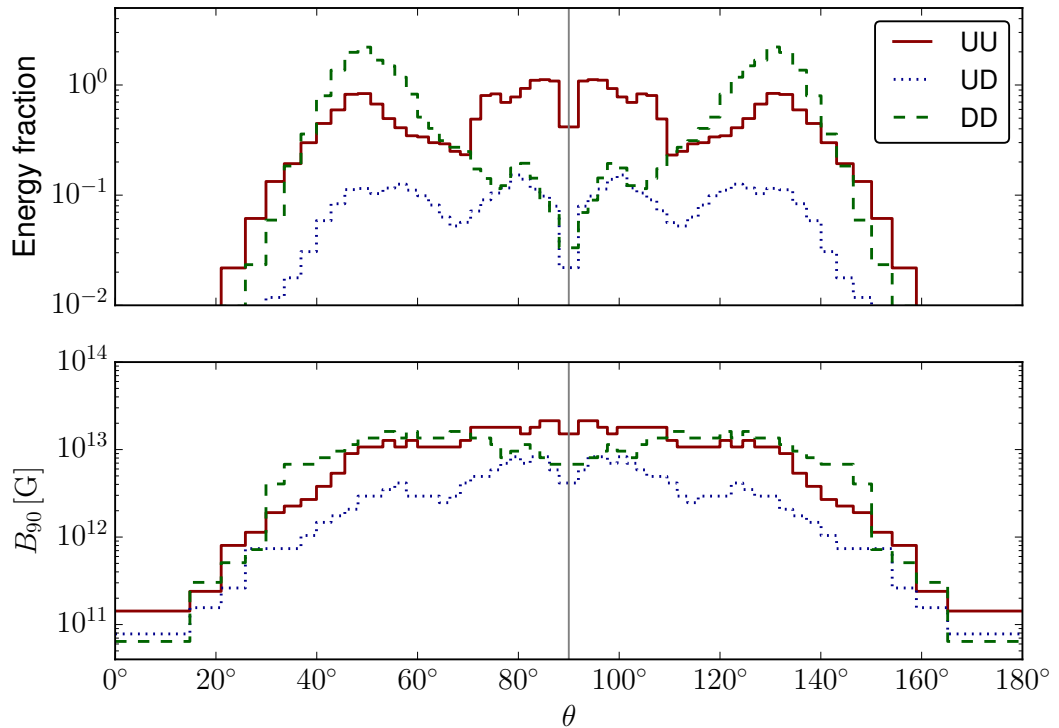


Figure 6.11 Like Fig. 6.9, but comparing models IF_q10_UU, IF_q10_UD, and IF_q10_DD 35ms after the merger. The energy distribution (top panel) is normalized to the total energy for model IF_q10_UU.

Fig. 6.9). As in Ref. [72], we find a clearly toroidal field structure in the disk, although the maximum strength is more than 1 order of magnitude lower than the value $2 \times 10^{15} G$ reported in Ref. [72]. Further, the measure B_{90} is around 2 orders of magnitude lower.

Note that a comparison between our Fig. 6.4 and the left panel of Fig. 2 of [72] is not possible because they show different quantities: the former shows the total magnetic energy as integrated over the whole domain, while the latter shows the emitted magnetic energy computed by integrating the Poynting vector. We did not compute the latter in our simulation.

The mass and spin we found for the BH formed during merger agree better than 1% with Ref. [72]. Also the initial disk mass is comparable. We did however find an accretion rate around 4 times larger than the one reported in Ref. [72]. We believe our result is more robust since we use the flux instead of the total rest mass outside the horizon, which in fact starts *increasing* at some point for the data on which Ref. [72] is based.

Both Ref. [72] and the present work do not find any outflows in the funnel along the rotation axis of the BH. This might be due to missing physical input (neutrino treatment; limits of the MHD approximation) in the simulations and/or too low resolution. We have checked that the matter in the funnel is not magnetically dominated in our simulation, which makes outflows unlikely. We note that the simulations presented in Refs. [76, 67] featured mildly relativistic outflows. This is due to the use of stronger initial magnetic fields that allow to better resolve the magnetorotational instability (MRI), and much longer evolutions after BH formation. Finally, Ref. [72] reported some outflows along the edge of the funnel. However, the given limit $\Gamma \lesssim 4$ for the Lorentz factor of the outflows was based on the *global* maximum. Using a movie showing a cut of v^z in the x-z plane ($z > 0$), we find a much lower limit of $v^z < 0.3c$ for any upward movement of matter in the disk or its edge.

6.3.3 Effects of the Initial Magnetic Field Orientation

When considering a different orientation for the initial magnetic field in the two NSs, we observe almost no differences in the overall dynamics, as well as the final BH mass and spin, the time of BH formation, the mass in the disk and the accretion rate. Nevertheless, some differences can be observed in the magnetic field evolution. From the magnetic energy and the maximum field strength (Fig. 6.4 and 6.5) we see that the totally aligned (with respect to the orbital axis) or totally misaligned cases, UU and DD respectively, reach the same level of magnetic field amplification at the end of the simulation (although with a slightly different path). The case in which magnetic fields are aligned in one NS and antialigned in the other (UD) is instead disfavoured because of a less efficient amplification in the disk, after BH formation. This may be due to the fact that in this case the magnetic field lines, in the region where the two NSs enter in contact with each other, have opposite directions and this may lead to a reduction in the magnetic field amplification. From the density-weighted average of the magnetic field strength (cf. Fig. 6.6), we notice a stronger magnetic field amplification in the inner (highest-density) region of the accretion disk for the UU case, compared to the DD and UD cases.

The influence of the initial alignment on the final structure of the field is shown in Fig. 6.10. All models exhibit the same general features, namely a toroidal field near the

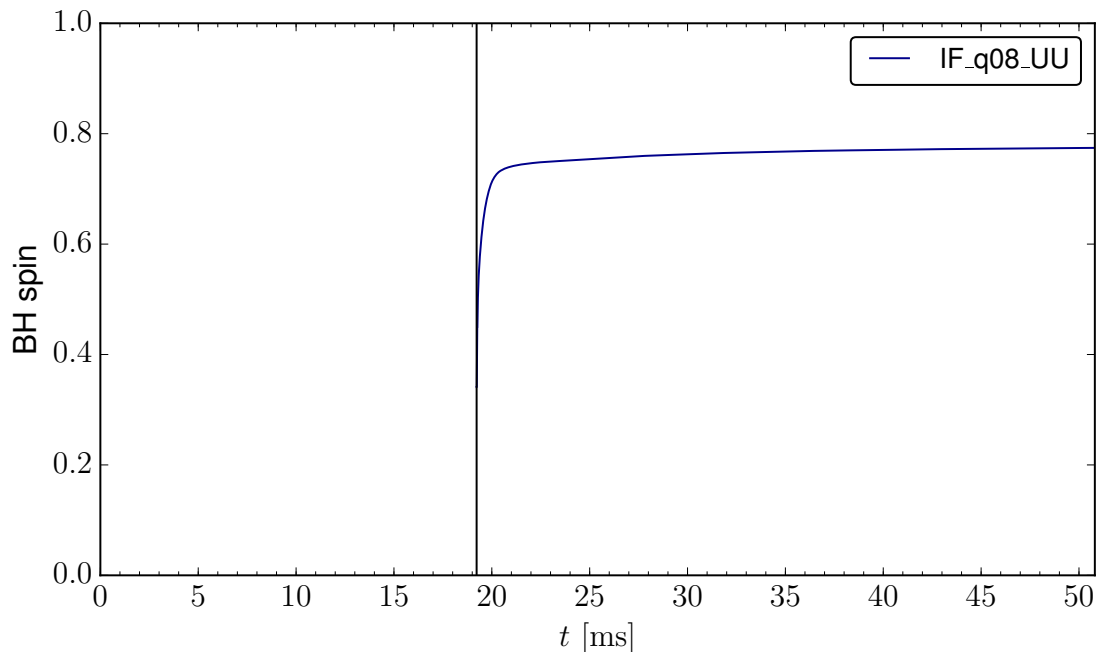


Figure 6.12 The time evolution of dimensionless BH spin a_{BH} for the IF_q08_UU model. The vertical black line denotes the time of black hole formation.

equatorial plane, a twister-shaped field forming a conical structure, and a very weak field near the axis. The relative strength between the cone and equatorial parts seems strongly affected by the initial alignment. This impression is validated by Fig. 6.11, which shows the distribution of the magnetic energy and the field strength B_{90} introduced in Sec. 6.3.1. The UU configuration contains more energy near the equatorial plane than both the UD and DD configurations, which are comparable in that respect. The amount of energy in the cone, on the other hand, is largest for the DD case and smallest for the UD case. The latter also has the weakest field strength B_{90} .

6.3.4 Ideal-Fluid Unequal-Mass Model

In order to investigate the effect of the mass ratio on the dynamics of matter and magnetic fields, we also evolved a model with a mass ratio of ~ 0.8 (model IF_q08).

The bottom rows of Figures 6.1 and 6.2 show the evolution of the rest-mass density on the equatorial and meridional planes, respectively.³ In this case the evolution is strongly asymmetric with the less compact star being strongly deformed and disrupted during merger. Even if this model has the same total baryonic mass as the equal-mass case, it

³In the central lower panel of both Figures 6.1 and 6.2 one can notice some artificial effects on the boundary between refinement levels, caused by failures in the conservative-to-primitive routine that sets those grid points to atmosphere. These effects, however, are present only in this case and they have negligible effect on the results discussed in this work, since they happen in low density regions.

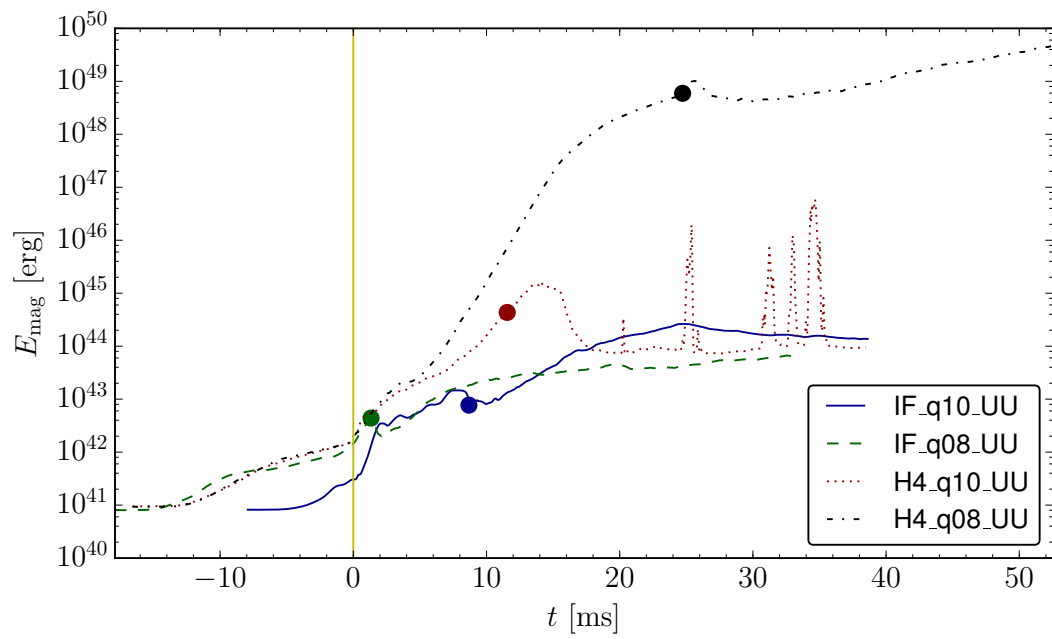


Figure 6.13 Comparison of total magnetic energy between models IF_q10_UU, IF_q08_UU, H4_q10_UU, H4_q08_UU. The yellow vertical line marks the merger time and the circles show the time of BH formation for each model.

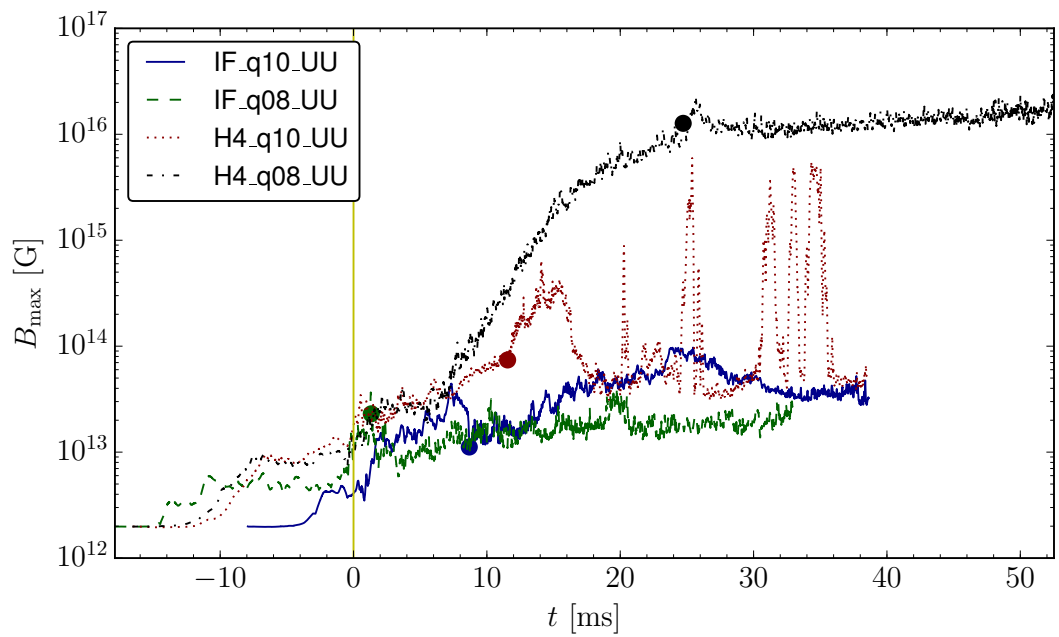


Figure 6.14 Comparison of the maximum values of magnetic field strength between models IF_q10_UU, IF_q08_UU, H4_q10_UU, H4_q08_UU. The yellow vertical line marks the merger time and the circles show the time of BH formation for each model.

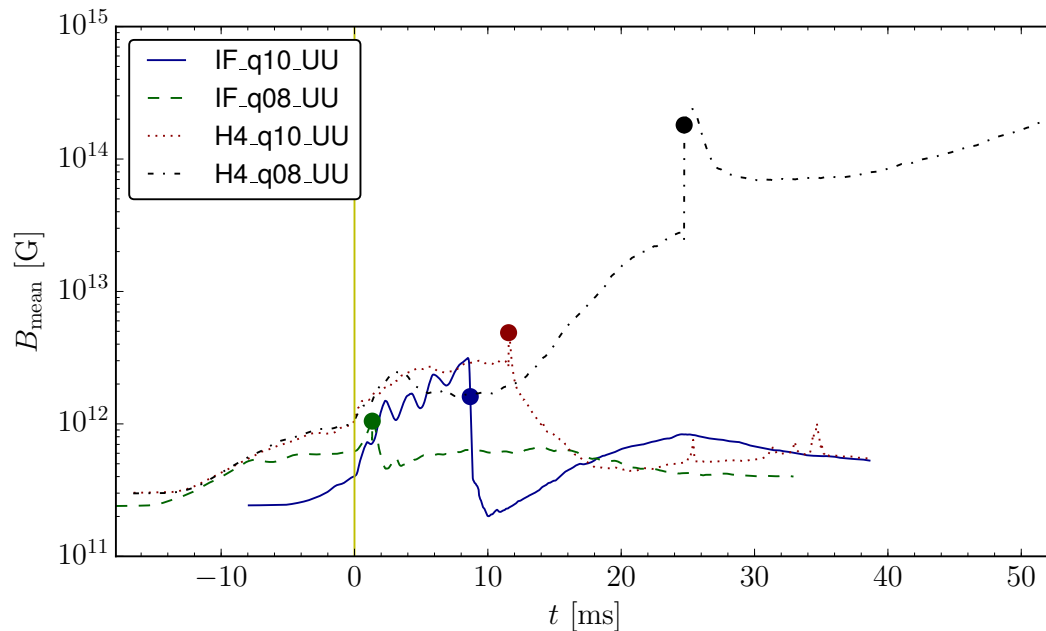


Figure 6.15 Comparison of the mean values of magnetic field strength between models IF_q10_UU, IF_q08_UU, H4_q10_UU, H4_q08_UU. The yellow vertical line marks the merger time and the circles show the time of BH formation for each model.

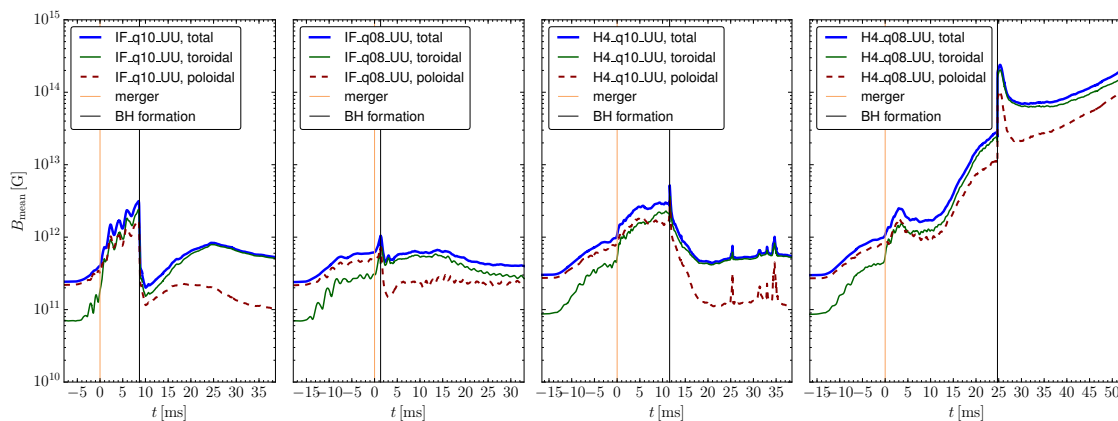


Figure 6.16 Comparison of the mean values of the total, poloidal, and toroidal magnetic field strengths between models IF_q10_UU, IF_q08_UU, H4_q10_UU, H4_q08_UU. The yellow vertical lines mark the merger time and the black vertical lines mark the time of BH formation.

promptly forms a BH after merger and therefore does not produce a HMNS. It is already evident from Figure 6.1 that the disk formed after merger has higher densities and it is more extended. As expected it is indeed more massive than the one formed in the equal-mass case and it has a rest mass of $\sim 0.21M_{\odot}$ at the end of the simulation. The accretion rate is more than 3 times larger than in the equal-mass case, while the BH has a smaller mass and spin (see Figure 6.12 for the time evolution of BH spin and Table 6.2), due to the larger amount of mass still in the disk by the end of the simulation.

The evolution of the magnetic field strength is shown in Figures 6.13, 6.14, 6.15, and 6.16. Because of the lack of a HMNS phase, the magnetic field is not amplified to the same maximum strengths as the equal-mass model prior to collapse, but, also because of the fact that more mass is left outside the BH, the density-weighted mean value after BH formation is similar to the equal-mass model (compare the first and second panels of Figure 6.16).

The influence of the mass ratio on the structure of the magnetic field is shown in Figures 6.17 and 6.18. For the ideal-fluid models, we find that the magnetic energy near the equatorial plane is reduced by an order of magnitude for the unequal-mass case. The energy and field strength B_{90} in the conical structure are comparable, but the opening half-angle is $\approx 10^{\circ}$ larger for the unequal-mass case. Note that we find much larger differences for the H4 EOS, as will be discussed in Sec. 6.3.7.

6.3.5 Equal-Mass H4 Model

We now investigate the effect of a different EOS using the piecewise approximation of the H4 EOS. We begin by describing our equal-mass model, which we recall is also the same one evolved in Refs. [49, 48].

The top panels of figures 6.19 and 6.20 show the evolution of the rest-mass density on the equatorial and meridional planes, respectively. Like in the case of the ideal-fluid equal-mass model IF_q10_UU, the merger remnant goes through a HMNS phase lasting about 12 ms before collapsing to a spinning BH. The disk mass is approximately the same as in model IF_q10_UU, but the BH mass is slightly smaller, consistent with the lower initial mass for the H4 models. Figure 6.21 is the time evolution of BH spin (the discontinuity at ~ 51 ms is due to the failure of finding apparent horizon between ~ 36 and ~ 51 ms and during that interval the value of the spin is kept constant in the plot), the value is also smaller than that in the IF_q10_UU model (see Table 6.2).

The comparison of the magnetic field evolution between the H4 and the ideal-fluid equal-mass models is shown in Figures 6.13, 6.14, 6.15, and 6.16. Since the lifetime of the HMNS is slightly longer than that of the ideal-fluid equal-mass model, the amplification of the magnetic energy and the maximum field strength are larger than in the ideal-fluid equal-mass model during the HMNS phase. After BH formation the magnetic field in the disk has a strength comparable to the one for the ideal-fluid equal-mass model, even if it exhibits a smaller decrease at BH formation. This may also be correlated with the slightly higher densities in the disk (compare the rightmost top panels of Figures 6.19 and 6.1).

In Figure 6.13 one can also notice some spikes in the evolution of the magnetic energy. These are due to very brief amplifications of the magnetic field near the surface of the apparent horizon in matter infalling into the BH and are very rapidly accreted by the

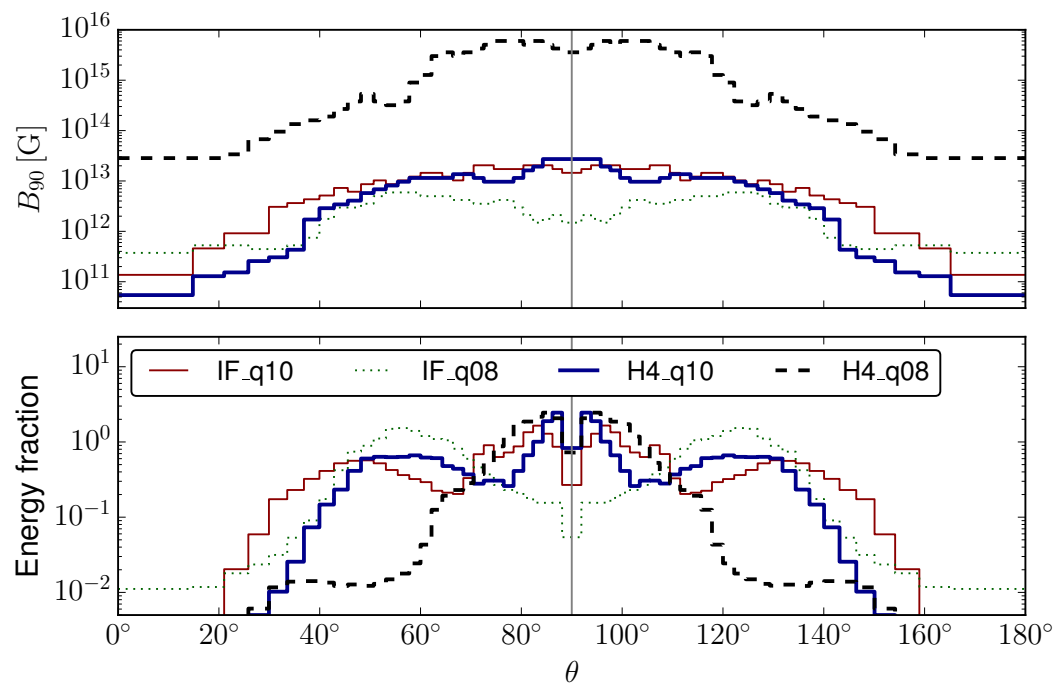


Figure 6.17 Like Fig. 6.9, but comparing models IF_q10_UU, IF_q08, H4_q10, and H4_q08 around $32ms$ after the merger. Also, each model is normalized separately in the lower panel, and we employed coordinates where the BH is located at the origin to account for the BH drift exhibited by the unequal mass models.

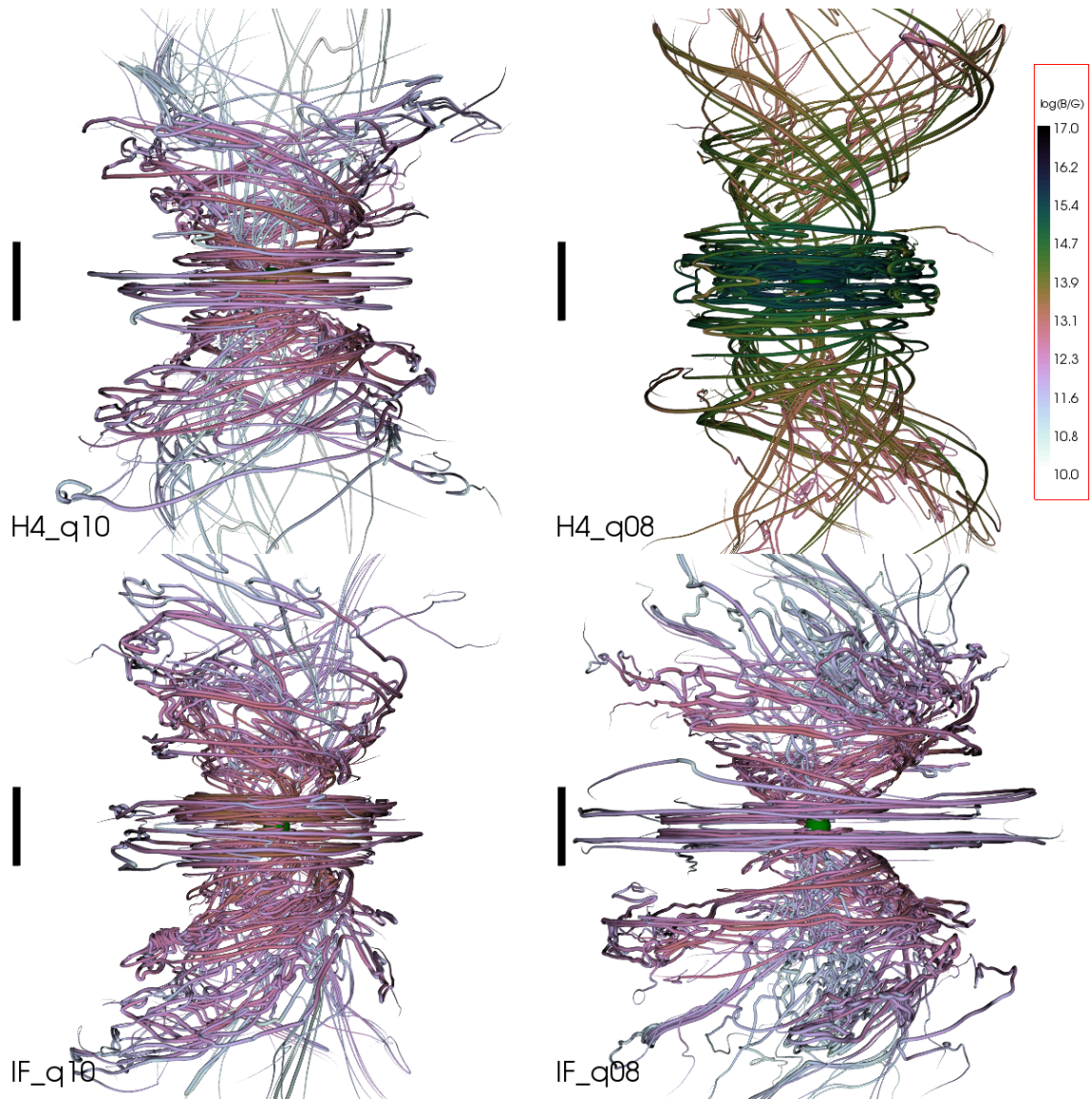


Figure 6.18 Magnetic field structure around 32ms after the merger, comparing models IF_q10_UU, IF_q08, H4_q10, and H4_q08. The black bars provide a length scale of 20km. The coloring of the field lines indicates the magnetic field strength ($\log_{10}(B [G])$, same color scale for all models) along the lines. However, for quantitative results see Fig. 6.17.

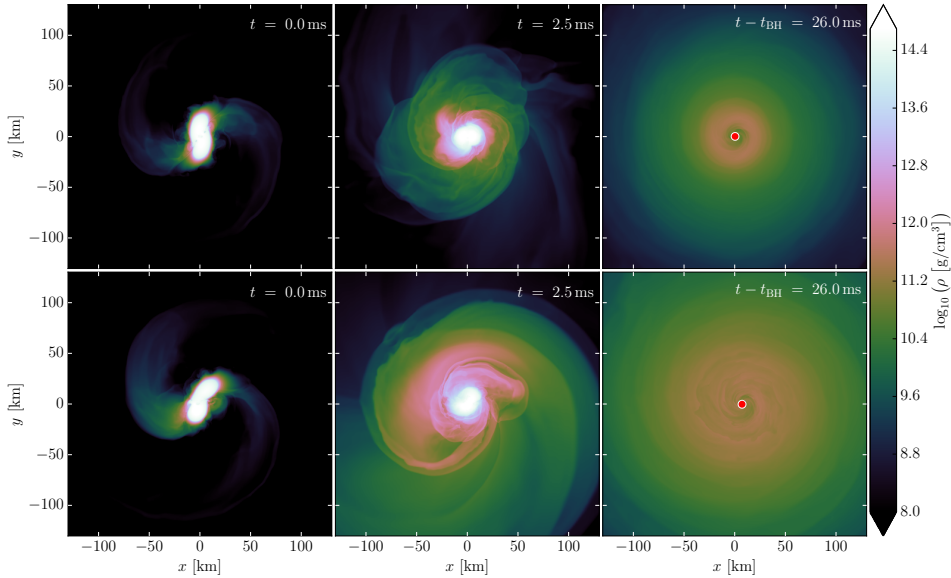


Figure 6.19 Rest-mass density evolution on the equatorial plane for models H4_q10 (top) and H4_q08 (bottom).

BH.

A comparison of the magnetic field structure for models H4_q10 and IF_q10 is given in Figures 6.17 and 6.18. Note however that the masses of the stars are also different, not just the EOS. The main difference is the opening half-angle of the conical part of the field, which is $\approx 10^\circ$ larger for the H4 equal-mass case. The magnetic energy and field strength B_{90} are instead very similar (see Figure 6.17).

6.3.6 Comparison with Kiuchi et al 2014

Our equal-mass H4 EOS model allows for a direct comparison with the results of Refs. [49, 48], who studied magnetized binaries with the highest grid resolution to date. For this, they employed a fixed mesh-refinement code described in Refs. [51, 50]. The implementation of their fixed mesh refinement (except for the part dealing with the magnetic field) is based on that of the SACRA code [85], which had been quantitatively compared to the *Whisky* code [11, 12] several years ago in Refs. [10, 68]. The main difference between *Whisky* and the latest code of Refs. [49, 48] is the scheme used to enforce the divergence-free constraint for the magnetic field. Differently from *Whisky*, the code of Refs. [49, 48] employs a fourth-order-accurate-in-time flux-CT scheme [13], which ensures also the magnetic-flux conservation across refinement boundaries, in addition to the divergence-free condition. Another difference is that the artificial atmosphere density is only constant up to some fixed radius and then falls off like r^{-2} [50]. This is important for ejected matter and magnetically driven winds, but probably irrelevant for the results discussed here.

The most important difference to the simulations presented in Ref. [49] is the grid resolution. The finest grid spacing used in Ref. [49] is $70m$, which is 2.66 times better than

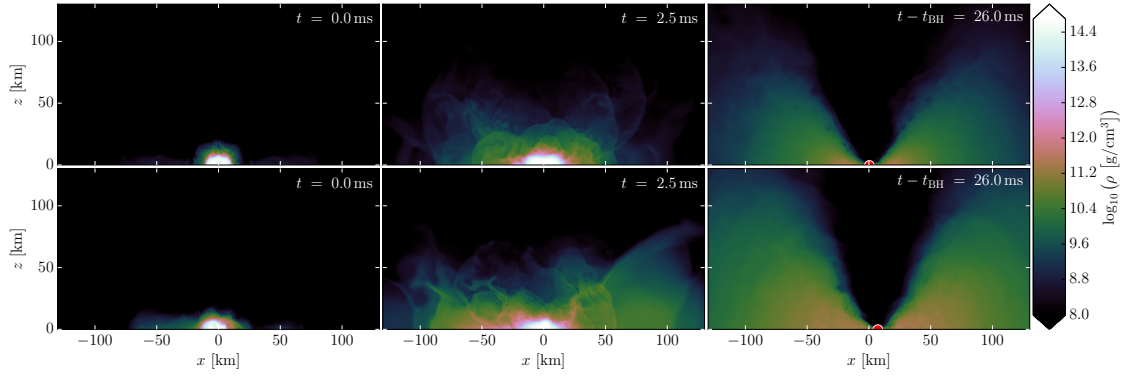


Figure 6.20 Rest-mass density evolution on the meridional plane for models H4_q10 (top) and H4_q08 (bottom).

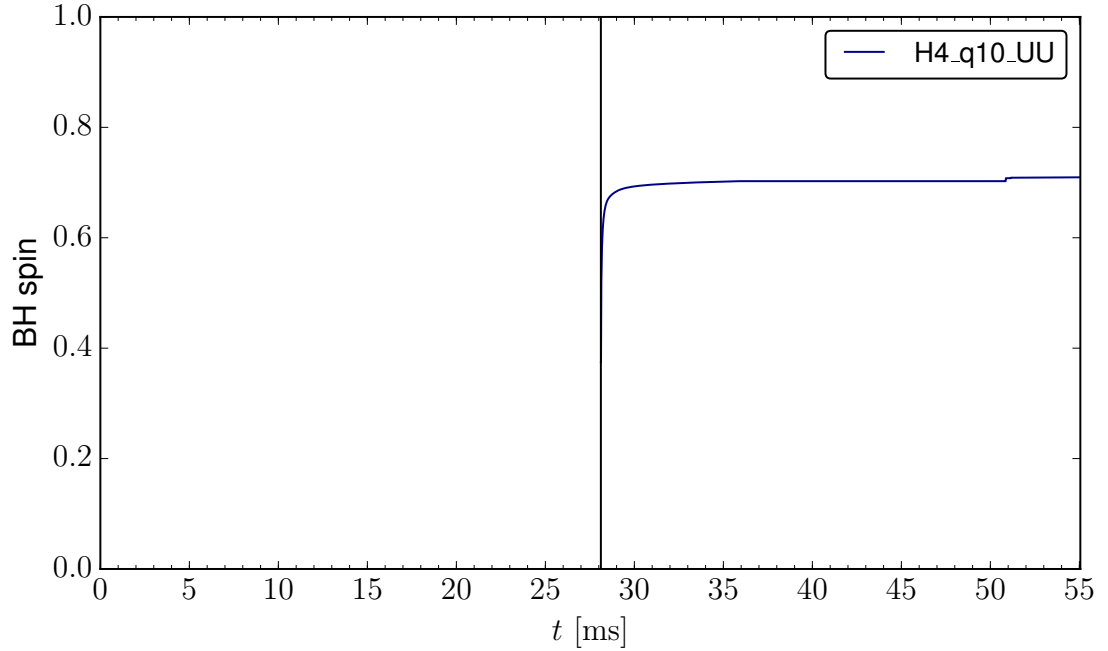


Figure 6.21 The time evolution of dimensionless BH spin a_{BH} for the H4_q10_UU model. The vertical black line denotes the time of black hole formation.

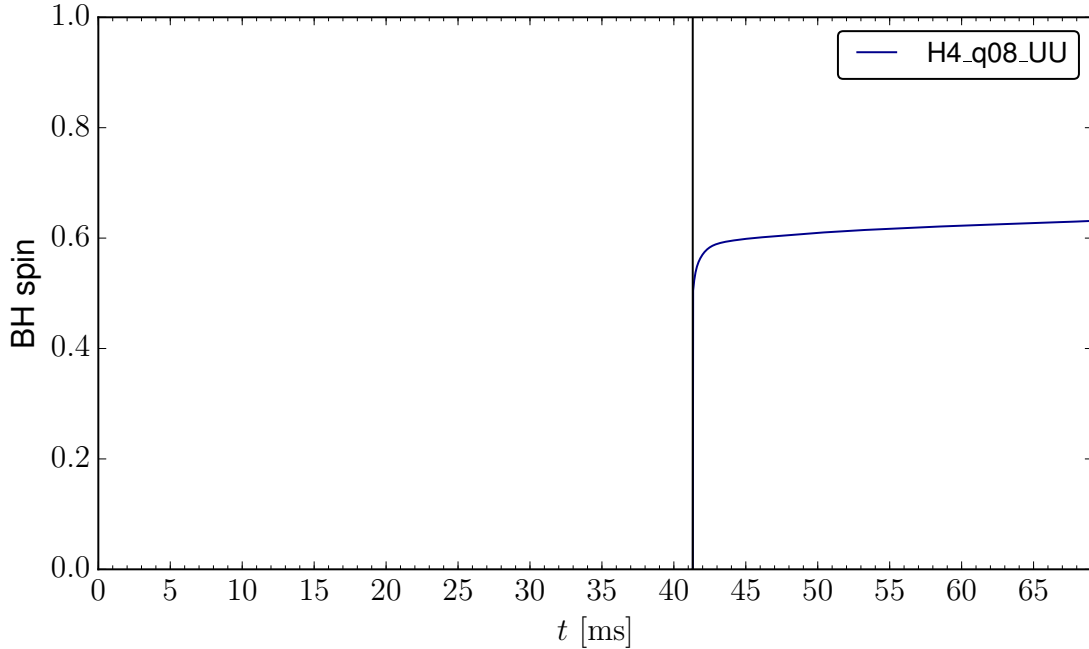


Figure 6.22 The time evolution of dimensionless BH spin a_{BH} for the H4_q08_UU model. The vertical black line denotes the time of black hole formation.

our standard resolution. The extent of the finest level is also larger than ours. The outer boundary in our work is slightly farther out than that in Ref. [49], but this is probably scarcely relevant for the results discussed here. In both cases the computational domain should be large enough to allow the evolution of the remnant and disk without the influence of boundary effects.

For the equal-mass H4 model, we also performed a simulation with the same grid spacing of $150m$ used for the lowest-resolution runs in Ref. [49]. In the following, we compare our main results to the $150m$ resolution run in Ref. [49] with the smallest initial magnetic field, $10^{15}G$, which is still 500 times stronger than ours. The strong field in Ref. [49] was chosen to facilitate the study of magnetic instabilities, while our aim is to use values more likely to occur in nature.

We find a HMNS lifetime of $10.9ms$, which agrees within 10% with the value shown in Fig. 2 of Ref. [49]. The dimensionless BH spin $10ms$ after merger in our simulation is 0.70, which agrees well with the value 0.69 reported in Ref. [49] (albeit for their $70m$ resolution run). Also the disk mass of $0.06M_{\odot}$ we found (at the same time) is identical to the value given in Ref. [49]. Therefore, the physical conditions for magnetic field amplification are very similar, apart from the different initial field strength.

In our run, the magnetic energy increases from $\approx 10^{43}$ erg at merger time to $\approx 10^{47}$ erg at the time of BH formation. In Ref. [49], the energy is already at this level at merger time and is amplified less than 1 order of magnitude in the $150m$ resolution run (in stark contrast to their higher-resolution runs). After collapse, the remaining energy outside the BH in-

creases from $\approx 10^{47}$ erg up to almost $\approx 10^{49}$ erg, at which point it saturates. In our simulation, the energy first stagnates around 5×10^{46} erg, and then starts growing again around $30ms$ after merger, up to a value of 4×10^{49} erg reached $60ms$ after merger. We do not observe saturation at this amplitude, but we cannot rule it out at later times. The reasons for the different behavior are unclear. Reference [49] clearly demonstrated that a $150m$ resolution is insufficient to resolve the field amplification in the disk, therefore the differences should not be taken too seriously. That said, we notice that Ref. [49] already reached a slightly higher magnetic energy directly after collapse, which makes it easier to resolve MRI effects in the disk. This might explain the delayed onset of amplification in our case. For more details about our high-resolution run we refer to Sec. 6.3.8, where the differences with respect to our standard resolution run are discussed.

An important statement in Ref. [49] is that no coherent structure of the poloidal component was found. This contrasts with our results with a lower initial magnetic field. Comparing the field lines shown in Fig. 6.18 to the ones in Fig. 1 of Ref. [49], we find indeed that the “twister” structure exposed in the former cannot be seen in the latter. On the other hand, the absence of a strongly collimated field along the BH axis reported in Ref. [49] agrees with our findings. The apparent absence of the twister structure might also be an artifact of the different selection of field lines and the larger scale of the plot in Ref. [49], resulting in a lower field line density near the “twister” structure. Furthermore, we made an effort to avoid seeds in the less regular regions between field lines of opposite direction. For those reasons, and also because of the lower resolution of our run, the comparison of the field structure remains rather inconclusive. We note however that our results do not rely solely on the field line plots. Using histograms in Fig. 6.17, we demonstrate that the dependence of the field energy on the θ coordinate is relatively flat and only falls off strongly between $50\text{--}30^\circ$ around the spin axis.

Finally, we note the study [48], in which additional refinement levels are added, down to a grid spacing of $17.5m$, in order to resolve the Kelvin-Helmholtz (KH) instability during the first few ms after merger. Those results show that a much higher resolution than the one implemented in our simulations is necessary in order to fully resolve the magnetic field amplification due to the KH instability during merger. Therefore, the magnetic field amplification inside the HMNS is most likely underestimated by our runs. The question of how this influences the post-collapse phase is not trivial, since an important fraction of the magnetic energy produced in the shear layer is likely to be swallowed by the BH upon collapse.

6.3.7 Unequal-Mass H4 model

For the H4 EOS, we found an enormous influence of the mass ratio on the magnetic field amplification (see also Section 6.3.8). The total magnetic energy and the maximum of the magnetic field are shown in Figures 6.13 and 6.14 in comparison to the equal-mass H4 model as well as the ideal-fluid models. As one can see, the lifetime of the HMNS ($\approx 24ms$) for the H4 unequal-mass case is more than twice as long as that for the H4 equal-mass case. During this phase, the field is growing exponentially, with the exception of the last $5ms$ before collapse. The time scale of the exponential growth is also longer than for the equal-mass case. Shortly before the collapse to a BH, the energy is around 4 orders of

magnitude larger than for the equal-mass case, and the maximum field strength more than 2 orders of magnitude larger. The fact that these values do not change drastically during collapse implies that most of the energy was contained in regions well outside the HMNS and that the field was also strongest there. As discussed in Section 6.3.8, we attribute at least part of this much stronger amplification to the magnetorotational instability.

The amplification after the collapse to a BH is comparable in growth rate to the ideal-fluid unequal-mass case (which showed a prompt collapse after merger). We conclude that the lifetime of the HMNS is a very important factor for the post-collapse field strength in the torus. It is likely that the large differences we see between the ideal-fluid and H4 unequal-mass cases are mostly due to the chosen total mass, i.e. we expect more similar results when comparing H4 and ideal-fluid EOS unequal-mass models with total masses chosen such that the HMNS lifetime is the same. Parameters other than the HMNS lifetime, namely disk mass, BH spin (the time evolution of the spin is in Figure 6.22), and accretion rate, are comparable to the IF_q08 case and cannot explain the much larger amplification.

The structure and distribution of the magnetic field 32ms after merger is shown in Figures 6.17 and 6.18. Apart from the increased amplitude, we find that for the unequal-mass case, a larger fraction of the energy is contained in the toroidal field near the equator. The field strength B_{90} reaches $\sim 6 \times 10^{15}G$ near the equator, more than 2 orders of magnitude above the strength for the equal-mass case ($\sim 3 \times 10^{13}G$). The opening angle of the conical structure is also smaller. As in the equal-mass case, the field near the axis does not contribute significantly to the total magnetic energy, and the field strength B_{90} near the axis is around 2 orders of magnitude below the equatorial value. Due to the overall increase in amplitude however, this now corresponds to a field strength $B_{90} \approx 3 \times 10^{13}G$ near the axis.

6.3.8 Influence of Resolution

We performed simulations at different resolutions for the ideal-fluid and H4 equal-mass models (IF_q10_UU and H4_q10). First, we discuss the ideal-fluid case, while the H4 case will be discussed at the end of this section. In the last paragraph, given its particular relevance, we will also discuss the impact of the chosen resolution on the unequal-mass H4 model (H4_q08).

Figure 6.23 shows the evolution of the maximum rest-mass density and magnetic energy at three different resolutions: $dx \approx 177, 222,$ and $277m$ (where dx is the finest grid spacing). The resolution affects the rest-mass density evolution only in the post-merger phase. The lifetime of the HMNS is extremely sensitive to small numerical errors and numerical convergence is difficult to achieve. In our case, higher resolutions resulted in a longer lifetime, and we see no convergence for the employed resolution range. Note however that in general the lifetime of HMNSs also depends very strongly on their mass.

The HMNS lifetime directly influences the disk mass, because the strong oscillations of the HMNS in conjunction with the rapid rotation constantly eject matter into the disk. Indeed, the disk mass increases from $0.015M_{\odot}$ for the lowest resolution (and shortest HMNS lifetime) to $0.077M_{\odot}$ at the highest resolution. The mass and spin of the BH on the other hand are only weakly affected by the HMNS lifetime. The differences between high and medium resolution at 30ms after collapse are both below 1.5%.

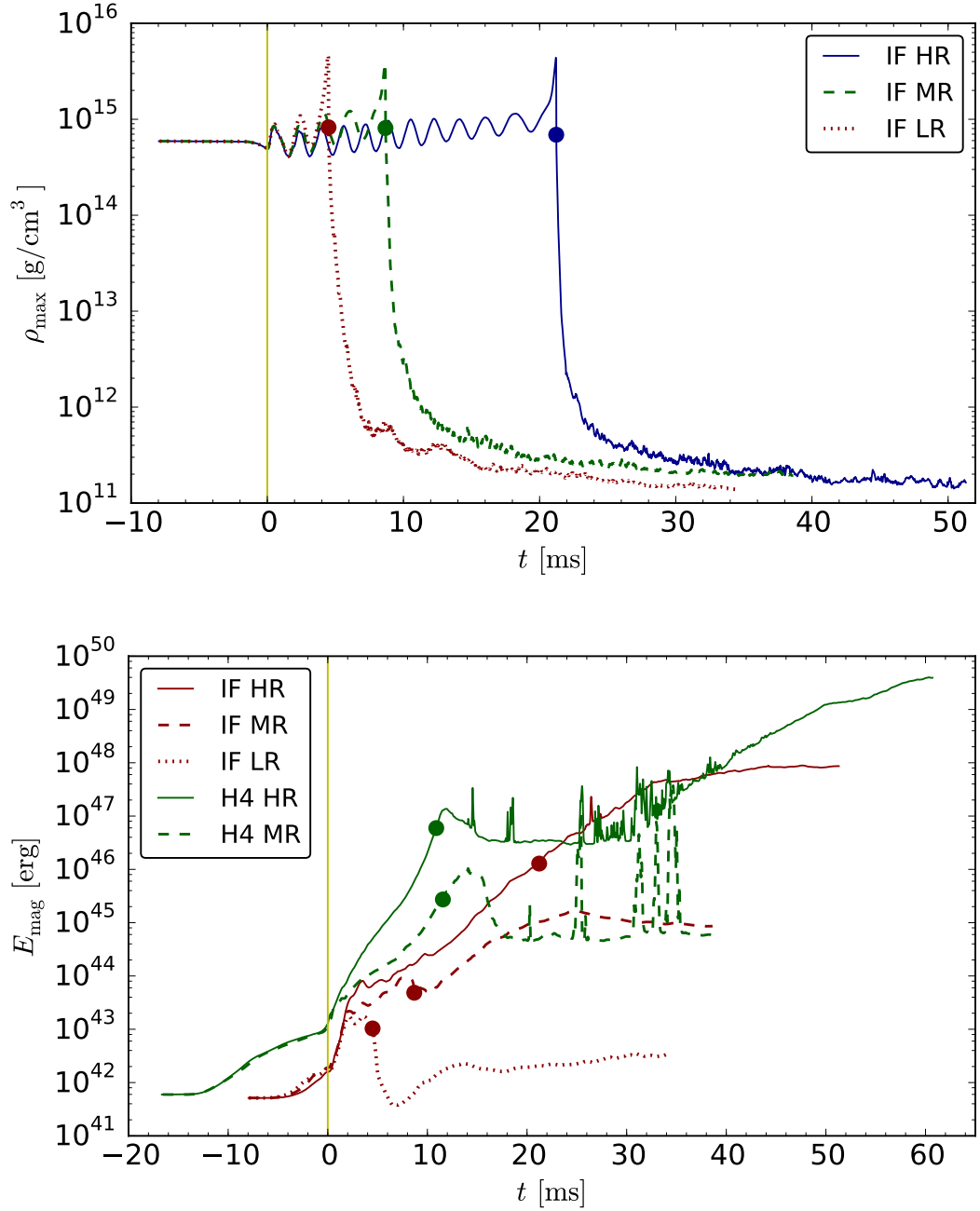


Figure 6.23 Evolution of maximum rest-mass density (upper panel) and magnetic energy (lower panel) for the equal-mass ideal-fluid model IF_q10_UU at different resolutions, with finest grid spacing of $dx \approx 177, 222, 277$ m for the high, medium and low resolutions, respectively. The evolution of the magnetic energy is also shown for the equal-mass H4 model H4_q10 with two different resolutions: $dx \approx 150$ m (HR) and 186 m (MR).

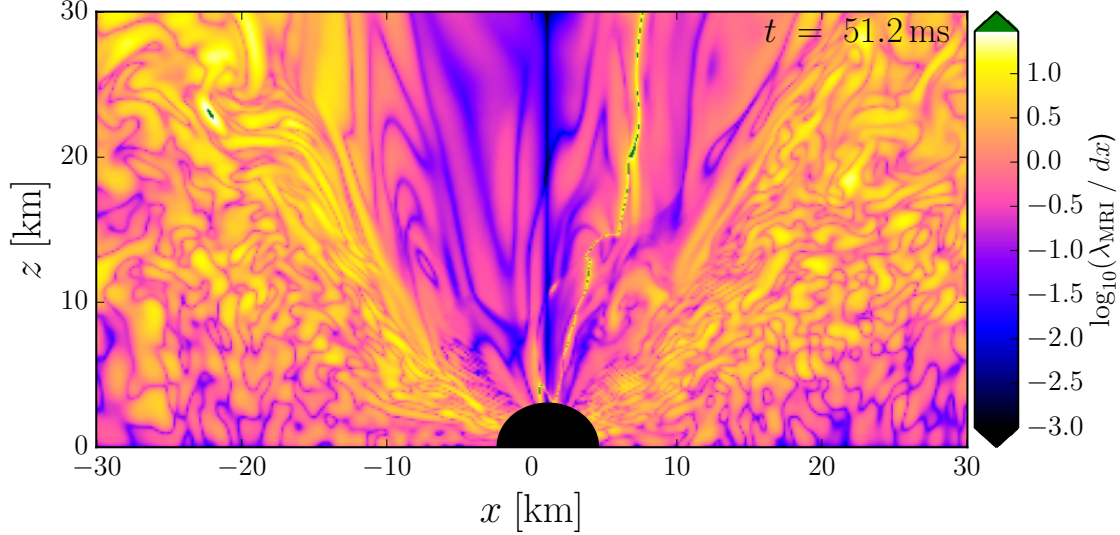


Figure 6.24 Meridional view of λ_{MRI}/dx for the highest-resolution simulation ($dx \approx 177$ m) of model IF_q10_UU, towards the end of the simulation ($t = 51.2$ ms).

During the first ~ 2 ms after merger, the magnetic energy shown in the lower panel of Fig. 6.23 exhibits an exponential increase, with a growth rate that depends only weakly on the resolution. The saturation of this exponential growth on the other hand sets in later (and at higher energies) for higher resolution. This amplification is most likely associated (at least in part) with the KH instability, which can be captured only on scales larger than the grid spacing and therefore is not entirely accounted for in our simulations.

In the subsequent evolution with medium and high resolution, the energy grows exponentially at comparable rate, but more slowly than directly after merger. We can attribute this to amplification of the field in the disk, since the additional energy is obviously not swallowed into the BH during the collapse of the HMNS, and because the amplification continues after collapse until it saturates. For the low resolution, the BH forms shortly after merger and the evolution of the field energy is due to the disk afterwards. For all resolutions, the energy increase ceases at some point. With increasing resolution, we observe a longer growth phase and a higher final amplitude. The difference between low and high resolution is more than 5 orders of magnitude. One possible explanation would be that the magnetic field amplification mechanism is acting also on small scales which are better resolved with a finer grid spacing.

One such mechanism that could operate in the disk is the MRI. The wavelength of the fastest growing mode of the MRI is approximately given by $\lambda_{\text{MRI}} \approx (2\pi/\Omega) \times B_k / \sqrt{4\pi\rho}$, where Ω is the angular velocity and B_k the magnetic field strength along the corresponding wave vector. In order to properly resolve this effect the finest grid spacing dx has to cover λ_{MRI} with at least 10 points (see, e.g., Ref. [80]). Figure 6.24 shows the ratio λ_{MRI}/dx for

the highest-resolution run ($dx \approx 177m$) at the end of the simulation. In this plot, the total magnetic field strength is used instead of B_k , and therefore the given ratio represents an upper limit. The ratio reaches maximum values ≈ 5 – 10 along the conical structure separating the disk from the funnel, where the magnetic field is the strongest. This indicates that a resolution $dx \lesssim 100m$ would be necessary in order to start resolving the MRI in that region. We note however that our formula for the wavelength does not take into account general-relativistic corrections and uses an idealized disk model.

Saturation of the amplification is not the only possible contribution to the flattening of the magnetic energy growth that happens ~ 15 – $20ms$ after collapse. Since the accretion time scale of the disk is $\sim 50ms$, we can expect that the magnetic energy contained in the accreted matter is relevant. Assuming that the magnetic strength in the inner disk grows as fast as in the remaining disk, the net increase would be zero when the accretion time scale and growth time scale agree. On the other hand, the fact that the maximum field strength and B_{90} saturate as well disfavors this scenario. Then again, the change of the disk structure due to accretion could affect the amplification mechanism, which would make the outcome sensitive again to the time of the collapse. The picture is complicated even more by the differences in disk mass due to the different HMNS lifetimes. For those reasons we cannot conclusively associate the flattening of the magnetic energy evolution to an actual saturation of the involved magnetic field amplification mechanisms.

The final magnetic energy between medium and high resolution differs by about 3 orders of magnitude, with the highest-resolution case reaching an increase of more than 6 orders of magnitude in E_{mag} compared to the beginning of the simulation. This amplification factor should be regarded as a lower limit that might be overcome with even higher resolution.

We now turn our attention to the H4 equal-mass model. In this case, we performed simulations at two different resolutions $dx \approx 186m$ (MR) and $150m$ (HR). The latter corresponds to the grid spacing employed in the lowest-resolution run of Ref. [49] for a very similar model. A direct comparison has already been presented in Section 6.3.6. The lower panel of Fig. 6.23 shows the evolution of the magnetic energy for the two H4 simulations. In contrast with the ideal-fluid case, there is no significant difference in the time of collapse to a BH (circle markers). Prior to collapse, the magnetic field amplification is stronger in the higher-resolution case, indicating that the dominant amplification mechanisms are not fully resolved. As for the ideal-fluid case, we estimated λ_{MRI}/dx and found that only some isolated lumps inside the “twister” structure are resolved with more than 10 grid points for the high-resolution case. In the highest-resolution run, a further increase in magnetic energy is observed some time after BH formation, corresponding to a strong amplification in the accretion disk. The simulation stops about $50ms$ after collapse and we find an overall change in magnetic energy of almost 8 orders of magnitude compared to initial data. This corresponds to an average increase of the magnetic field strength of about 4 orders of magnitude and it could be even larger with higher resolution.

For the unequal-mass H4 model we performed only one simulation with a finest grid spacing of $dx \approx 186m$. Nevertheless, because the model shows by far the strongest magnetic field amplification (c.f. Fig. 6.13), it is important to assess how well the MRI is resolved in this case. As shown in Figure 6.25 and differently from all other models in this

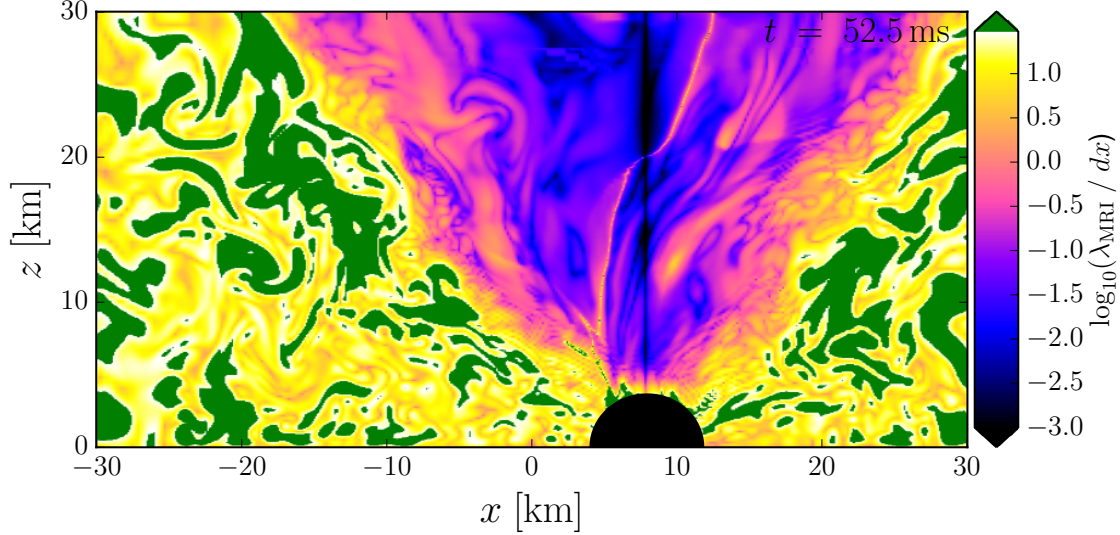


Figure 6.25 Same as Figure 6.24 for model H4_q08 at resolution $dx \approx 186$ m and at $t = 52.5$ ms.

study, at the end of the simulation $\lambda_{\text{MRI}}/dx > 10$ almost everywhere in the accretion disk. We attribute this to the fact that the magnetic field strength becomes higher because of the much longer lifetime of the HMNS and this makes λ_{MRI} larger. In turn, the MRI is better resolved, leading to a stronger amplification and thus to an even stronger magnetic field. This positive-feedback process provides a likely explanation for the fact that this particular model ends up with a magnetic energy that is several orders of magnitude higher. However, future simulations at higher resolution will be necessary in order to confirm this picture.

6.3.9 Constraints violation

To see the numerical accuracy of the simulations, we present the time evolutions of the Hamiltonian and momentum constraints for the IF_q10_UU, IF_q08_UU, H4_q10_UU and H4_q08_UU models in Figures 6.27, 6.28, 6.29 and 6.30, respectively. Here we also do not show the cases of IF_q10_UD and IF_q10_DD models since the difference of magnetic field configurations does not affect so much on the Hamiltonian and momentum constraints.

In models IF_q10_UU, H4_q10_UU and H4_q08_UU, the constraints show a similar behaviour. During inspiral the values of the Hamiltonian and momentum constraints are $\sim 10^{-2}$ and $\sim 10^{-4}$, respectively, then $\sim 10^{-1}$ and $\sim 10^{-3}$ in the following HMNS phase, finally $\sim 10^{-3}$ and $\sim 10^{-3}$ (in the IF_q10_UU model) or $\sim 10^{-4}$ and $\sim 10^{-4}$ (in the H4_q10_UU and H4_q08_UU models) after forming black holes. While in the IF_q08_UU model the values behave differently since the NSs promptly collapse to a black hole after merger.

One can see flat constraints lines starting from the formation of an apparent horizon and lasting for ~ 1 ms in the IF_q10_UU model, and increases of the constraints after

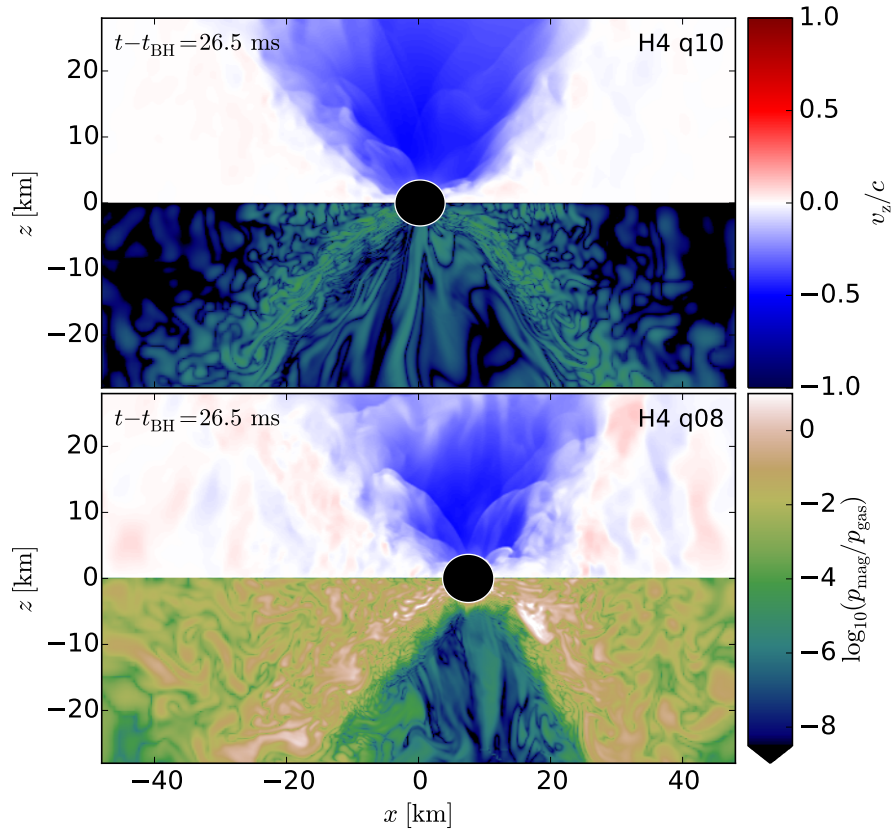


Figure 6.26 Meridional view of BH and accretion torus for the equal- and unequal-mass H4 simulations. The panels refer to 26.5 ms after BH formation and show in the top half ($z > 0$) the fluid velocity along the z axis and in the bottom half ($z < 0$) the magnetic-to-fluid pressure ratio in log scale.

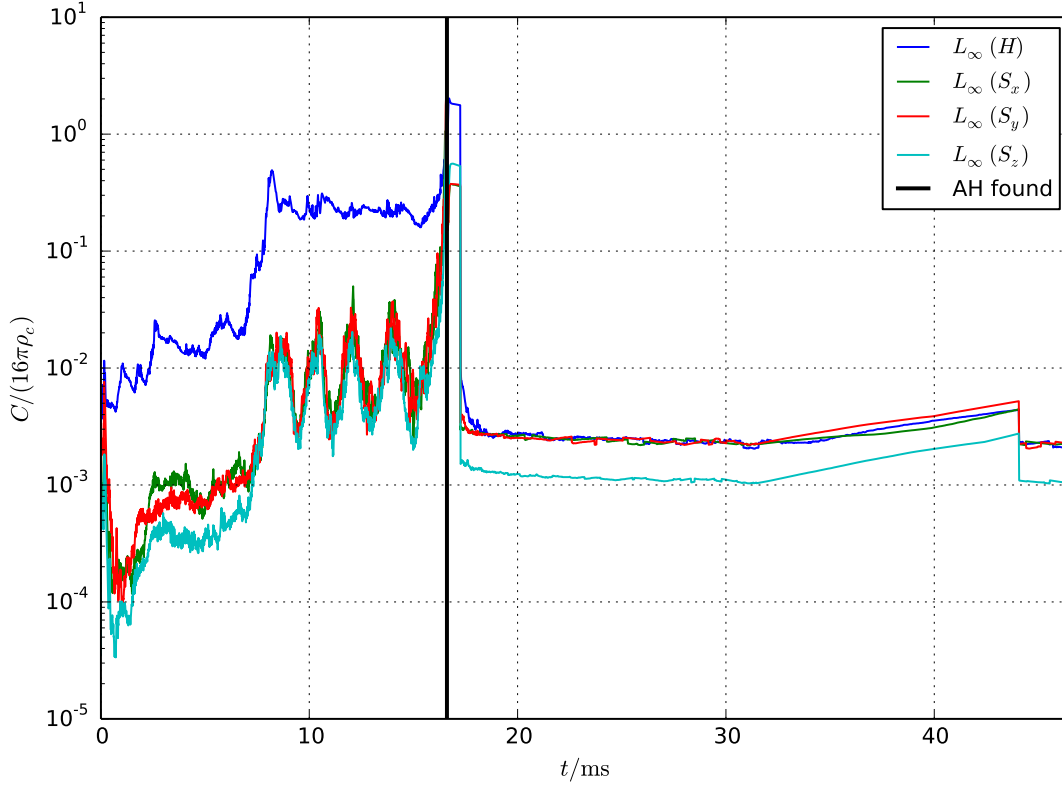


Figure 6.27 Evolution of the maximum values for the Hamiltonian and momentum constraints for the IF_q10_UU model. The relationship between line colors and physical quantities is the same as Figure 5.10.

forming black holes in the IF_q10_UU and H4_q10_UU models. These are due to the failure in finding apparent horizons. The increases of the constraints just reflect the values inside the black holes (when an apparent horizon is not found, our code gives the maximum of the constraints in all numerical grids including the black hole).

6.4 Short Gamma-Ray Bursts and Other Electromagnetic Signals

The possibility that the merger of two NSs may be accompanied by an SGRB has been discussed for several decades (see, i.e., Refs. [65, 28, 63, 75]). The generally invoked scenario is one in which the merger product is a BH surrounded by a massive accreting torus. The rapid accretion of the disk onto the newly formed BH provides the central engine for the burst. Another possibility that has been suggested for powering the engine is the electromagnetic spindown emission from a highly magnetized NS (see, i.e., Refs. [23, 59]), which survives for some time before collapsing to a BH or remains as a

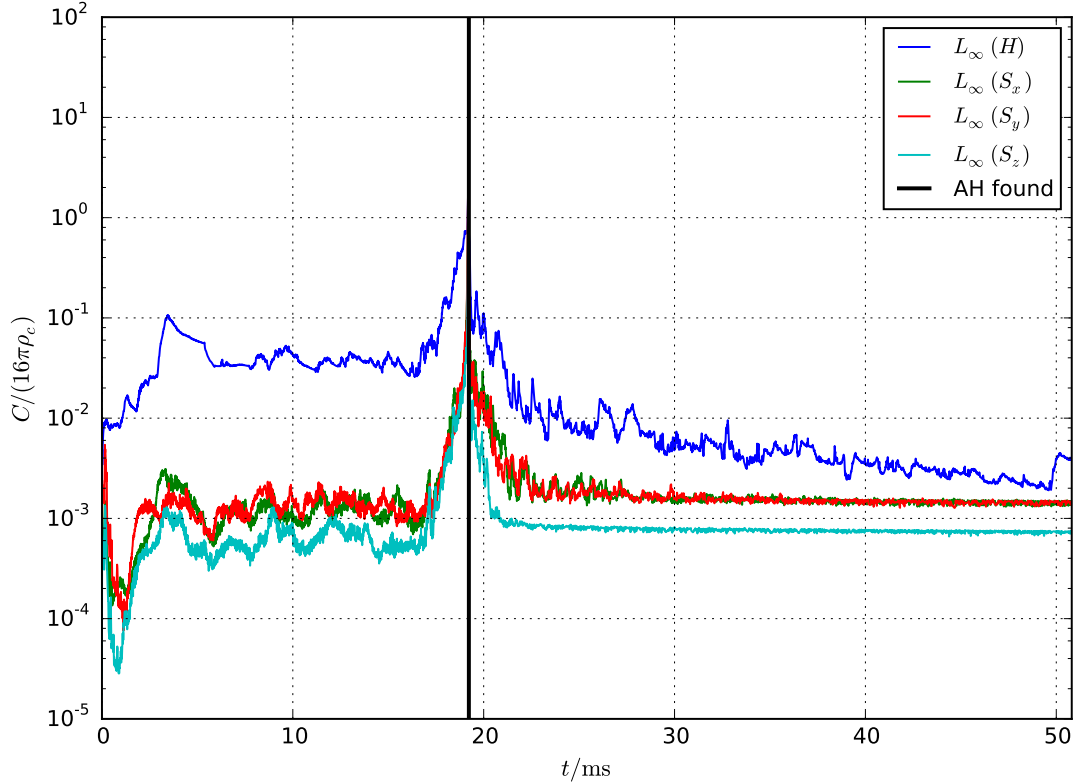


Figure 6.28 Evolution of the maximum values for the Hamiltonian and momentum constraints for the IF_q08_UU model. The relationship between line colors and physical quantities is the same as Figure 5.10.

stable NS (if allowed by its mass [33]). Finally, an alternative “time-reversal” scenario has been proposed [21, 20] in which the NS survives for a long time (up to spindown time scales) before eventually collapsing to a BH, and while its rotational energy powers a long-lasting X-ray signal (potentially explaining the X-ray afterglows commonly observed by *Swift*; see, e.g., Ref. [74]), the SGRB itself is powered by accretion onto the resulting BH, as in the standard scenario. In this work we focus on the first, most studied case in which a BH is formed in less than 100ms after merger.

The γ -ray emission is believed to be produced within a relativistic outflow (at the distances at which this becomes optically thin), and hence a crucial ingredient of any SGRB model is its ability to drive a jet. Two main mechanisms have been invoked: neutrinos (see, e.g., Ref. [75]) and magnetic fields. At high accretion rates, neutrinos can, in principle, tap the thermal energy of the disk produced by viscous dissipation and liberate large amounts of its binding energy via the $\nu\bar{\nu} \rightarrow e^+e^-$ process in regions of low baryon density. However, recent simulations of the hyperaccreting disk that include neutrino transfer have shown that, if the remnant torus and environment is that of a BNS merger, then neutrino emission

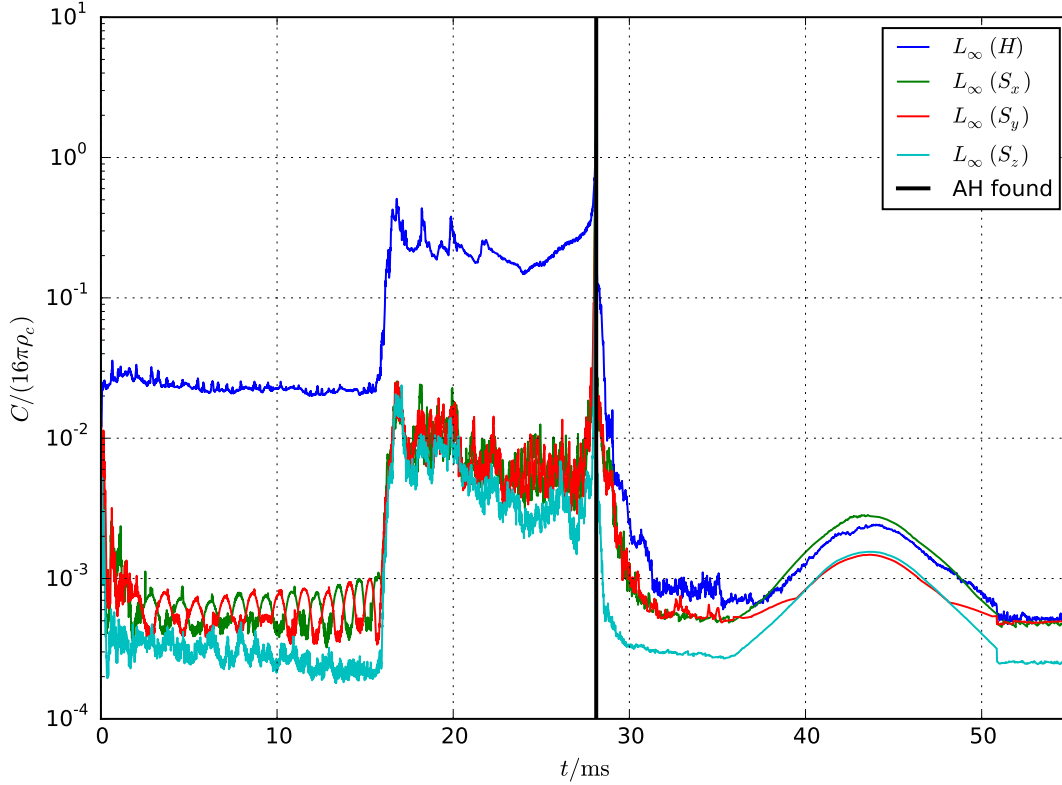


Figure 6.29 Evolution of the maximum values for the Hamiltonian and momentum constraints for the H4.q10_UU model. The relationship between line colors and physical quantities is the same as Figure 5.10.

is too short and too weak to yield enough energy for the outflow to break out from the surrounding ejecta as a highly relativistic jet [45]. Hence, it has been concluded that neutrino annihilation alone may not be able to power SGRBs from BNS mergers.

On the other hand, a strong poloidal magnetic field around a spinning BH can extract rotational energy and power an outflow [16]. This mechanism is commonly considered the most viable one for producing jets. Therefore, the topology of the post-merger magnetic field in our simulations plays an especially important role. Evidence for a geometrical structure compatible with jet formation in the merger of a BNS was found in Ref. [72], although as already discussed earlier only recently it was possible to show that BNS mergers can actually produce an “incipient jet” along the spin axis of the resulting BH, defined as a collimated and mildly relativistic outflow that is at least partially magnetically dominated [76]. A similar result was obtained earlier for NS-BH binary mergers [67].

Our simulations show the formation of a spinning BH with spin parameter in the range ~ 0.6 – 0.8 (see Table 6.2) and surrounded by a torus of at least a few percent of a solar mass, with the unequal-mass models yielding the larger torus masses. These

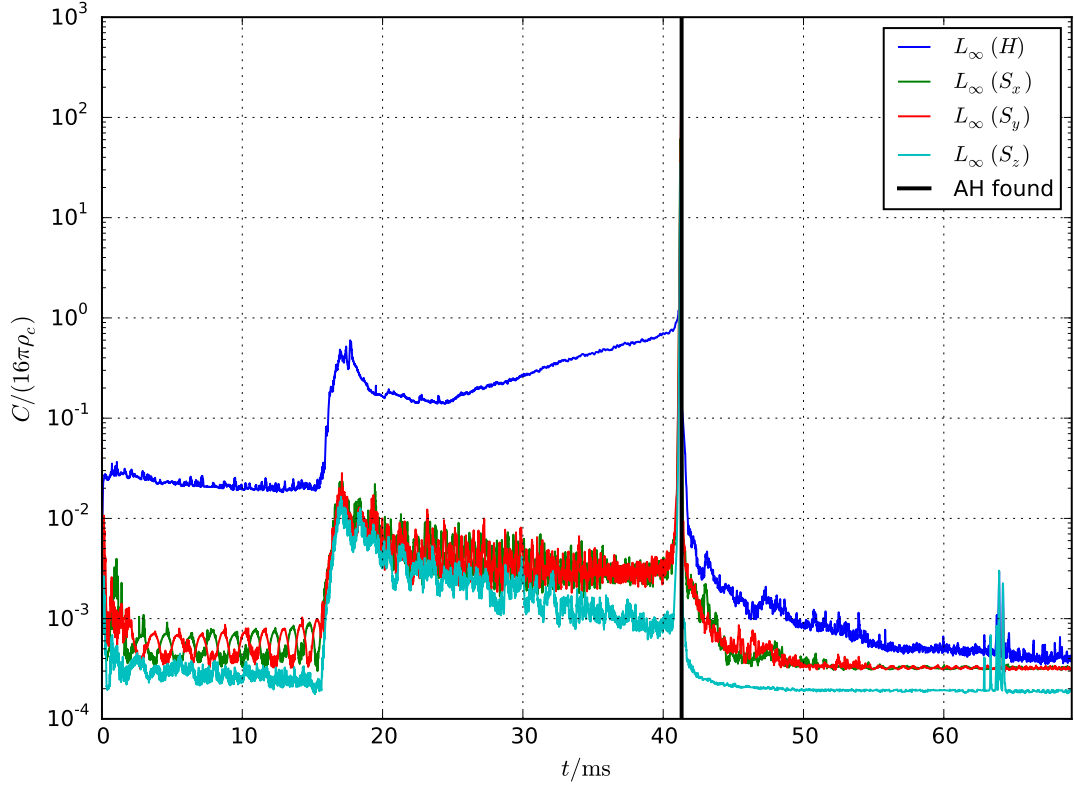


Figure 6.30 Evolution of the maximum values for the Hamiltonian and momentum constraints for the H4_q08_UU model. The relationship between line colors and physical quantities is the same as Figure 5.10.

results are consistent with previous results (e.g., Refs. [71, 72]). The average accretion rates are of the order of $\sim 1M_{\odot}s^{-1}$. For typical conversion efficiencies of accreted mass to observed radiation, these accretion rates and torus masses satisfy the energy requirements of the observed SGRBs, in particular in the unequal-mass cases [34]. However, the ability to launch a magnetically driven jet requires, in addition to a massive disk, also a strong poloidal field along the spin axis of the BH.

As discussed in the previous sections, in our simulations magnetic fields are strongly amplified after merger during the HMNS lifetime (see Figs. 6.13, 6.14, and 6.15). Magnetic field amplification continues in the disk after BH formation although in some cases an overall decrease of magnetic energy is observed, possibly due to accretion. As a result of the amplification, and in particular of the winding of the magnetic field lines, the toroidal component becomes dominant over the poloidal one in the disk. Along the edge of the accretion torus we observe the development of a mixed poloidal-toroidal “twister” structure. For the unequal-mass H4 model, we observed a particularly strong amplification of both the poloidal and toroidal components. For this case, the density-weighted mean value grows by

over 2 orders of magnitude (see Fig. 6.16). One important reason for this difference lies in the fact that, for this combination of EOS and NS masses, the HMNS formed upon merger survives for a much longer timescale compared with the other cases that we studied (see Sections 6.3.7 and 6.3.8). The higher torus mass and the stronger magnetic field amplification make the H4 unequal-mass case the most favorable of our models to produce a jet. Also the magnetic field morphology and the half-opening angle of the funnel (smaller than 30°) are compatible with what is needed to drive a SGRB (see Fig. 6.18 and 6.20).

Figure 6.26 shows the fluid velocity along the orbital axis and the magnetic-to-fluid pressure ratio⁴ for the equal- and unequal-mass H4 simulations, $26.5ms$ after BH formation. In both cases matter inside the funnel and along the spin axis of the BH is still infalling and in the unequal-mass case the pressure ratio indicates that the fluid is becoming magnetically dominated at the edges of the disk, but inside the funnel magnetic field pressure is subdominant. In conclusion, despite the fact that some favourable conditions are met, we do not find evidence of jet formation. Our results confirm the expectation that unequal-mass systems produce more massive disks (for the same total baryonic mass) and we find that longer-lived HMNSs can lead to a much stronger magnetic field amplification, which might also support the formation of a jet.

From our results, we are not in a position to exclude that the systems under investigation can form a jet. Our present simulations are limited to less than $30ms$ (in one case $50ms$) after BH formation and an outflow might still emerge on longer time scales. Moreover, magnetic field amplification mechanisms that act on scales that are too small to be properly resolved with our present resolution (such as the Kelvin-Helmholtz instability) would provide much stronger amplification (see, e.g., Refs. [48, 49, 80]) and thus influence the dynamics.

Our simulations lack a neutrino treatment. As such, we cannot compute the contribution of neutrinos to cooling and heating of the remnant disk. Most importantly, our simulations do not allow us to investigate the emergence of a jet driven by neutrino annihilation. However, as discussed above, Ref. [45] concluded that for the BNS merger scenario to yield a SGRB, jets must be magnetically driven. Lacking neutrinos in our treatment should not prevent the simulations from showing the emergence of such a magnetic jet. Nevertheless, neutrinos can still have an impact on the evolution of both the HMNS and the accretion disk.

In addition to the prompt γ -ray emission produced within the relativistic outflow and the associated X-ray and optical afterglows, the merger of two NSs is also expected to create a significant amount of neutron-rich radioactive elements, whose decay should result in a transient signal, the so-called “kilonova” or “macronova”, in the days following the burst (see, e.g., Refs. [73, 58]). The emerging radiation is expected to peak in the near IR, due to the large optical opacity of the heavy r -process elements, and to be nearly isotropic. As such, it constitutes an interesting complement to the prompt gamma-ray emission, which is expected to be generally beamed. Kilonova candidates were found to be associated with GRB 130603B [83], a SGRB at redshift $z = 0.356$, with GRB 060614 [86, 44], and with GRB 050709 [43]. Another promising electromagnetic signal from BNS mergers is the

⁴The ratio is defined as $\beta \equiv b^2/(2p)$, where $b^2 \equiv b^\mu b_\mu$ and b^μ is the 4-vector of the magnetic field as measured by the comoving observer [37].

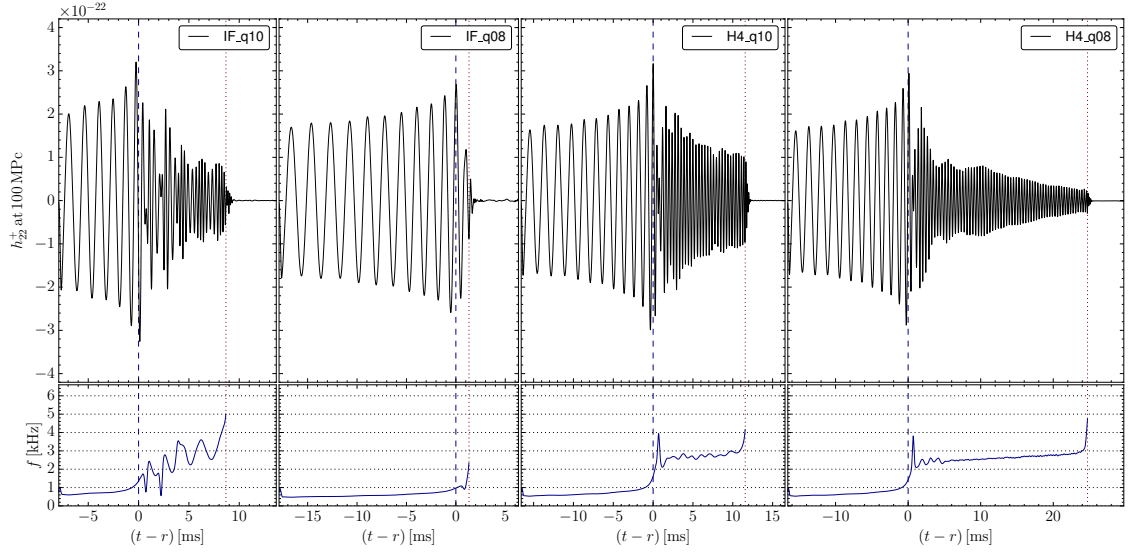


Figure 6.31 GW signal for models (from left to right) IF_q10, IF_q08, H4_q10 and H4_q08. The top panels show the strain at nominal distance of 100 Mpc. The lower panels show the instantaneous frequency.

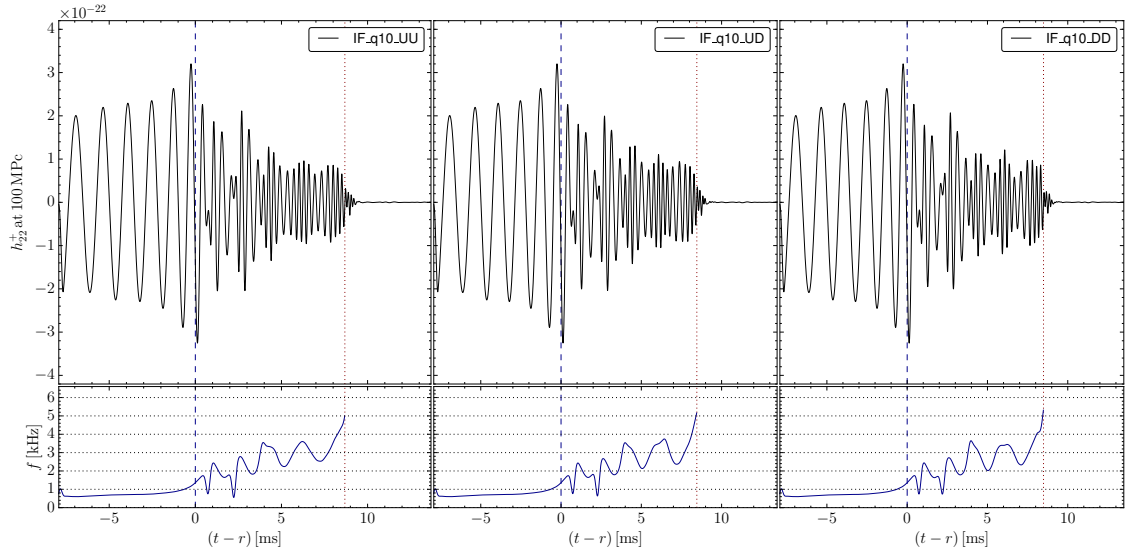


Figure 6.32 GW signal for models (from left to right) IF_q10_UU, IF_q10_UD and IF_q10_DD. The top panels show the strain at nominal distance of 100 Mpc. The lower panels show the instantaneous frequency.

isotropic X-ray emission powered by the spindown of a long-lived NS remnant [78, 79], although such a signal is not expected if a BH is formed shortly (< 1 s) after merger.

The observation of SGRBs or other electromagnetic counterparts in combination

with the BNS merger GW signal will dramatically improve the scientific output of a detection. In the following section we discuss the GW emission from the BNS mergers studied in this work.

6.5 Gravitational Waves

For all runs we extract the GW signal at a fixed radius of ~ 1100 km via the Moncrief formalism (signal is extracted also via the Weyl scalar Ψ_4 , but only for cross-checking purposes). Note that extrapolation at infinity is not performed for any of our simulations.

In this section we present the strain of the GW signal as $h_{lm} = h_{lm}^+ + ih_{lm}^\times$, namely, the coefficients of the spin-weighted spherical harmonics expansion. In order to obtain the actual strain that would be measured by a GW detector, one should multiply our value by the spin-weighted spherical harmonics in order to take into account the signal direction. For each simulation we also extracted the instantaneous frequency of the GW from the phase velocity of the complex strain, which is shown in the bottom panels of Figs. 6.31 and 6.32.

In Fig. 6.31 we show the $l = m = 2$ component of the GW strain for models IF_q10, IF_q08, H4_q10 and H4_q08. While in the IF_q08 case, where the system promptly collapses to a BH, the GW includes only inspiral, merger, and ringdown, in all the other cases a HMNS is formed and therefore we have also a longer post-merger GW signal. In the IF_q10 case the GW frequency during the HMNS lifetime varies continuously. This behavior differs from the H4 cases, where the HMNS phases show signals with a very strong peak at specific frequencies. Note that in the H4 cases the HMNS has a longer lifetime, and in the H4_q10 case the post-merger GW signal also has a stronger amplitude with respect to the other models. As previously discussed, however, the lifetime of the remnant also depends on the resolution, with the HMNS surviving longer with higher resolution.

In terms of frequency, the H4 models show a drift towards higher frequencies during the post-merger phase, which is more evident in the H4_q08 case, where the remnant lasts longer and the value of the frequency oscillates less. In Table 6.2 we report for all models the frequency at merger f_{merger} and, for the H4 cases, also f_{HMNS} , which indicates the frequency corresponding to the most prominent post-merger peak in the GW spectrum (called f_{peak} in Ref. [15] and f_2 in Ref. [82]). We do not provide f_{HMNS} for the ideal-fluid models since IF_q08 has no HMNS remnant (it promptly collapses to a BH) and in IF_q10 the frequency oscillates too much to get an accurate estimate, as it is shown from both the amplitude and spectral behaviors.

We also studied whether the effect of magnetic field orientation had any impact on the GW signal. As shown in Fig. 6.32, this impact is minimal. This may change if the magnetic field is amplified to much larger values during merger.

Finally, in Figures 6.33 and 6.34 we plot the power spectra of the GW signals for all our simulations against present and future ground-based detector sensitivities (namely Advanced Virgo, Advanced LIGO, and the Einstein Telescope, all in the standard broadband configuration).

The power spectrum we show in the plots is given by $h_{eff}(f) = \sqrt{\tilde{h}_+^2(f) + \tilde{h}_\times^2(f)}$,

where \tilde{h}_+ and \tilde{h}_\times are the Fourier transforms of h_{lm}^+ and h_{lm}^\times for $l = m = 2$. From both Figures we can see that the inspiral phase would be detected by both Advanced Virgo and Advanced LIGO for all models. Moreover, in Fig. 6.33 we see that for the H4 models the post-merger peak of the signal due to HMNS oscillations would also be strong enough to be detected by Advanced LIGO and Virgo. If detected, this peak could play a very important role in constraining the NS EOS [15, 82, 81].

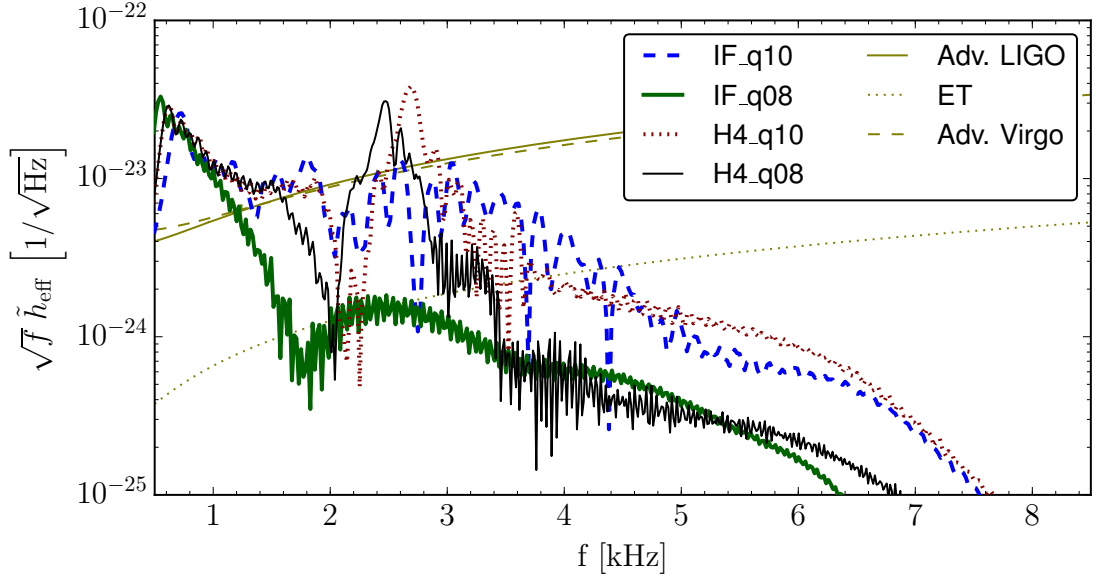


Figure 6.33 GW spectra (solid lines) for the four models of Fig. 6.31 in comparison to the sensitivity curves of GW detectors (dashed lines). The strain is given at distance of 100 Mpc.

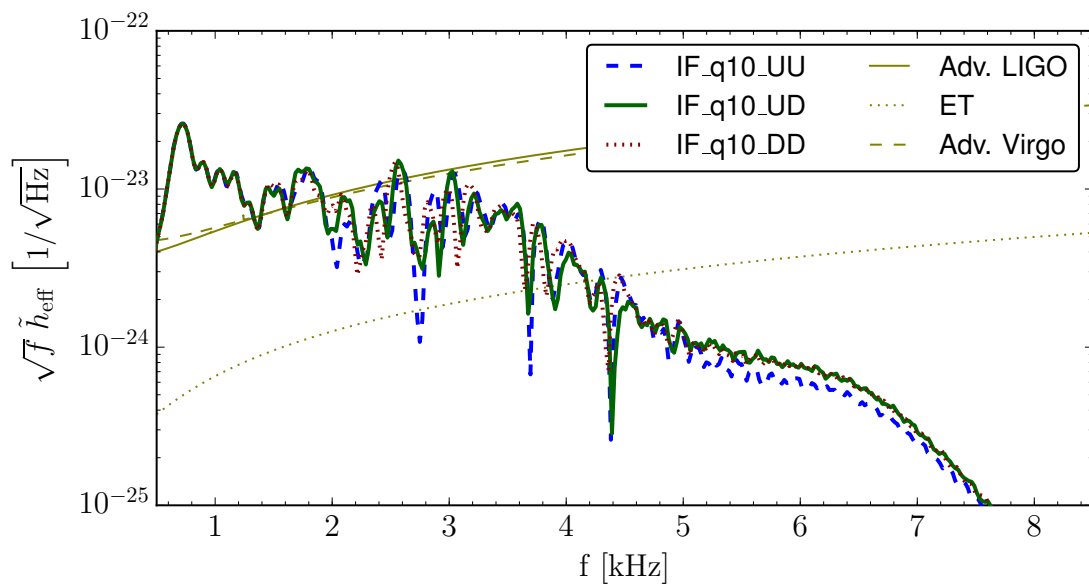


Figure 6.34 GW spectra (solid lines) for the three models of Fig. 6.32 in comparison to the sensitivity curves of GW detectors (dashed lines). The strain is given at distance of 100 Mpc.

Chapter 7

Conclusions

In this thesis I presented fully GRMHD simulations of BNS mergers employing three different EOSs: ideal-fluid, APR4, and H4. In the APR4 simulations, two neutron stars promptly collapse to a black hole after merger, and no significant amount of matter is left in the remnant disk around the formed black hole. Also, the amplification of magnetic field strength is not very large as the magnetized remnant is swallowed by the central black hole at merger. While, for the “low-mass” and “unequal-mass” cases massive disks are formed and a small amplification of the magnetic field was observed [29].

In the ideal fluid and H4 simulations, we have visualized magnetic field lines of post-merger remnant in order to investigate the field structure, in particular whether an ordered poloidal field is formed or not, because such a structure may lead to the formation of a relativistic jet and possibly to SGRBs. In all cases we observed the formation of an organized magnetic field structure aligned with the spin axis of the final black hole, regardless of EOS, magnetic field orientation and mass ratio, though we could not see a relativistic jet [47].

The fact that we could not see the formation of relativistic jet in any of our simulations is not unexpected, because our resolution is not high enough to fully resolve the KH instability and the MRI during the evolution. In addition, the time lapse of our simulations are limited to a few ms (in the APR4 simulations) or a few tens of ms (in the ideal fluid and H4 simulations) after the formation of a black hole though it may take more time to form a relativistic jet.

In all the simulations we also computed the GW signals and compared them with the sensitivity curves of current and future GW detectors. We investigated the effect of magnetic fields on GWs and for the magnetic field strength used in our work the effect is minimal. In particular we did not see any effect of the magnetic field initial orientation on the GWs.

Our future simulations will use higher resolution or implement a subgrid model in order to follow the magnetic field amplification more accurately. We will also run much longer simulations in order to study the possible formation of relativistic jets. Also, implementation of more realistic EOSs, such as finite-temperature EOSs, and neutrino emission would provide more realistic post-merger dynamics and GW emission.

A Visualizing the Field Structure

Our visualization method for the magnetic field aims at solving the following problems. First, the magnetic field in our simulations is organized in tubes, and the direction of the field between neighbouring tubes changes sign. The in-between field is typically weaker and less regular. Using random or regularly spaced seed points for the integration is bound to miss the strong field regions. Second, showing the field lines everywhere leads to visual clutter and obscures the global structure. We therefore have to choose a smaller number of field lines which are representative of the structure. It is important to use a well-defined automated method for the field line filtering since a biased selection can result in misleading plots. Finding a good selection rule is difficult because the field strength varies strongly between the different parts of the field we are interested in.

To solve the first problem, we divide the volume of interest into a coarse grid (15^3 cells). In each cell, we determine the location of maximum field strength and use it as a seed point. We then integrate the field lines for all seed points. The solution of the second problem is more involved. First, we divide our domain into bins regularly spaced in $\cos(\theta)$, where θ is the angle between the BH axis and the position vector relative to the BH. We then sort the field lines in each bin by their maximum field strength inside the given bin. Next, we assign to each field line the maximum of its rank in all bins it traverses. We then sort the field lines by this “maximum local importance” measure and keep only a given number of them.

This prescription results in a balanced distribution of field lines in the different parts of the field (axis, disk, torus) despite a strongly varying strength on both large and small length scales. One could argue however that the binning in terms of $\cos(\theta)$ might highlight conical structures where there are none in reality. For example, the strong field in the torus casts a “shadow” radially outwards where weaker field lines are not shown. To validate that the visual impression given by the 3D plots is correct, we also compared different visualizations, such as volume rendering of the field strength and simple 2D cuts.

Bibliography

- [1] J. Abadie, B. P. Abbott, R. Abbott, M. Abernathy, T. Accadia, F. Acernese, C. Adams, R. Adhikari, P. Ajith, B. Allen, and et al. TOPICAL REVIEW: Predictions for the rates of compact binary coalescences observable by ground-based gravitational-wave detectors. *Classical and Quantum Gravity*, 27(17):173001, September 2010.
- [2] B. P. Abbott and et al. Gw151226: Observation of gravitational waves from a 22-solar-mass binary black hole coalescence. *Phys. Rev. Lett.*, 116:241103, Jun 2016.
- [3] B. P. Abbott and et al. Observation of gravitational waves from a binary black hole merger. *Phys. Rev. Lett.*, 116:061102, Feb 2016.
- [4] A. Akmal, V. R. Pandharipande, and D. G. Ravenhall. Equation of state of nucleon matter and neutron star structure. *Phys. Rev. C*, 58:1804–1828, Sep 1998.
- [5] M. Alcubierre, B. Brügmann, T. Dramlitsch, J. A. Font, P. Papadopoulos, E. Seidel, N. Stergioulas, and R. Takahashi. Towards a stable numerical evolution of strongly gravitating systems in general relativity: The conformal treatments. *Phys. Rev. D*, 62(4):044034, August 2000.
- [6] M. Alcubierre, B. Brügmann, D. Pollney, E. Seidel, and R. Takahashi. Black hole excision for dynamic black holes. *Phys. Rev. D*, 64(6):061501, September 2001.
- [7] M. Anderson, E. W. Hirschmann, L. Lehner, S. L. Liebling, P. M. Motl, D. Neilsen, C. Palenzuela, and J. E. Tohline. Magnetized Neutron-Star Mergers and Gravitational-Wave Signals. *Physical Review Letters*, 100(19):191101, May 2008.
- [8] Luis Anton, Olindo Zanotti, Juan A. Miralles, Jose M. Marti, Jose M. Ibanez, Jose A. Font, and Jose A. Pons. Numerical 3+1 general relativistic magnetohydrodynamics: A Local characteristic approach. *Astrophys. J.*, 637:296–312, 2006.
- [9] R. Arnowitt, S. Deser, and C. W. Misner. Republication of: The dynamics of general relativity. *General Relativity and Gravitation*, 40:1997–2027, September 2008.
- [10] L. Baiotti, M. Shibata, and T. Yamamoto. Binary neutron-star mergers with Whisky and SACRA: First quantitative comparison of results from independent general-relativistic hydrodynamics codes. *Phys. Rev. D*, 82(6):064015, September 2010.

-
- [11] Luca Baiotti, Ian Hawke, Pedro Montero, and Luciano Rezzolla. A new three-dimensional general-relativistic hydrodynamics code. In R. Capuzzo-Dolcetta, editor, *Computational Astrophysics in Italy: Methods and Tools*, volume 1, page 210, Trieste, 2003. MSAIt.
- [12] Luca Baiotti, Ian Hawke, Pedro J. Montero, Frank Löffler, Luciano Rezzolla, Nikolaos Stergioulas, José A. Font, and Ed Seidel. Three-dimensional relativistic simulations of rotating neutron star collapse to a Kerr black hole. *Phys. Rev. D*, 71:024035, 2005.
- [13] D. S. Balsara and D. S. Spicer. A staggered mesh algorithm using high order godunov fluxes to ensure solenoidal magnetic fields in magnetohydrodynamic simulations. *J. Comput. Phys.*, 149:270–292, 1999.
- [14] Thomas W. Baumgarte and Stuart L. Shapiro. Numerical integration of Einstein’s field equations. *Phys. Rev. D*, 59:024007, December 1998.
- [15] A. Bauswein and H.-T. Janka. Measuring Neutron-Star Properties via Gravitational Waves from Neutron-Star Mergers. *Phys. Rev. Lett.*, 108(1):011101, January 2012.
- [16] R. D. Blandford and R. L. Znajek. Electromagnetic extraction of energy from Kerr black holes. *MNRAS*, 179:433–456, May 1977.
- [17] C. Bona, J. Massó, E. Seidel, and J. Stela. New Formalism for Numerical Relativity. *Physical Review Letters*, 75:600–603, July 1995.
- [18] David Brown, Peter Diener, Olivier Sarbach, Erik Schnetter, and Manuel Tiglio. Turduckening black holes: an analytical and computational study. *Phys. Rev. D*, 79:044023, 2009.
- [19] Y. Choquet-Bruhat. Théorème d’existence pour certains systèmes d’équations aux dérivées partielles non linéaires. *Acta Mathematica*, 88(141), 1952.
- [20] R. Ciolfi and D. M. Siegel. Short gamma-ray bursts from binary neutron star mergers: the time-reversal scenario. *ArXiv e-prints:1505.01420*, May 2015.
- [21] R. Ciolfi and D. M. Siegel. Short Gamma-Ray Bursts in the ”Time-reversal” Scenario. *Astrophys. J. Letters*, 798:L36, January 2015.
- [22] P. Colella and P. R. Woodward. The piecewise parabolic method (ppm) for gas-dynamical simulations. *J. Comput. Phys.*, 54:174, 1984.
- [23] Z. G. Dai, X. Y. Wang, X. F. Wu, and B. Zhang. X-ray Flares from Postmerger Millisecond Pulsars. *Science*, 311:1127–1129, February 2006.
- [24] S. Dall’Osso, B. Giacomazzo, R. Perna, and L. Stella. Gravitational Waves from Massive Magnetars Formed in Binary Neutron Star Mergers. *Astrophys. J.*, 798:25, January 2015.
- [25] G. Darrois. Les équations de la gravitation einsteinienne. 48 p. Paris, Gauthier-Villars (Mémorial des sciences mathématiques fasc. 25)., 1927.

- [26] K. Dionysopoulou, D. Alic, and L. Rezzolla. General-relativistic resistive-magnetohydrodynamic simulations of binary neutron stars. *Phys. Rev. D*, 92(8):084064, October 2015.
- [27] Matthew D. Duez, Yuk Tung Liu, Stuart L. Shapiro, Masaru Shibata, and Branson C. Stephens. Evolution of magnetized, differentially rotating neutron stars: Simulations in full general relativity. *Phys. Rev. D*, 73:104015, May 2006.
- [28] D. Eichler, M. Livio, T. Piran, and D. N. Schramm. Nucleosynthesis, neutrino bursts and gamma-rays from coalescing neutron stars. *Nature*, 340:126–128, July 1989.
- [29] A Endrizzi, R Ciolfi, B Giacomazzo, W Kastaun, and T Kawamura. General relativistic magnetohydrodynamic simulations of binary neutron star mergers with the apr4 equation of state. *Classical and Quantum Gravity*, 33(16):164001, 2016.
- [30] Zachariah B. Etienne, Vasileios Paschalidis, Yuk Tung Liu, and Stuart L. Shapiro. Relativistic MHD in dynamical spacetimes: Improved EM gauge condition for AMR grids. *Phys. Rev.*, D85:024013, 2012.
- [31] Brian D. Farris, Roman Gold, Vasileios Paschalidis, Zachariah B. Etienne, and Stuart L. Shapiro. Binary black-hole mergers in magnetized disks: Simulations in full general relativity. *Phys. Rev. Lett.*, 109:221102, Nov 2012.
- [32] J. A. Font. Numerical hydrodynamics and magnetohydrodynamics in general relativity. *Living Reviews in Relativity*, 11(7), 2008. URL (cited on November 2nd 2016): <http://www.livingreviews.org/lrr-2008-7>.
- [33] B. Giacomazzo and R. Perna. Formation of Stable Magnetars from Binary Neutron Star Mergers. *Astrophys. J. Letters*, 771:L26, July 2013.
- [34] B. Giacomazzo, R. Perna, L. Rezzolla, E. Troja, and D. Lazzati. Compact Binary Progenitors of Short Gamma-Ray Bursts. *Astrophys. J. Letters*, 762:L18, January 2013.
- [35] B. Giacomazzo, L. Rezzolla, and L. Baiotti. Can magnetic fields be detected during the inspiral of binary neutron stars? *MNRAS*, 399:L164–L168, October 2009.
- [36] B. Giacomazzo, L. Rezzolla, and L. Baiotti. Accurate evolutions of inspiralling and magnetized neutron stars: Equal-mass binaries. *Phys. Rev. D*, 83(4):044014, February 2011.
- [37] Bruno Giacomazzo and Luciano Rezzolla. WhiskyMHD: a new numerical code for general relativistic magnetohydrodynamics. *Class. Quantum Grav.*, 24:S235, 2007.
- [38] N. K. Glendenning and S. A. Moszkowski. Reconciliation of neutron-star masses and binding of the Lambda in hypernuclei. *Physical Review Letters*, 67:2414–1417, October 1991.
- [39] L. Gualtieri, R. Ciolfi, and V. Ferrari. Structure, deformations and gravitational wave emission of magnetars. *Classical and Quantum Gravity*, 28(11):114014, June 2011.

- [40] A. Harten, P. D. Lax, and B. van Leer. On upstream differencing and godunov-type schemes for hyperbolic conservation laws. *SIAM Rev.*, 25:35, 1983.
- [41] K. Hotokezaka, K. Kyutoku, H. Okawa, M. Shibata, and K. Kiuchi. Binary neutron star mergers: Dependence on the nuclear equation of state. *Phys. Rev. D*, 83(12):124008, June 2011.
- [42] R. A. Hulse and J. H. Taylor. Discovery of a pulsar in a binary system. *Astrophys. J. Letters*, 195:L51–L53, January 1975.
- [43] Z.-P. Jin, K. Hotokezaka, X. Li, M. Tanaka, P. D’Avanzo, Y.-Z. Fan, S. Covino, D.-M. Wei, and T. Piran. The Macronova in GRB 050709 and the GRB-macronova connection. *Nature Communications*, 7:12898, September 2016.
- [44] Z.-P. Jin, X. Li, Z. Cano, S. Covino, Y.-Z. Fan, and D.-M. Wei. The Light Curve of the Macronova Associated with the Long-Short Burst GRB 060614. *ApJ*, 811:L22, October 2015.
- [45] O. Just, M. Obergaulinger, H.-T. Janka, A. Bauswein, and N. Schwarz. Neutron-star Merger Ejecta as Obstacles to Neutrino-powered Jets of Gamma-Ray Bursts. *Astrophys. J. Letters*, 816:L30, January 2016.
- [46] W. Kastaun, R. Ciolfi, A. Endrizzi, and B. Giacomazzo. Structure of Stable Binary Neutron Star Merger Remnants: Role of Initial Spin. *ArXiv e-prints:1612.03671*, December 2016.
- [47] T. Kawamura, B. Giacomazzo, W. Kastaun, R. Ciolfi, A. Endrizzi, L. Baiotti, and R. Perna. Binary neutron star mergers and short gamma-ray bursts: Effects of magnetic field orientation, equation of state, and mass ratio. *Phys. Rev. D*, 94(6):064012, September 2016.
- [48] K. Kiuchi, P. Cerdá-Durán, K. Kyutoku, Y. Sekiguchi, and M. Shibata. Efficient magnetic-field amplification due to the Kelvin-Helmholtz instability in binary neutron star mergers. *Phys. Rev. D*, 92(12):124034, December 2015.
- [49] K. Kiuchi, K. Kyutoku, Y. Sekiguchi, M. Shibata, and T. Wada. High resolution numerical relativity simulations for the merger of binary magnetized neutron stars. *Phys. Rev. D*, 90(4):041502, August 2014.
- [50] K. Kiuchi, K. Kyutoku, and M. Shibata. Three-dimensional evolution of differentially rotating magnetized neutron stars. *Phys. Rev. D*, 86(6):064008, September 2012.
- [51] K. Kiuchi, S. Yoshida, and M. Shibata. Nonaxisymmetric instabilities of neutron star with toroidal magnetic fields. *Astron. Astrophys.*, 532:A30, August 2011.
- [52] C. Kouveliotou, C. A. Meegan, G. J. Fishman, N. P. Bhat, M. S. Briggs, T. M. Koshut, W. S. Paciesas, and G. N. Pendleton. Identification of two classes of gamma-ray bursts. *Astrophys. J. Letters*, 413:L101–L104, August 1993.

-
- [53] James M. Lattimer and Madappa Prakash. Neutron star observations: Prognosis for equation of state constraints. *Physics Reports*, 442(16):109 – 165, 2007. The Hans Bethe Centennial Volume 1906-2006.
- [54] A. Lichnerowicz. L'intégration des équations de la gravitation relativiste et le problème des n corps. *Journal de Mathématiques Pures et Appliquées*, 23(37), 1944.
- [55] Y. T. Liu, S. L. Shapiro, Z. B. Etienne, and K. Taniguchi. General relativistic simulations of magnetized binary neutron star mergers. *Phys. Rev. D*, 78(2):024012, July 2008.
- [56] F. Löffler, J. Faber, E. Bentivegna, T. Bode, P. Diener, R. Haas, I. Hinder, B. C. Mundim, C. D. Ott, E. Schnetter, G. Allen, M. Campanelli, and P. Laguna. The Einstein Toolkit: a community computational infrastructure for relativistic astrophysics. *Class. Quantum Grav.*, 29(11):115001, June 2012.
- [57] Duncan R. Lorimer. Binary and millisecond pulsars. *Living Reviews in Relativity*, 11(1):8, 2008.
- [58] B. D. Metzger, G. Martínez-Pinedo, S. Darbha, E. Quataert, A. Arcones, D. Kasen, R. Thomas, P. Nugent, I. V. Panov, and N. T. Zinner. Electromagnetic counterparts of compact object mergers powered by the radioactive decay of r-process nuclei. *MNRAS*, 406:2650–2662, August 2010.
- [59] B. D. Metzger, E. Quataert, and T. A. Thompson. Short-duration gamma-ray bursts with extended emission from protomagnetar spin-down. *MNRAS*, 385:1455–1460, April 2008.
- [60] V. Moncrief. Gravitational perturbations of spherically symmetric systems. I. The exterior problem. *Annals of Physics*, 88:323–342, December 1974.
- [61] A. Nagar and L. Rezzolla. Corrigendum: Gauge-invariant non-spherical metric perturbations of Schwarzschild black-hole spacetimes. *Classical and Quantum Gravity*, 23:4297, June 2006.
- [62] Takashi Nakamura, Ken-ichi Oohara, and Yasufumi Kojima. General relativistic collapse to black holes and gravitational waves from black holes. *Prog. Theor. Phys. Suppl.*, 90:1–218, 1987.
- [63] R. Narayan, B. Paczynski, and T. Piran. Gamma-ray bursts as the death throes of massive binary stars. *Astrophys. J. Letter*, 395:L83–L86, August 1992.
- [64] Feryal Özel, Gordon Baym, and Tolga Güver. Astrophysical measurement of the equation of state of neutron star matter. *Phys. Rev. D*, 82:101301, Nov 2010.
- [65] B. Paczynski. Gamma-ray bursters at cosmological distances. *Astrophys. J. Letter*, 308:L43–L46, September 1986.

- [66] C. Palenzuela, S. L. Liebling, D. Neilsen, L. Lehner, O. L. Caballero, E. O'Connor, and M. Anderson. Effects of the microphysical equation of state in the mergers of magnetized neutron stars with neutrino cooling. *Phys. Rev. D*, 92(4):044045, August 2015.
- [67] V. Paschalidis, M. Ruiz, and S. L. Shapiro. Relativistic Simulations of Black Hole-Neutron Star Coalescence: The Jet Emerges. *Astrophys. J. Letter*, 806:L14, June 2015.
- [68] J. S. Read, L. Baiotti, J. D. E. Creighton, J. L. Friedman, B. Giacomazzo, K. Kyutoku, C. Markakis, L. Rezzolla, M. Shibata, and K. Taniguchi. Matter effects on binary neutron star waveforms. *Phys. Rev. D*, 88(4):044042, August 2013.
- [69] Jocelyn S. Read, Benjamin D. Lackey, Benjamin J. Owen, and John L. Friedman. Constraints on a phenomenologically parametrized neutron-star equation of state. *Phys. Rev. D*, 79:124032, Jun 2009.
- [70] C. Reisswig, C. D. Ott, U. Sperhake, and E. Schnetter. Gravitational wave extraction in simulations of rotating stellar core collapse. *Phys. Rev. D*, 83:064008, Mar 2011.
- [71] L. Rezzolla, L. Baiotti, B. Giacomazzo, D. Link, and J. A. Font. Accurate evolutions of unequal-mass neutron-star binaries: properties of the torus and short GRB engines. *Class. Quantum Grav.*, 27(11):114105, June 2010.
- [72] L. Rezzolla, B. Giacomazzo, L. Baiotti, J. Granot, C. Kouveliotou, and M. A. Aloy. The missing link: Merging neutron stars naturally produce jet-like structures and can power short Gamma-Ray Bursts. *Astrophys. J. Letters*, 732(11):L6, May 2011.
- [73] S. Rosswog. Mergers of Neutron Star-Black Hole Binaries with Small Mass Ratios: Nucleosynthesis, Gamma-Ray Bursts, and Electromagnetic Transients. *Astrophys. J.*, 634:1202–1213, December 2005.
- [74] A. Rowlinson, P. T. O'Brien, B. D. Metzger, N. R. Tanvir, and A. J. Levan. Signatures of magnetar central engines in short GRB light curves. *MNRAS*, 430:1061–1087, April 2013.
- [75] M. Ruffert and H.-Th. Janka. Gamma-ray bursts from accreting black holes in neutron star mergers. *Astron. Astrophys.*, 344:573–606, 1999.
- [76] M. Ruiz, R. N. Lang, V. Paschalidis, and S. L. Shapiro. Binary Neutron Star Mergers: A Jet Engine for Short Gamma-Ray Bursts. *ApJ*, 824:L6, June 2016.
- [77] Masaru Shibata and Takashi Nakamura. Evolution of three-dimensional gravitational waves: Harmonic slicing case. *Phys. Rev. D*, 52:5428, 1995.
- [78] D. M. Siegel and R. Ciolfi. Electromagnetic Emission from Long-lived Binary Neutron Star Merger Remnants. I. Formulation of the Problem. *Astrophys. J.*, 819:14S, March 2016.

-
- [79] D. M. Siegel and R. Ciolfi. Electromagnetic Emission from Long-lived Binary Neutron Star Merger Remnants. II. Lightcurves and Spectra. *Astrophys. J.*, 819:15S, March 2016.
- [80] D. M. Siegel, R. Ciolfi, A. I. Harte, and L. Rezzolla. Magnetorotational instability in relativistic hypermassive neutron stars. *Phys. Rev. D*, 87(12):121302, June 2013.
- [81] K. Takami, L. Rezzolla, and L. Baiotti. Spectral properties of the post-merger gravitational-wave signal from binary neutron stars. *Phys. Rev. D*, 91(6):064001, March 2015.
- [82] Kentaro Takami, Luciano Rezzolla, and Luca Baiotti. Constraining the equation of state of neutron stars from binary mergers. *Phys. Rev. Lett.*, 113(9):091104, August 2014.
- [83] N. R. Tanvir, A. J. Levan, A. S. Fruchter, J. Hjorth, R. A. Hounsell, K. Wiersema, and R. L. Tunnicliffe. A ‘kilonova’ associated with the short-duration γ -ray burst GRB 130603B. *Nature*, 500:547–549, August 2013.
- [84] Jonathan Thornburg. A fast apparent-horizon finder for 3-Dimensional Cartesian grids in numerical relativity. *Class. Quantum Grav.*, 21(2):743–766, 2004.
- [85] T. Yamamoto, M. Shibata, and K. Taniguchi. Simulating coalescing compact binaries by a new code (SACRA). *Phys. Rev. D*, 78(6):064054, September 2008.
- [86] B. Yang, Z.-P. Jin, X. Li, S. Covino, X.-Z. Zheng, K. Hotokezaka, Y.-Z. Fan, T. Piran, and D.-M. Wei. A possible macronova in the late afterglow of the long-short burst GRB 060614. *Nature Communications*, 6:7323, June 2015.